DIRECT NUMERICAL SIMULATION OF INCOMPRESSIBLE FLOWS IN DOMAINS OF CLOSE PACKED SPHERES

A Dissertation

by

LAMBERT HENDRIK FICK

Submitted to the Office of Graduate and Professional Studies of
Texas A&M University
in partial fulfillment of the requirements for the degree of

DOCTOR OF PHILOSOPHY

Chair of Committee,	Yassin A. Hassan
Committee Members,	Nagamangala K. Anand
	Maria D. King
	William H. Marlow
	Elia Merzari
Head of Department,	Yassin A. Hassan

May 2017

Major Subject: Nuclear Engineering

ABSTRACT

This study aimed to investigate and quantify turbulent flow effects for incompressible, isothermal fluid flows in computational domains consisting of regularly packed spheres using high-fidelity computational fluid dynamics. The flow domains treated in this study are analogous in an idealized sense to those encountered in pebble bed based high temperature nuclear reactors.

The quantification of turbulent flow effects serves two purposes. Firstly, it assists in the development of lower-fidelity engineering tools such as Reynolds averaged Navier-Stokes based methodologies. Secondly, the quantification of turbulent flow effects adds to our fundamental understanding of the physics of incompressible flows in complex geometries.

The study was conducted using an open-source spectral element computational fluid dynamics code, Nek5000, which was used to perform a series of direct numerical simulations in several flow domains representing both theoretical geometries and idealized sections of a practical reactor core at low to moderate Reynolds numbers.

Selected results include the development of a high-fidelity database of numerical data for an expanded unit-cell geometry, the identification of possible very low frequency temporal dynamics in domains featuring several close packed spheres, and the calculation of turbulence statistics in a domain approximating the near-wall region of a reactor core.

DEDICATION

To Esmé

ACKNOWLEDGEMENTS

I thank my advisor, Dr. Yassin Hassan, for the support and guidance he provided during my time at Texas A&M University. His unrelenting drive to provide the best opportunities for his students and promote excellence in the field of nuclear engineering is an example that I shall aspire to follow in my own career.

I also thank Dr. Elia Merzari for his numerous technical insights and contributions to the work presented in the dissertation. Thanks also to the Nek5000 research group at Argonne National Laboratory for the opportunities and learning experiences that I would not have had without their support.

To my parents, sister, and family-in-law: Thank you for never ceasing to believe in and support Esmé and me, even as we ventured far away from home. Your encouragement, love and advice mean the world to us.

Finally, to my beautiful wife Esmé: Thank you for being my partner on this wonderful adventure.

CONTRIBUTORS AND FUNDING SOURCES

Contributors

This work was supported by a dissertation committee consisting of Drs. Yassin Hassan (advisor) and Dr. William Marlow of the Department of Nuclear Engineering, Drs. Maria King and Nagamangala Anand of the Department of Mechanical Engineering, and Dr. Elia Merzari of Argonne National Laboratory.

All other work conducted for the dissertation was completed by the student independently.

Funding sources

Graduate study was supported by a research assistantship from Texas A&M University.

This research used resources of the Argonne Leadership Computing Facility, which is a DOE Office of Science User Facility supported under Contract DE-AC02-06CH11357.

NOMENCLATURE

Acronyms

ACF	Auto-correlation function
ALCF	Argonne Leadership Computing Facility
BDF	Backward differentiation formula
CCF	Cross-correlation function
CFD	Computational fluid dynamics
CFL	Courant-Friedrichs-Lewy
CU	Convective unit
DNS	Direct numerical simulation
EXT	Extrapolation formula
FCC	Face-centered-cubic
FTT	Flow through time
GLL	Gauss-Lobatto-Legendre
K-H	Kelvin-Helmholtz
LES	Large eddy simulation
N-S	Navier-Stokes
PBR	Pebble bed reactor
POD	Proper orthogonal decomposition
RANS	Reynolds averaged Navier-Stokes
SEM	Spectral element method
TKE	Turbulent kinetic energy
TRISO	Tristructural isotropic
VHTR	Very high temperature, gas-cooled reactor

Non-dimensional characteristic numbers

Fr	Froude number
Re	Reynolds number
St	Strouhal number

Characteristic units

L_D	Characteristic length scale
U_C	Characteristic velocity

Mathematical operations

$\sum$	Summation
$\frac{D}{Dt}$	Material derivative
∇f	Gradient operator
$\nabla \cdot \mathbf{U}$	Divergence operator
$\nabla \times \mathbf{U}$	Curl operator
Δ	Laplace operator
$\frac{\partial}{\partial[x,t]}$	Partial derivative
$\{\cdot\}$	Data ensemble
$\langle\cdot\rangle$	Average
$(\cdot,\cdot)$	Inner product
$*$	Non-dimensionalization

Mathematical symbols

Δt	Time-step length
$\Delta x, \Delta y, \Delta z$	Spatial collocation point separation
δ	Normalized interpolation line coordinate
ϵ	Dissipation tensor
η	Kolmogorov length scale

θ	Angle
λ	Eigenvalues
μ	Dynamic viscosity
ν	Kinematic viscosity
Π	Velocity-pressure-gradient tensor
π	Polar angle
ρ	Density
τ	Stress tensor
τ_η	Kolmogorov time scale
τ_w	Wall shear stress
ϕ	Basis eigenfunctions
ψ	Elevation angle
Ω	Domain
$\hat{\Omega}$	Reference element domain
a	Eigenfunction coefficients
C_f	Skin-friction coefficient
C_p	Pressure coefficient
$\mathbf{f}$	Body force
E_f	Domain element number
g	Gravitational acceleration
h	Lagrange polynomial
L	Interpolation line length
$\mathbf{U}$	Velocity (vector)
U	Velocity (component)
U_o	Free stream velocity

u	Fluctuating velocity (component)
u_η	Kolmogorov velocity scale
u^e_{ijk}	Basis coefficient
N	Polynomial order
$\mathcal{P}$	Production tensor
p	Pressure
p_o	Reference ressure
R	Pressure-rate-of-strain tensor
$T^{(p)}_{ijk}$	Pressure transport tensor
t	Time
$\mathbf{x}$	Position vector
e, f	Fluid domain indices
i, j, k	Index notation indices
r, s, t	Reference element indices
x, y, z	Cartesian components

TABLE OF CONTENTS

Page

LIST OF FIGURES

FIGURE Page

LIST OF TABLES

TABLE Page

1. INTRODUCTION

The objective of this study is to investigate fundamental turbulent flow effects present in flows through structured pebble beds using direct numerical simulation (DNS). To achieve this goal, several numerical experiments were performed for different flow cases, with each case aiming to investigate specific phenomena. Specifically of interest was the development of sets of high quality DNS reference data, the quantification of the transport of turbulent kinetic energy, the temporal dependence of the averaged variable fields, and the effects of bounding walls on flow in the near-wall and bulk flow areas.

1.1 Background

The following subsections serve to broadly outline the relevant concepts, systems, and methods treated in this work. A general description of pebble bed reactors (PBR), which is the practical system to which the research applies, is given. Computational fluid dynamics (CFD) as an investigative tool for fluid dynamics research is then discussed. This is followed by a brief outline of direct numerical simulation, which is the CFD framework used in this study. Finally, the significance and broader impact of the work is discussed.

1.1.1 Pebble bed nuclear reactors

The pebble bed nuclear reactor is one of two variants of the very high temperature gas-cooled reactor (VHTR) concept proposed by the Generation Four International Forum (GIF) as a replacement for currently operating nuclear power reactors. The design is based on an unstructured bed of spherical graphite fuel pebbles in which tristructural isotropic (TRISO) fuel particles are dispersed [3, 4]. Energy transfer

and conversion is facilitated by a helium or molten salt working fluid in the primary system, coupled via heat exchanger to a gas (Brayton) or steam (Rankine) thermodynamic power cycles. The high coolant temperatures achievable by these systems also allows for them to be used for process heat generation. The design offers several improvements over existing light-water based power reactors:

1. Improved economics: high thermal efficiency.

2. Application flexibility: high outlet temperatures that allow for power generation, as well as industrial process heat production.

3. Enhanced safety characteristics: stability of graphite moderator and core structures during accident transients.

A schematic representation of a PBR system is illustrated in Fig. 1.1. The core is comprised either a cylindrical or annular graphite structure, filled with on the order of hundreds of thousands of spherical graphite fuel pebbles. The coolant is generally forced through the core from the top, so as to avoid fluidization of the bed, which may lead to undesired mechanical stresses and wear.

Different proposed designs call for either offline or online refueling. In the case systems using online refueling, the fuel pebbles naturally displace downward and are collected at the bottom of the core barrel before they are reinserted at the top. The displacement rate is slow enough so that the core may be considered stationary when considering flow simulations.

While a number of reactors based on the pebble bed design have been constructed, several technical challenges remain open. From a fluid dynamics standpoint, relevant challenges which may be addressed using fundamental studies include prediction of coolant flow paths, flow stagnation and resultant hot-spot generation, and bypass-flow in the near wall region.

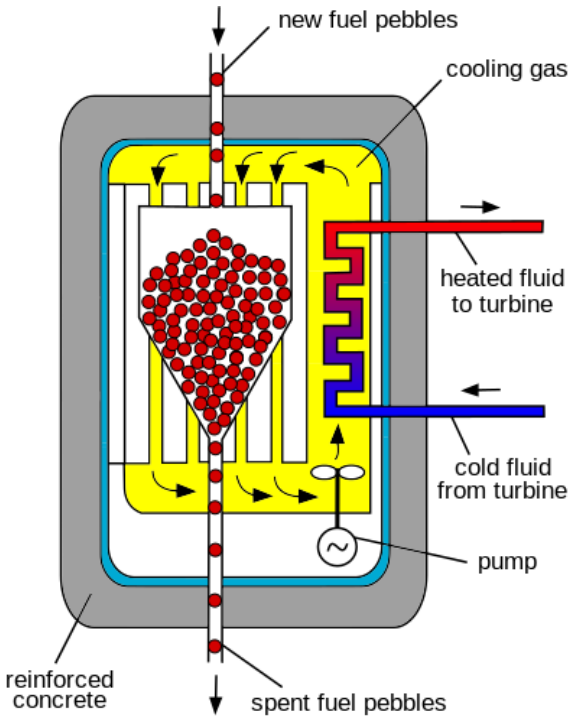

Figure 1.1: Schematic representation of a PBR system, illustrating forced convection from the top of the core, as well as online refueling.

1.1.2 Computational fluid dynamics

Engineered systems that utilize working fluids for energy transport, such as PBRs, almost exclusively operate in the turbulent fluid-flow regime. Turbulence is a time-dependent, three-dimensional, and non-linear process, which through decades of research has been proven to be accurately described by the Navier-Stokes (N-S) equations. Thus, CFD tools incorporate various frameworks to numerically solve or model these equations for flows of interest.

With the advancement of computational resources in the last several decades, CFD has become an integral tool for research and development work pertaining to power systems. CFD provides a practically simplified and more cost-effective tool

for research and development than experiments. It allows for the characterization of fluid flow and heat transfer phenomena in complex systems without the setup time and cost of experiments. Importantly however, many CFD tools are based on mathematical simplifications and assumptions that make simulating complex turbulent phenomena practical in general engineering and design applications. To justify these assumptions experiments must be used to validate the results of CFD computations, especially in new or novel applications.

The following subsections briefly discuss the available CFD frameworks for conducting numerical simulation of pebble bed flows, while a detailed review of the various methodolgies and overarching frameworks may be found in [5].

1.1.3 Reynolds averaged Navier-Stokes

Figure 1.2 details the different numerical frameworks that are available for simulating flows through pebble beds. Reynolds averaged Navier-Stokes (RANS) and porous media based frameworks allow for simulations in computational domains that most closely approximate practical system geometries. These methods are also computationally inexpensive. However, since they rely on a number of assumptions and closure models, the results generated using these methods must be explicitly tested to ensure they deliver accurate results. Several studies using RANS based approaches have illustrated their limited ability to generate accurate results in the pebble bed geometries of interest here [1]. They also provide the least details in terms of the underlying physics.

1.1.4 Large eddy simulation and hybrid methods

Higher fidelity methods such as large eddy simulation (LES) and hybrid RANS/LES methods allow for more accurate numerical simulations that also better resolve the relevant physics, at the cost of increased computational expense. As computational

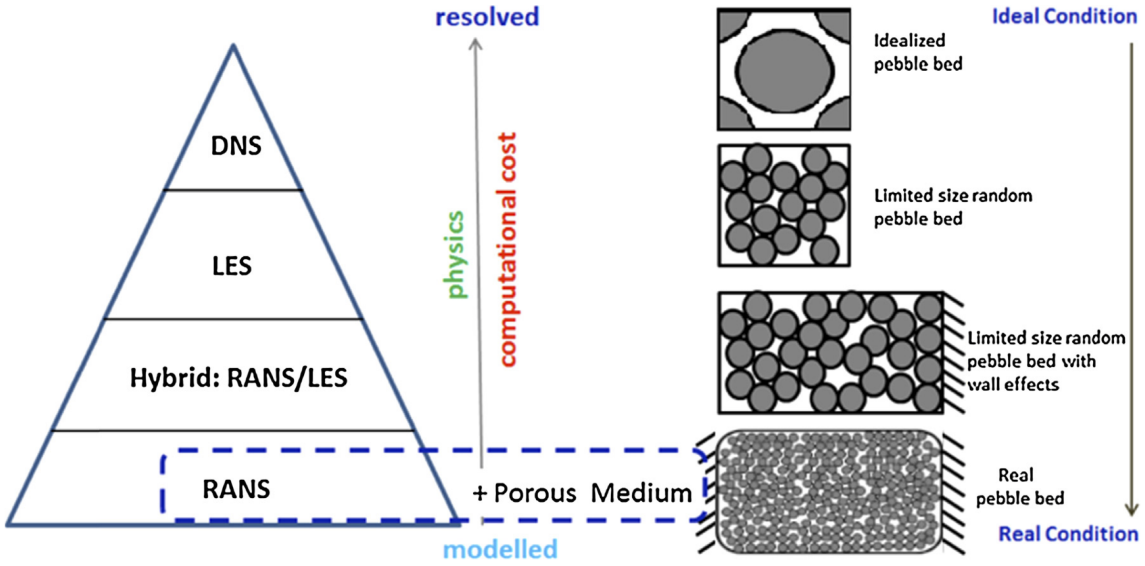

Figure 1.2: The different frameworks in which numerical studies of flows through pebble beds may be conducted [1].

fluid dynamics tools and resources become more advanced, these methods are becoming more prevalent in engineering research. Examples of such studies include [6, 7].

1.1.5 Direct numerical simulation

Direct numerical simulation (DNS) explicitly solves the discritized N-S equations using selected numerical methods, without the need for any modeling of the small scales of turbulent motion as is required for RANS and LES based approaches. This frameworks represents the costliest framework for solving the N-S equations, but delivers unparalleled spatial and temporal fidelity, capturing all the physical phenomena present in turbulent flows. Consequently, DNS is the preferred methodology for fundamental turbulence research, and is employed in this study in the form of the Nek5000 spectral element CFD code.

The spectral element method is a higher-order spatial method which forms a sub-

class of the finite-element discretization framework [8]. This method is well suited for DNS, since it exhibits low numerical dissipation and dispersion, which is specifically important when performing detailed investigations on physical effects such as the dissipation of turbulent kinetic energy in flows under consideration.

The computational cost of DNS remains prohibitive. This limits both the size of computational domains that may be considered, as well as the achievable flow Reynolds numbers. Therefore, this study focuses on flow in regularized domains much smaller than what is encountered in practical systems, while also only considering low to moderate Reynolds number flows.

1.2 Objectives of the study

The aim of the study is to contribute in a meaningful manner to our understanding of the dynamics of turbulent flows in pebble bed geometries. Additionally, by conducting the research in a manner that facilitates the use of the developed data in the optimization of engineering research and design tools, the work aims to also be applicable in a broader sense.

By designing several simulations pertaining to flows in pebble beds and performing pertinent analyses for each of the cases, the above mentioned goal may be achieved. Three studies, each with a specific set of goals are proposed, with the anticipated goals for each study are summarized in a point-wise manner below:

1. Numerical experiment I: Flow over one and two spheres in free-stream conditions:
    - Verify the simulation methodology by using the available numerical simulation and experimental literature.
    - Confirm increased meta-stable behavior of data averaged over long time-integration periods when additional spheres are added to the canonical

case of flow over a single sphere.

2. Numerical experiment II: Face-centered-cubic (FCC) domain.

    - Generate a high-fidelity database of time-invariant flow data, including:
        - First- and second-order turbulence statistics.
        - Budgets of the turbulent kinetic energy.
    - Identify and isolate temporal instabilities present in the flow.

3. Numerical experiment III: Wall-bounded, expanded FCC domain.

    - Generate first-of-a-kind DNS results that quantify the effect of a bounding wall on the flow.

The chronological order in which the studies were conducted does not follow the numbering of the numerical experiments listed above. Chronologically, the FCC study was conducted first, followed by the spheres in free-stream conditions, and finally the wall case. The reasoning for the deviation in presentation order from the chronological order in which the experiments were conducted is to create a logical progression in the complexity of the cases being considered both in terms of flow parameters and geometry.

1.3 Structure of the dissertation

The different numerical studies that comprise the dissertation will be treated as independent results and discussions sections, with an overarching structure provided by consolidated general introduction, mathematical theory, and conclusions sections.

The structure of the dissertation may be summarized section-wise below:

1. Section 1: Introduction. General introduction, including the relevant simulation framework and objectives of the study.

2. Section 2: Mathematical theory. Brief discussion of the mathematical theory that is relevant to all the subsequent sections.

3. Sections 3-5: Computational studies.

   (a) Numerical experiment I: Single and two sphere cases.

   (b) Numerical experiment II: Single unit cell and expanded cases.

   (c) Numerical experiment III: Wall bounded case.

4. Section 6: Conclusions and future work.

1.4 Summary

The background section served to introduce the engineering system of interest in this study, along with a brief introduction to CFD and DNS, which will be the tool employed in this study.

The objectives of the study are to provide CFD model developers with relevant, statistically averaged and time-invariant data for the purpose of model optimization and development. Furthermore, the study aims to quantify complex turbulent phenomena present in pebble beds.

2. THEORETICAL BACKGROUND

This section briefly outlines the mathematical theory relevant to the works that will be subsequently discussed. Instead of fully re-deriving the conservation equations and mathematical tools, only short discussions with references to relevant texts are given for the sake of brevity. More specific methods, which might only pertain to certain sections in the results, are discussed in the specific sections where they are relevant.

The conservation laws, in the form of the Navier-Stokes eqations, are initially stated. This is followed by a brief discussion of the numerical discretization of the equations as it is implemented in Nek5000. The turbulent kinetic energy transport equation, for which the budgets were calculated in several of the studies, is discussed. The requirements for classification of a numerical simulation of a turbulent flow as a direct numerical simulation, which itself requires access to the aforementioned turbulent kinetic energy transport equation terms, is treated. Finally, the method of proper orthogonal decomposition (POD), which was used in multiple cases during this study, is briefly treated.

2.1 Navier-Stokes equations

Following the derivation in [9], the constant property, incompressible, dimensional Navier-Stokes equations are

$$\partial_t \rho + \nabla \cdot (\rho \mathbf{U}) = 0 \quad (Continuity) \tag{2.1}$$

$$\rho \left(\partial_t \mathbf{U} + \mathbf{U} \cdot \nabla \mathbf{U}\right) = -\nabla p + \nabla \cdot \tau + \rho \mathbf{f} \quad (Momentum) \tag{2.2}$$

where $\tau = \mu\left(\nabla\mathbf{U} + \nabla\mathbf{U}^T\right)$. Since we consider constant property flows, the continuity equation (2.1) reduces to the divergence-free (solenoidal) condition $\nabla \cdot \mathbf{U} = 0$. Furthermore, our constant viscosity allows for the contraction of the viscous stress tensor, so that

$$\nabla \cdot \tau = \mu\Delta\mathbf{U}. \tag{2.3}$$

The dimensional Navier-Stokes equations may be non-dimensionalized using appropriate characteristic parameters. Using L_D and U_C as arbitrary characteristic length and velocity parameters, so that $\mathbf{x}^* = \mathbf{x}/L_D$, $\mathbf{U}^* = \mathbf{U}/U_C$, $t^* = \frac{t}{L_D/U_C}$, and assuming dominant convective effects, i.e. $p^* = \frac{p}{\rho U_C^2}$, the Navier-Stokes equations can be non-dimensionalized to

$$\partial_t\mathbf{U}^* + \mathbf{U}^* \cdot \nabla\mathbf{U}^* = -\nabla p^* + \frac{1}{Re}\Delta\mathbf{U}^* + \frac{1}{Fr}\frac{\mathbf{f}}{g}, \tag{2.4}$$

where $Re = \frac{\rho U_C L_D}{\mu}$ and $Fr = \frac{U_C^2}{gL_D}$ Since no external forces are assumed in the simulations, we operate in the $Fr \to \infty$ limit. Thus, we obtain a set of free equations.

$$\nabla \cdot \mathbf{U} = 0 \tag{2.5}$$

$$\partial_t\mathbf{U}^* + \mathbf{U}^* \cdot \nabla\mathbf{U}^* = -\nabla p^* + \frac{1}{Re}\Delta\mathbf{U}^*, \tag{2.6}$$

This formulation of the governing equations is used consistently throughout the remainder of the dissertation. For simplicity the $*$ notation is dropped. Since the density is unity in all the cases considered in the remainder of the dissertation, the

Reynolds stresses are simply represented by the covariances of the fluctuating velocity field, $\langle u_i u_j \rangle$, where the fluctuating velocity field is obtained using standard Reynolds decomposition, $u_i = \langle u_i \rangle - U_i$.

2.2 Spectral element method and Nek5000 numerical schemes

The spectral element method (SEM) is a high-order finite element method for the numerical solution of partial differential equations. The method is based on discretization of a given computational domain into disjoint macro-elements, with the solution and geometry approximated via high-order polynomial expansions within each macro-element. The method combines high-order (spectral) accuracy, while providing the geometric flexibility of low-order finite-element techniques.

For the three-dimensional flows considered in this dissertation, the spectral element method entails breaking the computational domain up in to hexahedral elements, with each element face consisting of non-degenerate quadrangles. Within each element, a local Cartesian mesh is constructed corresponding to a $N \times N \times N$ tensor-product box. The solution is evaluated in this tensor-product box using Lagrange polynomials, evaluated at Gauss-Lobatto-Legendre (GLL) collocation points. The GLL distribution clusters the evaluation points near the element boundaries, and is chosen due to it's accurate approximation, interpolation, and quadrature properties.

A basic description of the spectral element method as it is implemented in Nek5000 is given in the following subsections. The interested reader may refer to [10] for further details regarding the SEM.

2.2.1 Spatial discretization

The SEM was originally developed using Chebyshev collocation within each element [8], but this was subsequently replaced by a Galerkin formulation based on GLL quadrature [11].

In the SEM, data is represented on sets of nonoverlapping subdomains, Ω^e , $e = 1, ..., E_f$, with the entire domain

$$\Omega_f := \bigcup_{e=1}^{E_f} \Omega^e. \tag{2.7}$$

In each element, a typical variable $u(\mathbf{x})$ is represented by

$$u(\mathbf{x})\,|_{\Omega^e} = u(x, y, z)\,|_{\Omega^e} = \sum_{k=0}^{N}\sum_{j=0}^{N}\sum_{i=0}^{N} u^e_{ijk} h_i(r)\, h_j(s)\, h_k(t), \tag{2.8}$$

where u^e_{ijk} are the basis coefficients; $h_i(r)$, $h_j(s)$, $h_k(t)$ are N-th order one-dimensional Lagrange polynomials evaluated at GLL points, and $\mathbf{r} := (r, s, t)$ are the coordinates in the canonical reference element $\hat{\Omega} := [-1, 1]^3$. For $\mathbf{x} := (x, y, z) \in \Omega^e$, an isoparametric mapping

$$\mathbf{x}|_{\Omega^e} = \sum_{k=0}^{N}\sum_{j=0}^{N}\sum_{i=0}^{N} \mathbf{x}^e_{ijk} h_i(r)\, h_j(s)\, h_k(t), \tag{2.9}$$

relates Ω^e as the image of $\hat{\Omega}$ under the polynomial mapping in eq. (2.9). This mapping is assumed to be invertible, and thus requires the angles at the edges of Ω^e are bounded away from 0° and 180°, and that the edges of the element are smooth.

The discretization of the pressure space is similar to that of the velocity space, with the only difference being that Lagrange interpolants of order $N - 2$ are used that are evaluated at Gauss-Legendre collocation points. This formulation is formally known as the $\mathbb{P}_N - \mathbb{P}_{N-2}$ SEM.

2.2.2 Temporal discretization

Nek5000 uses a semi-implicit time-stepping method. In the formulation, the viscous terms in the Navier-Stokes equation, given in eq. (2.5), are treated implicitly using a k-step backward differentiation formula (BDFk) based on a truncated Taylor expansion of the solution, while the non-linear (convective) terms are treated using an explicit extrapolation scheme of order k (EXTk). For the simulations conducted in this dissertation, an order of $k = 3$ was used, resulting in a $BDF3/EXT3$ time-stepping scheme that is globally third-order accurate.

Due to the explicit treatment of the convective terms, a restriction exists on the time-step size Δt, so as to maintain stability during time-marching. The stability condition, termed the Courant-Friedrichs-Lewy (CFL) condition, can be written in the form

$$\Delta t < C \times MIN_{\Omega_f} \left\{ \frac{\Delta x}{|u_x|}, \frac{\Delta y}{|u_y|}, \frac{\Delta z}{|u_z|} \right\}, \tag{2.10}$$

where C is the CFL number, $\Delta x, \Delta y, \Delta z$ are the x, y, z distances between the spatial collocation points, u_x, u_y, u_z are their corresponding velocities, and MIN_{Ω_f} refers to the minimum over the entire flow field.

2.3 Turbulent kinetic energy transport equation

The quantification of the evolution of turbulent kinetic energy in a flow is integral to our understanding of turbulent flow processes. Since DNS allows us to decompose the turbulent flow field using Reynolds decomposition, each term of the turbulent kinetic energy equation may be computed at every point in the domain. Following [9], the turbulent kinetic energy equation is given as

$$0 = \overbrace{-\frac{\bar{D}}{\bar{D}t}\left\langle u_i u_j \right\rangle}^{Mean\ convection} - \overbrace{\frac{\partial}{\partial x_k}\left\langle u_i u_j u_k \right\rangle}^{Turbulent\ convection} + \overbrace{\nu\nabla^2\left\langle u_i u_j \right\rangle}^{Viscous\ diffusion} + \mathcal{P}_{ij} + \Pi_{ij} - \epsilon_{ij}, \tag{2.11}$$

where $\mathcal{P}_{ij}$ is the production tensor

$$\mathcal{P}_{ij} \equiv -\left\langle u_i u_k \right\rangle \frac{\partial \left\langle U_j \right\rangle}{\partial x_k} - \left\langle u_j u_k \right\rangle \frac{\partial \left\langle U_i \right\rangle}{\partial x_k}, \tag{2.12}$$

Π_{ij} is the velocity-pressure-gradient tensor

$$\Pi_{ij} \equiv -\frac{1}{\rho}\left\langle u_i \frac{\partial p'}{\partial x_j} + u_j \frac{\partial p'}{\partial x_i} \right\rangle, \tag{2.13}$$

and ϵ_{ij} is the dissipation tensor

$$\epsilon_{ij} \equiv \left\langle \frac{\partial u_i}{\partial x_k} \frac{\partial u_j}{\partial x_k} \right\rangle. \tag{2.14}$$

The velocity-pressure-gradient tensor may be decomposed so that

$$\Pi_{ij} = \mathcal{R}_{ij} - \frac{\partial}{\partial x_k} T^{(p)}_{ijk}, \tag{2.15}$$

where $\mathcal{R}_{ij}$ is the pressure-rate-of-strain tensor

$$\mathcal{R}_{ij} \equiv \left\langle \frac{p'}{\rho} \left(\frac{\partial u_i}{\partial x_j} + \frac{\partial u_j}{\partial x_i} \right) \right\rangle, \tag{2.16}$$

and $T_{ijk}^{(p)}$ is the pressure transport tensor

$$T_{ijk}^{(p)} \equiv \frac{1}{\rho} \langle u_i p' \rangle \, \delta_{jk} + \frac{1}{\rho} \langle u_j p' \rangle \, \delta_{ik}. \tag{2.17}$$

Each of these terms may be calculated in Nek5000 by calling subroutines developed in [12]. Different terms in the turbulent kinetic energy transport equation are calculated and discussed in results presented in later sections of the dissertation.

2.4 Requirements for DNS

For a numerical simulation to be termed DNS, it must resolve all the length and time scales in a turbulent flow. The concept of the energy cascade, which was put forth in [13], states that turbulence is comprised of eddies of different sizes. Turbulent kinetic energy is imparted to the largest eddies in the flow from the mean flow kinetic energy, after which it is cascaded through increasingly smaller eddies to the dissipation scales, which are the smallest length and time scales in a turbulent flow. At these scales, the turbulent kinetic energy is transformed into heat energy.

Kolmogorov theory, which is underpinned by three hypotheses, remains the most widely accepted theory that formalizes the energy cascade process and the characteristics of the smallest scales of turbulent motion. The first Kolmogorov similarity hypothesis [14] states that the statistics of a turbulent flow at a sufficiently high Reynolds number have a universal form that is uniquely determined by the flow kinematic viscosity ν, and dissipation ϵ. Based on this, the Kolmogorov length,

velocity, and time scales may be defined respectively as:

$$\eta \equiv \left(\frac{\nu^3}{\epsilon}\right)^{1/4}, \tag{2.18}$$

$$u_\eta \equiv (\nu\epsilon)^{1/4}, \tag{2.19}$$

$$\tau_\eta \equiv \left(\frac{\nu}{\epsilon}\right)^{1/2}. \tag{2.20}$$

These scales represent a minimum criterion to which the discretization of a numerical turbulent flow simulation must adhere to be termed a direct numerical simulation. When both the temporal, as well as the spatial discretization of the numerical case is finer than the Kolmogorov time and length scales respectively, all the possibles scales of motion that is present in the flow will be captured, and the numerical simulation may be classified as a direct numerical simulation.

While the Reynolds numbers of the flows treated in these studies could not be explicitly classified as having sufficient Reynolds number based on the first similarity hypothesis, these scales were calculated for the intermediate Reynolds number cases that will be discussed in §4 and §5 and compared with relevant spatial and temporal discretizations of those cases to test for conformance to DNS requirements.

2.5 Proper orthogonal decomposition

Proper orthogonal decomposition is a powerful analytical tool that allows us to identify coherent structures in turbulent flows based on their energy content. POD provides a basis for modal decomposition of an ensemble of functions, such as data generated in DNS studies, with the goal of efficiently capturing the dominant features of a near-infinite-dimensional process (turbulence) with a drastically reduced number of representative modes.

POD data generated from turbulent flow simulations may be used in different ways. Firstly, the POD modes may be used as a set of basis functions for the construction of a low-dimensional approximation of a full simulation governed by the Navier-Stokes equations. Such a low-dimensional approximation, termed a reduced order model, generally consists of a system of ordinary differential equations that are integrated in time to calculate temporal coefficients, which when combined with the spatial information contained in the POD modes, may be used to approximately reconstruct the dynamic behavior of the flow in question.

Secondly, since POD decomposes the flow field optimally in such a manner that the persistent (temporally), highest energy structures in the flow are highlighted, it allows us to investigate the physical effects that drive the behavior of the flow.

A brief discussion of the theory of POD following [15], and the method of snapshots [16], which is implemented in Nek5000 [17], is given below.

When seeking a good representation of the members of an ensemble of data, for example scalar fields $\left\{u^k\right\}$ with each a function $u = u(x)$ defined on $0 \leq x \leq 1$, each u must be projected onto candidate basis functions. Thus, we assume that the functions belong to an inner product space such as the $L^2([0,1])$ space of square-integrable functions with inner product

$$(f, g) = \int_0^1 f(x)\, g(x)\, dx. \tag{2.21}$$

Thus, we want to find a basis $\{\phi_j(x)\}_{j=0}^{\infty}$ for L^2 that is optimal for the data set in the sense that the finite-dimensional representations of the form

$$u_N(x) = \sum_{j=1}^{N} a_j \phi_j(x) \tag{2.22}$$

describe typical members of the ensemble better than representations of the same dimension in any other basis. The term typical implies averaging, which in our simulations is taken to be a time average over an ensemble with members $u^k(x) = u(x, t_k)$ taken sequentially during time integration.

If the L^2 space considered in the example is taken to be a more general Hilbert space $\mathcal{H}$, the optimality condition for choosing the basis implies maximizing the normalized averaged projection of u onto ϕ,

$$\max_{\phi \in \mathcal{H}} \frac{\left\langle | (u, \phi)^2 | \right\rangle}{\|\phi\|^2}. \tag{2.23}$$

This problem is solved using the calculus of variations, and delivers the following eigenvalue problem

$$\mathcal{K}\phi = \lambda\phi \tag{2.24}$$

Thus, the optimal basis is given by the eigenfunctions $\{\phi^j\}$ of the operator $\mathcal{K}$ that is defined from the computational data, and are termed the POD modes.

Expanding (2.24), we have

$$\mathcal{K}\phi\left(\mathbf{x}\right)=\int_{\Omega}K\left(\mathbf{x},\mathbf{x}'\right)\phi\left(\mathbf{x}'\right)d\left(\mathbf{x}'\right)=\lambda\phi\left(\mathbf{x}\right), \tag{2.25}$$

where the kernel $K\left(\mathbf{x},\mathbf{x}'\right)=\left\langle \mathbf{u}\left(\mathbf{x},t\right)\mathbf{u}\left(\mathbf{x}',t\right)\right\rangle$, and the vector multiplication implies a dyadic product. Considering the finite dimensional case with $\mathcal{H}=\mathbb{R}^{N}$, with the data coming from the simulations as a collection of M vectors $\mathbf{u}^{k}\in\mathbb{R}^{N}$, and $\langle\cdot\rangle$ represents an arithmetic mean, the Kernel may be written as

$$\mathcal{K}_{ij}=\frac{1}{M}\sum_{k=1}^{M}u_{i}^{k}u_{j}^{k}. \tag{2.26}$$

Thus, $\mathcal{K}$ is a real, symmetric $N\times N$ matrix, and eq. (2.24) is a standard matrix eigenvalue problem in $\mathbb{R}^{N}$. However, since the number of grid points N is substantial in DNS calculations, it is impractical to solve this eigenvalue problem for the DNS data analysis. Thus, we instead use the method of snapshots to solve an $M\times M$ problem.

In the method of snapshots, the collection of M vectors that is used to generate the kernel in eq. (2.26), is a series of linearly independent flow realizations taken sequentially during time integration of the turbulent flow case. Now, taking $\{\mathbf{u}^{i}\}_{i=1}^{M}$ as the realizations of the flow field and that the inner product of the N-dimensional vector space of the realizations is denoted by $(\cdot,\cdot)$, this is the discretized version of the $L^{2}\left(\Omega\right)$ inner product. Each eigenfunction may be written as

$$\phi=\sum_{k=1}^{M}a_{k}\mathbf{u}^{k}, \tag{2.27}$$

with the coefficients a_k to be computed. Using eq. (2.26), the eigenvalue problem given in eq. (2.24) may be rewritten as:

$$\left(\frac{1}{M}\sum_{i=1}^{M}\mathbf{u}^i\left(\mathbf{u}^i\right)^T\right)\sum_{k=1}^{M}a_k\mathbf{u}^k=\lambda\sum_{k=1}^{M}a_k\mathbf{u}^k \tag{2.28}$$

The l.h.s. may be rewritten in the following manner:

$$\sum_{i=1}^{M}\left[\sum_{k=1}^{M}\frac{1}{M}\left(\mathbf{u}^k,\mathbf{u}^i\right)a_k\right]\mathbf{u}^i. \tag{2.29}$$

A sufficient condition for the solution of eq. (2.24) will be to find the coefficients a_k such that

$$\sum_{i=1}^{M}\frac{1}{M}\left(\mathbf{u}^k,\mathbf{u}^i\right)a_k=\lambda a_i\ ;\ i=1,...,M. \tag{2.30}$$

This is the form of the $M\times M$ eigenvalue problem that is solved in Nek5000 to compute the POD modes of the flow under consideration.

2.6 Summary

This section detailed the mathematical theory that serves as basis for the studies detailed in the following section, including the conservation equations, the turbulent kinetic energy transport equation derived from the Navier-Stokes equations using Reynolds decomposition, the discretization requirements for DNS, POD, and the spectral element method which is utilized in Nek5000. The next three sections detail separate numerical experiments focusing on different aspects of flows through

domains consisting of multiple close packed spheres.

3. NUMERICAL EXPERIMENT I: SINGLE AND TWO SPHERES

The second numerical experiment conducted during the dissertation research is presented as the first numerical experiment in this section. This ordering was chosen so that the impact of multiple spheres on the temporal dynamics of the flow is highlighted early. This ordering of the presented studies also allows for a satisfying progression of the geometric complexity of the considered cases, as well as the progression of the flow complexity as characterized by the Reynolds number.

This section consists of a brief background regarding the canonical case of flows over a single sphere in free-stream conditions, as well as the proposed addition of spheres to increase complexity. This is followed by a discussion of the methodology followed in the study, a presentation of the most pertinent results and associated discussions, and finally some conclusions drawn from the study.

3.1 Background

The study of incompressible flow over spherical bluff bodies is encountered both in fundamental fluid dynamics research, as well as in in research pertaining to physical systems such as high temperature nuclear reactors.

Computational limitations have largely prevented researchers from using high fidelity methods such as direct numerical simulations to extract similarly detailed results from representative engineering flow simulations as has been achieved in fundamental studies. Thus, the bulk of the available high fidelity numerical results pertaining to flows over spheres is devoted to fundamental studies of simplified flows over single spheres in free stream conditions. Examples include studies at low Reynolds numbers focusing on quantifying transition dynamics [18], and intermediate Reynolds number simulations using large eddy simulation and DNS focusing on

wake visualization and first- and second order turbulence statistics [19, 20].

For practical flows over spherical bodies, such as those encountered gas-cooled nuclear reactors, numerical simulations have largely been done using Reynolds averaged Navier-Stokes (RANS) and hybrid-RANS based frameworks. For RANS based simulations, examples of research include the quantification of the effects of contact treatment between the spheres, and the calculation of turbulence statistics. However, since RANS based methods have inherent modeling uncertainties, they must be verified and validated using either experimental or DNS flow data.

In support of the development of DNS verification data for RANS based simulations, results have recently been published from the simulation of isothermal, intermediate Reynolds number flow through an idealized domain of packed spheres [21]. During the simulations, low-frequency temporal instabilities in the flow were observed that led to unsteady averaged statistics, even over long periods of time-integration.

In this work, the aim is to further quantify the observed instability in flows over multiple spherical bodies by reducing both the complexity of the flow physics, i.e. the Reynolds number, as well as the the geometry, and thus isolate more clearly the mechanism of the observed instability. Results from two simulations, flow over a single and two spheres, are presented. Both cases were run with a Reynolds number of 1000.

The case of flow over a single sphere was used to verify that the numerical simulations delivered acceptably valid results, and also as reference case with which results from the second case could be compared. Presented results include selected first- and second order turbulence statistics, temporal auto- and cross-correlations, and analysis of POD data.

3.2 Methodology

This subsection outlines the cases under consideration, including the geometric, flow, and computational parameters used in the study.

3.2.1 Geometry and boundary conditions

The first geometry under consideration is the canonical single sphere in free stream conditions. The mesh for the case was generated in Prenek, the native mesh generation and pre-processing module in Nek5000. The meshing process consisted of generating a rectangular three-dimensional box with the extents defined by $-5 \leq x/L_D, y/L_D \leq 5$, and $-5 \leq z/L_D \leq 25$, after which a spherical shell mesh with spherical to rectangular transition elements with extents of $-1 \leq x/L_D, y/L_D, z/L_D \leq 1$ was substituted into the box domain at the origin. This resulted in a mesh with $24,416$ elements. The diameter of the sphere is defined as $L_D = 1$. The sections of the mesh surrounding the sphere(s) for the two cases is illustrated in Fig. 3.1.

The geometric parameters for the mesh resulted in a blockage of 1%, which is considered negligible for experiments on this type of geometry [22, 23], and is therefore appropriate in our numerical study.

The second mesh was generated using the same procedure as for the first mesh, only with an additional spherical to rectangular mesh being added with center point at $[x/L_D, y/L_D, z/L_D] = [0, 0, 2]$, resulting in a mesh with $24,832$ elements. Since the spheres for the second case are located along the same axial line as for the single sphere case, the blockage ratio remains the same. A polynomial order of $N = 11$ was chosen for both cases.

The boundary conditions were consistent for the two cases. No-slip wall conditions were imposed on the sphere surfaces, while the upstream and radial boundaries were set to a constant stream wise velocity of $U_z = 1$. An outflow boundary con-

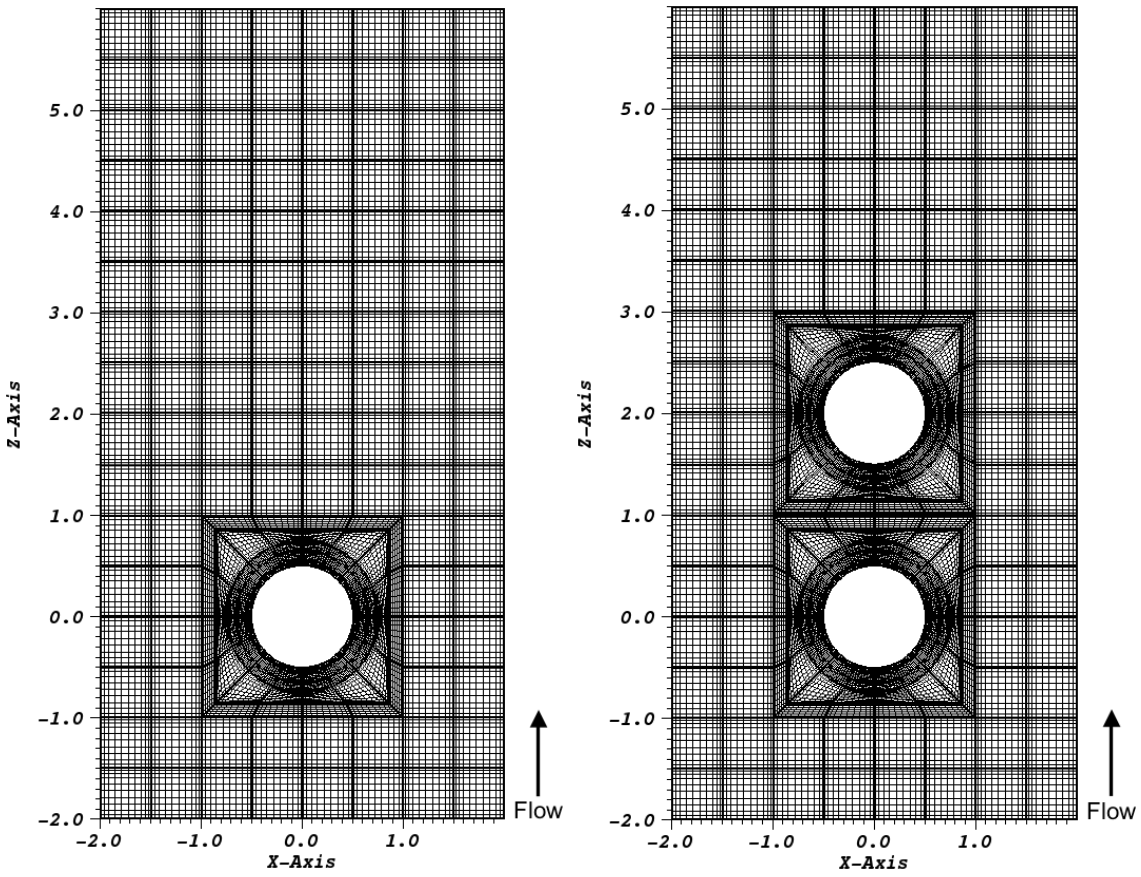

Figure 3.1: Planar sections of the spectral element meshes for the two cases.

dition was used at the downstream boundary. This setup is similar to that used in [18], which was conducted at corresponding Reynolds numbers.

3.2.2 Computational parameters

The flow Reynolds number for the cases was defined using the free stream velocity, $U_o = 1$, and pebble diameter $L_D = 1$. A unit density was assigned to the fluid, allowing the Reynolds number to be defined as $Re = 1/\mu$. Since the purpose for the study was the investigation of unsteady dynamics resulting from spheres in close proximity, a value of $Re = 1000$ was chosen for the simulations. This allowed us to

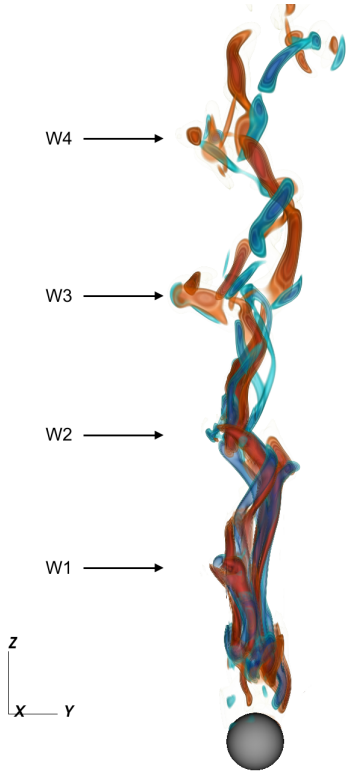

Figure 3.2: Volume rendering of the instantaneous stream wise vorticity in the wake of the single sphere case.

run in the unsteady, subcritical regime for flows over bluff bodies, whilst avoiding the increased spatial and temporal resolution requirements for higher values of the Reynolds number. This choice also allowed for verification of the single sphere results with results from previous studies.

The instantaneous stream wise vorticity component in the wake of the single sphere case is shown in Fig. 3.2, with four vortex structures (indicated by W1-4) observable in the wake region. A Kelvin-Helmholtz instability is known to exist in the shear layer in the near downstream region of the sphere at this subcritical Reynolds number [20], which results in the vortex structures not being as coherent as those observed in the pure Kármán vortex regime at lower Reynolds numbers.

Table 3.1: Computational parameters: 1 & 2 sphere cases

	Case (Spheres)	
Parameter	1	2
Reynolds number ($1/\mu$)	1,000	1,000
Time step length (L_D/U)	0.004	0.004
Collocation points	$3.220E7$	$3.275E7$
CPU Cores	16,384	16,384
Total CU	1,120	1,120

Both cases were run concurrently on the Argonne Leadership Computing Facility IBM Blue Gene/Q clusters located at Argonne National Laboratory. Initial flow development to turbulent conditions was done for both cases using a lower discretization order of $N = 5$, to allow for rapid time stepping. Flow was developed for 200 convective units (CU $= L_D/U_o$) before production runs were commenced. Table 3.1 presents a summary of the run-time parameters used during production runs.

3.2.3 Verification

To ensure the validity of the presented data, selected results from the single sphere case were compared with results from experimental and computational studies carried out using similar geometries.

3.2.4 Wake separation frequency

For the single sphere case, temporal data for $1,200$ point probes in the near wake region were recorded during production runs. The point probes were seperated into 12 lines of 100 probes at increasing distances downstream of the sphere. Six lines were defined in the $[x, 0, z]$ and $[0, y, z]$ planes respectively. For a selected point in the shear layer downstream of the sphere, the power spectrum seen in Fig. 3.3

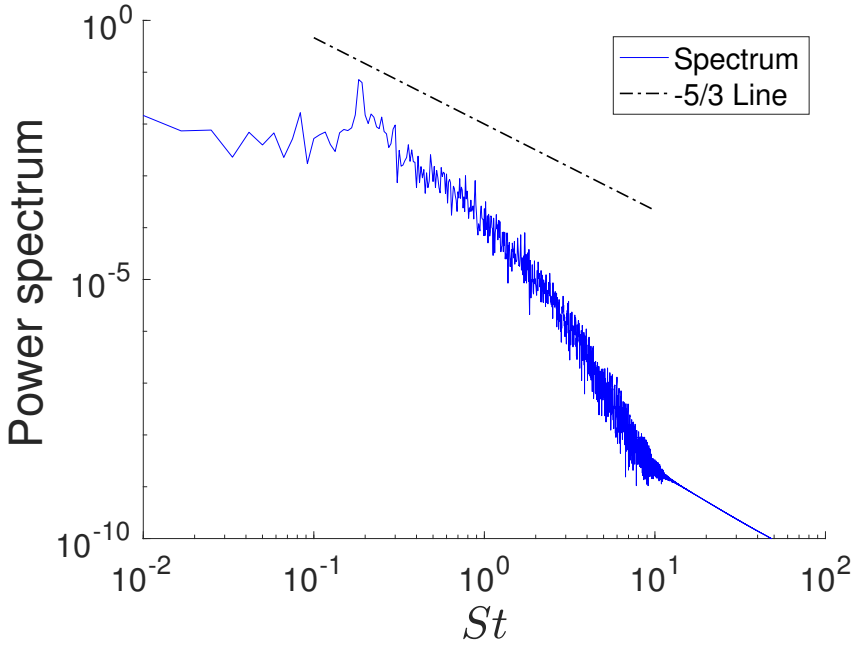

Figure 3.3: Power spectrum of U_z at $z/L_D = 3$ and $z/L_D = 0.3$. The observed energy peak corresponds to the shedding Strouhal number, $St = 0.187$.

shows agreement with experimental data for flow at $Re = 1000$ [23], who observed a shedding Strouhal number in the range of 0.187-0.202. The value of $St = 0.187$ for this simulation also correspond reasonably with the value of $St = 0.195$ reported during computational studies [18].

3.2.5 Wake axial velocity.

Another parameter that is well quantified for flow over a single sphere is the averaged stream wise velocity along the domain axial center line. A comparison of our result with the experimental results in is shown in Fig. 3.4. While the profiles show generally good agreement, the results from the current study do over predict the magnitude of the velocity in the recirculation region.

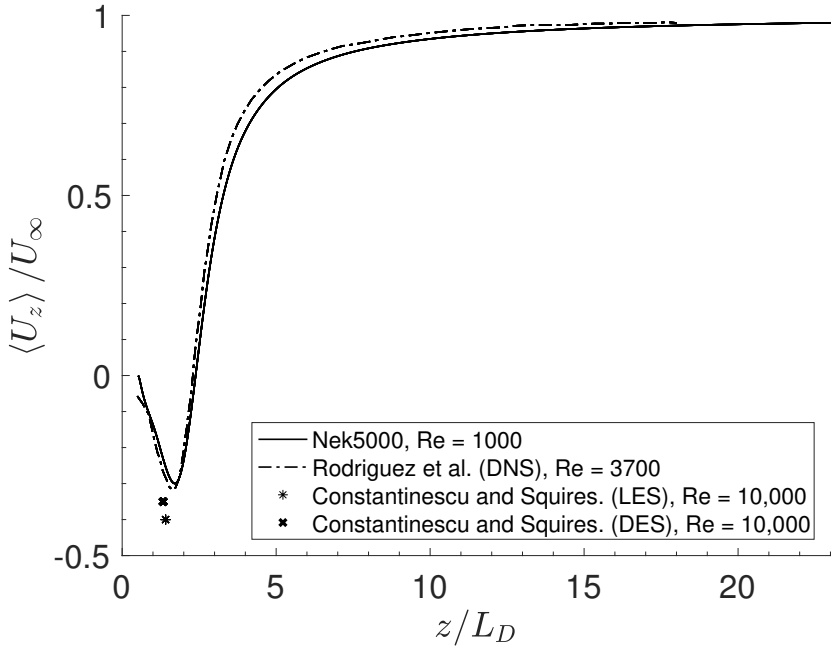

Figure 3.4: Profile of $\langle U_z \rangle$ along the domain axial center line and comparison with the experimental data of [2].

3.2.6 Pressure and skin-friction coefficients

Figure 3.5 shows the distribution of the pressure coefficient, defined as

$$C_p = \frac{2\,(p - p_o)}{\rho U_o^2} \tag{3.1}$$

on the surface of the sphere. The angle is measured from upstream to downstream. Comparative results from both computational and experimental studies is also provided. From the computational results from [18] and the present study, it is observed that as the Reynolds number increases, the angular position where the negative pressure magnitude is lowest shifts towards the upstream (front) position on the surface

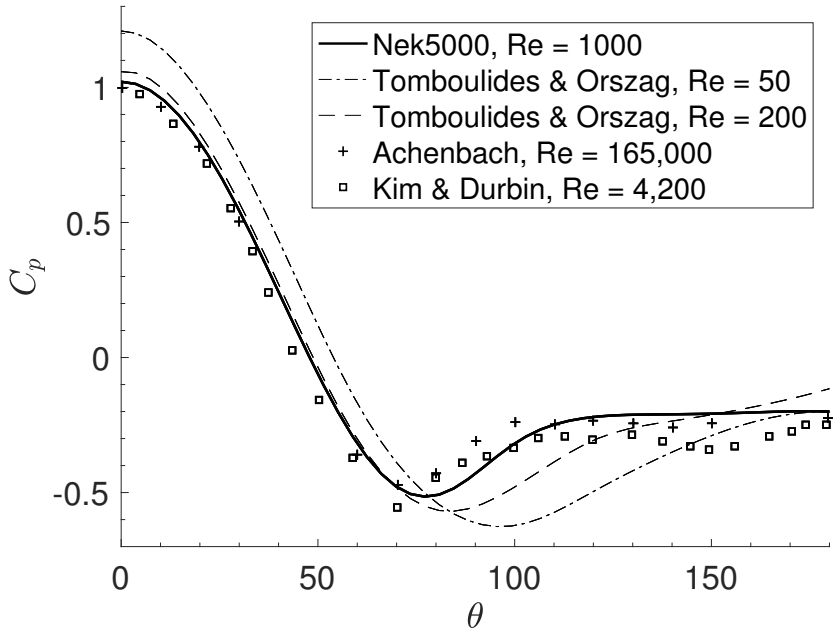

Figure 3.5: Profile of the pressure coefficient on the sphere surface.

of the sphere. The trend also shows that the maximum magnitude of the negative value of the pressure coefficient decreases as the Reynolds number increases. This trend is further confirmed by the experimental results of [24, 23], where the angular point of largest negative magnitude is shifted to the front of the sphere, and the magnitude of the value decreases with increased Reynolds number.

The skin-friction coefficient, defined as

$$C_f = \frac{\tau_w}{\rho U_o^2} \tag{3.2}$$

where $\tau_w = \mu \left(\frac{\partial U}{\partial y}\right)_{y=0}$, is plotted in Fig. 3.6. For comparison with experimental results generated at larger Reynolds numbers, the values are normalized using $\sqrt{Re}$.

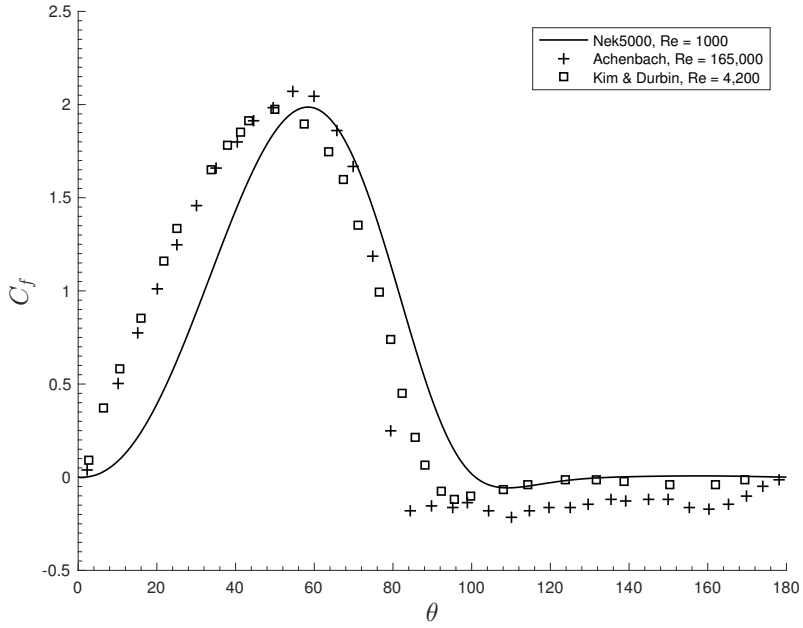

Figure 3.6: Profile of the skin-friction coefficient on the sphere surface.

it is observed that profile for C_f in the current simulations is consistent with experimental data, but that the profile is shifted towards the downstream angular points. This may be explained by the difference in Reynolds number, where higher values will lead to the boundary layer separation point, defined by the the angular location where $\tau_w = 0$, moving forward on the pebble surface. This is confirmed by tabulated results in [19]. Additionaly, the angular point of separation for our simulation matches the computational results in [18] very well. For the same Reynolds number, they report a separation angle of $\theta = 102°$, while the current results show a value of $\theta = 101°$.

The presented verification results indicate acceptable results from the simulation.

3.3 Results and discussions

Selected results from the two numerical cases are presented in the following subsections.

3.3.1 First and second order statistics

The first- and second-order turbulence statistics presented here was averaged for the total time integration period achieved during production. An established practice for computational studies of flow over spherical bluff bodies is to average interpolated line profiles azimuthally around the domain axial center line to obtain well averaged statistics. This is justified by the assumption that the statistics develop to a time-invariant, azimuthally symmetric condition as the time integration period increases. However, based on the results presented in [21], it is observed that this is assumption is not necessarily valid for flow geometries that feature multiple spherical bluff bodies, even for long periods of time integration. While the geometries presented in this study are simplified when compared with those detailed in [21], it is believed that similar metastable behavior, characterized by low-frequency switching of the azimuthal location of the highest magnitude of the statistics, might also occur for these simpler geometries. It is expected that this to particularly be true for the case with two spheres.

Since azimuthal averaging has not been implemented here, a longer period of time integration was required to obtain acceptably stationary statistics. Based on a review of studies similar to that performed here [19, 18], the total integration time of 1120 convective units was deemed to be sufficient to compensate for this.

Pseudo-color fields of the averaged stream wise velocity is shown in Fig. 3.7 for the $[x, 0, z]$ plane. It can be seen that for the single sphere case that $\langle U_z \rangle$ shows a symmetric profile around the axial center line. For the two sphere case, a generally

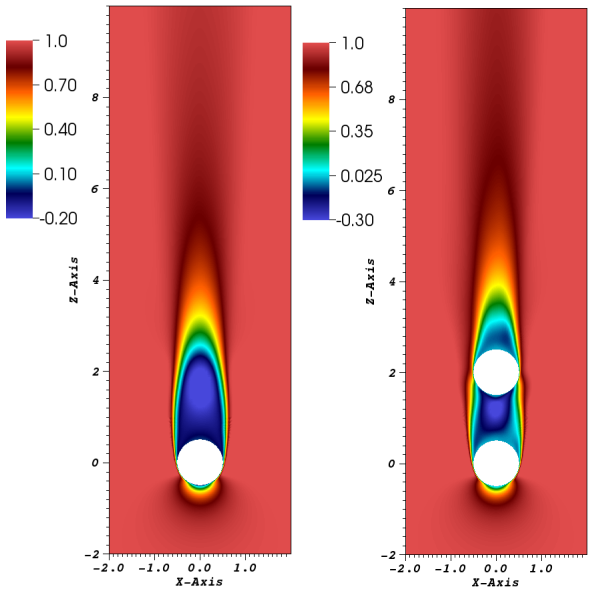

Figure 3.7: Pseudo-color field of $\langle U_z \rangle$ for the one (left) and two (right) sphere cases.

symmetric wake region behind the downstream sphere is also observed, but $\langle U_z \rangle$ does not have a symmetric solution in the gap area between the upstream and downstream spheres. Here, the larger magnitude of the recirculation velocity, i.e. $\langle U_z \rangle < 0$, is biased towards coordinate values of $x/L_D < 0$. Thus, an increased asymmetry in the averaged first-order statistics is observed for the case where a second, downstream sphere is present. The magnitude of the recirculation velocity for the two sphere case is also larger than for the single sphere case.

Since the simulations were conducted using a fluid density of unity, the Reynolds stress tensor is simply represented by the single-point, single-time covariance tensor, $\langle u_i u_j \rangle$. Figure 3.8 shows the $\langle u_z u_z \rangle$ component of the tensor for the two cases. While the solution for this component of the Reynolds stress looks nominally symmetric for the single sphere case, It can be seen that a significant asymmetry of this component of the Reynolds stress exists for the two sphere case in the $[x, 0, z]$ plane, even after

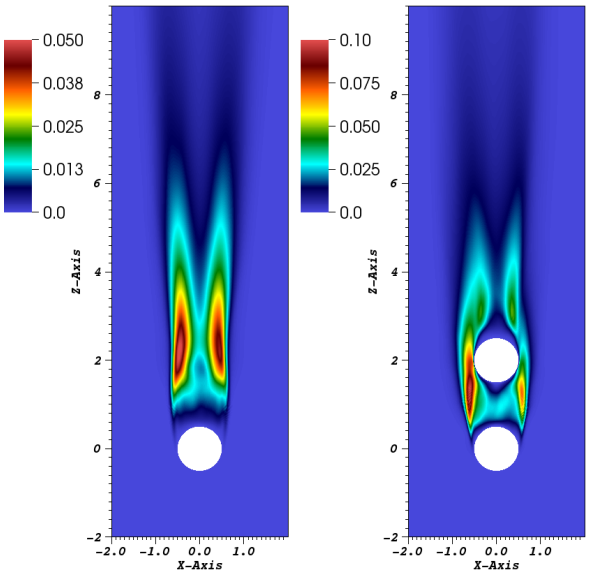

Figure 3.8: Pseudo-color field of the in-plane Reynolds stress component $\langle u_z u_z \rangle$ for the one (left) and two(right) sphere cases.

convergence to what would be classified as a stationary state. It can also be observed that the magnitude of the Reynolds stress is also increased due to the presence of the downstream sphere.

Figures 3.9 and 3.10 shows interpolated line profiles of $\langle u_z u_z \rangle$ in the near wake region for both cases. Each of the six lines consist of 100 individual interpolation points. A consistent set of markers between the location of the interpolation line and the profile is used, with top-left to bottom right for the interpolated line plots corresponding to bottom to top locations in the domain. The interpolated data is normalized for the six lines in each data series using

$$X_{norm} = max\left(max\left(|X_{i,j}|\right)_{i=1,100}\right)_{j=1,6} \tag{3.3}$$

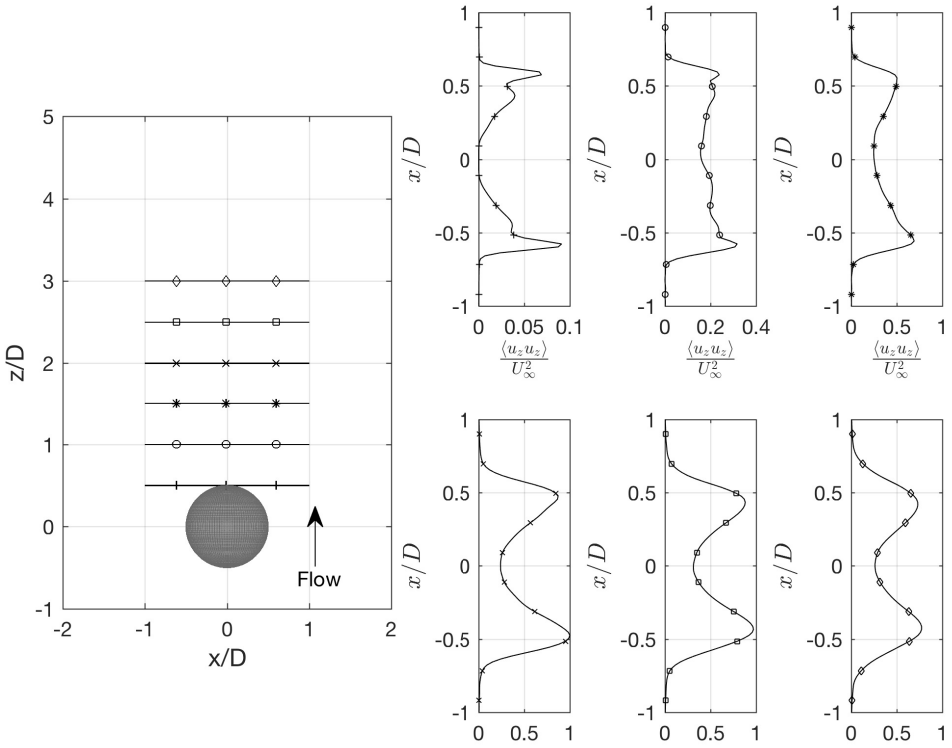

Figure 3.9: Line profiles of $\langle u_z u_z \rangle$ in the wake region of the single sphere. All lines normalized using the largest absolute value obtained from the six interpolation lines.

where X is the variable that is to be normalized. This normalization allows for the simplest representation of the the specific line profiles under consideration.

For the single sphere case, it can be seen that $\langle u_z u_z \rangle$ evolves from a low-magnitude, narrowly peaked profile for the interpolation line closest to the sphere, to a broader profile with a maximum magnitude at the $z/L_D = 2.5$ line. A slight asymmetry, with the maximum magnitude biased towards the $x/L_D < 0$ side can be seen.

For the two sphere case, the first interpolation line is qualitatively similar to the line at the same position for the single sphere case. The second and third lines,

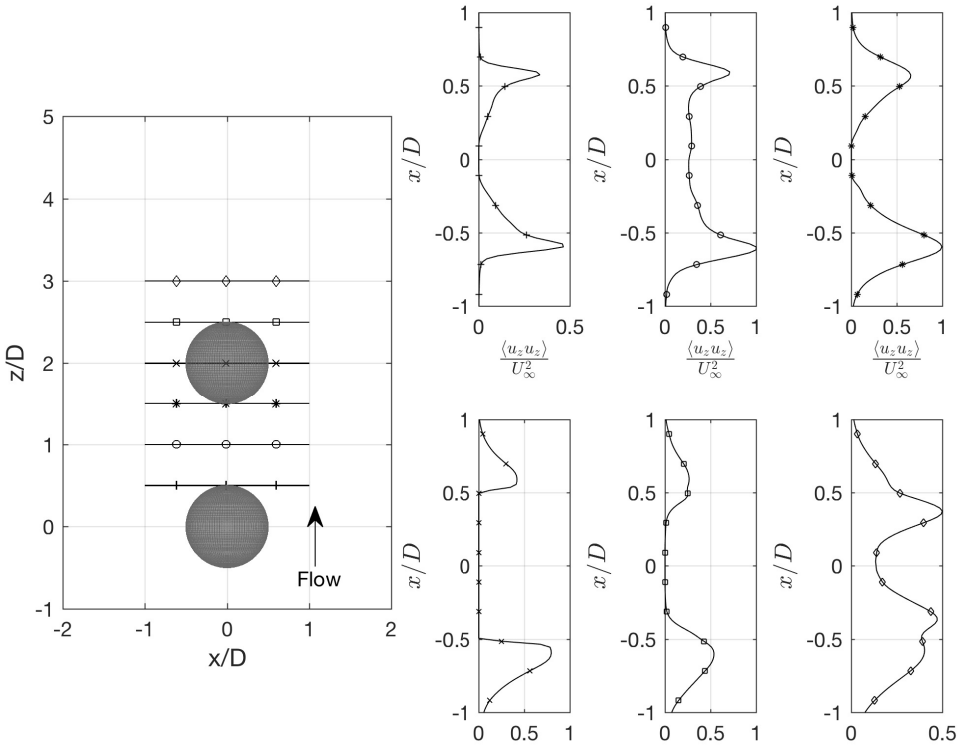

Figure 3.10: Line profiles of $\langle u_z u_z \rangle$ in the region close to the two spheres. All lines normalized using the largest absolute value obtained from the six interpolation lines.

located in the recirculation area between the upstream and downstream spheres correspond to the areas of highest Reynolds stress, with a clear asymmetry of the averaged profile biased toward $x/L_D < 0$ also being observable. Interestingly, for the final interpolation line behind the downstream sphere, the asymmetry has switched, although the magnitude of the shear stress is lower for this interpolated line.

From the presented statistics, it is evident that the addition of a second sphere indeed increases the level of asymmetry observed in the nominally steady solution.

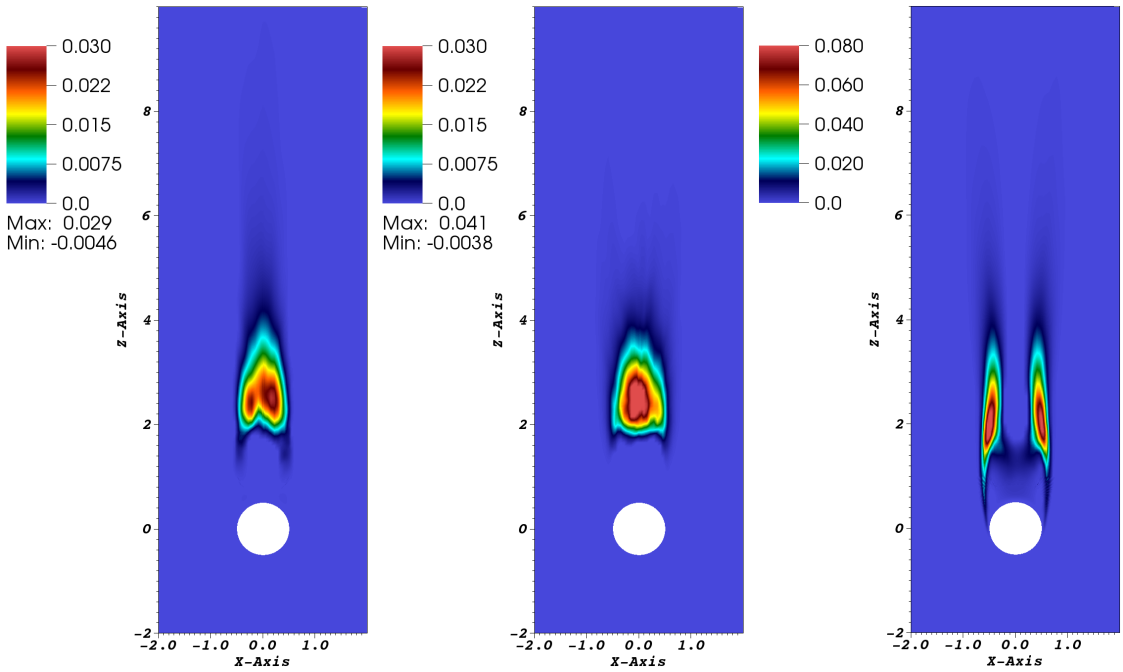

(a) $\mathcal{P}_{xx}$ (b) $\mathcal{P}_{yy}$ (c) $\mathcal{P}_{zz}$

Figure 3.11: Pseudo-color field of the diagonal components of the turbulent kinetic energy production tensor for the single sphere case in the $[x, 0, z]$ plane.

3.3.2 Turbulent kinetic energy

Selected components of the turbulent kinetic energy transport equation terms are presented. The selected terms are the production and dissipation tensors.

The structure and the magnitude of the production components $\mathcal{P}_{xx}$ and $\mathcal{P}_{yy}$ are similar, as shown in Figs. 3.11a and 3.11a. For $\mathcal{P}_{zz}$, shown in Fig. 3.11a, the magnitude is higher, while a better converged structure is also observable. The position of the maximum magnitude is consistent over all three components, and reflects the location where the shear-layer Kelvin-Helmholtz (K-H) instability manifests on the periphery of the recirculation region. The stream wise component, $\mathcal{P}_{zz}$ also shows non-zero values beginning at the sphere surface where the wake separates from the

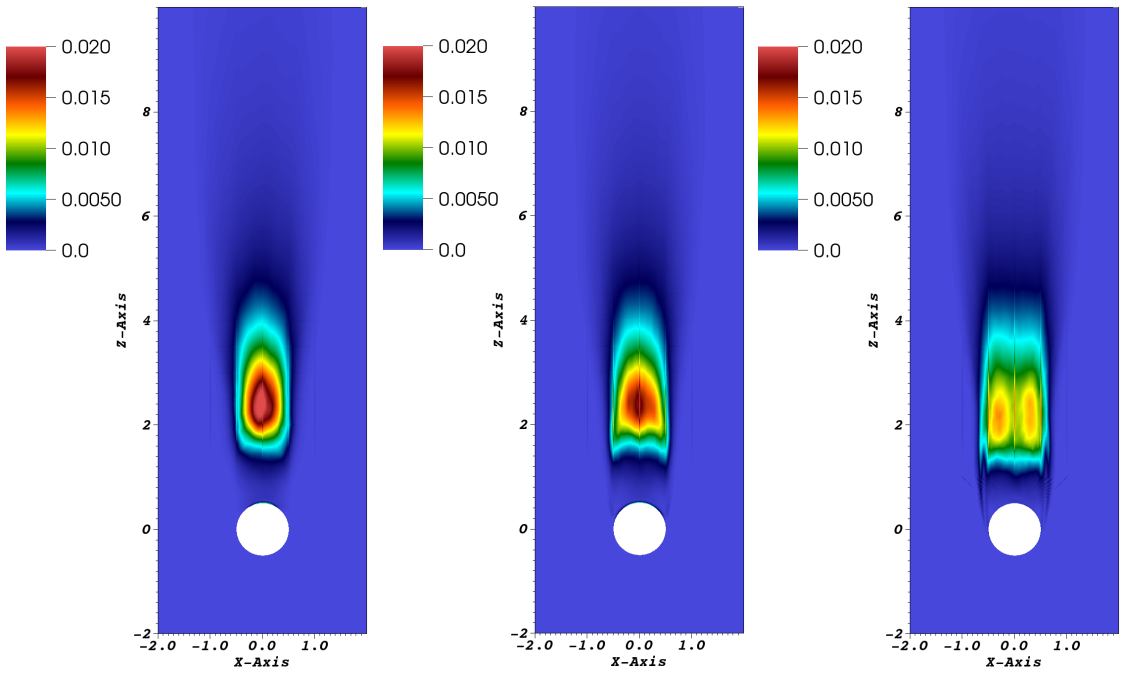

(a) ϵ_{xx} (b) ϵ_{yy} (c) ϵ_{zz}

Figure 3.12: Pseudo-color field of the diagonal components of the turbulent kinetic energy dissipation tensor for the single sphere case in the $[x, 0, z]$ plane.

sphere, showing the interaction between the low velocity recurculation zone and the free stream flow.

For the turbulent kinetic energy dissipation components shown in Figs. 3.12a, 3.12b, and 3.12c, the structure mirrors that of the production, showing a maximum in the dissipation in the area where the K-H instability causes the production of smaller structures in the wake.

For the two sphere case, the lateral production components $\mathcal{P}_{xx}$ and $\mathcal{P}_{yy}$ seem to exhibit similar structures which are rotated by 90° around the axial center line of the domain. The maximum magnitude of the production is focused on the stream wise front of the down stream sphere. When considering $\mathcal{P}_{zz}$, a clear asymmetry of magnitude of the production is apparent. This is consistent with increased asymmetry

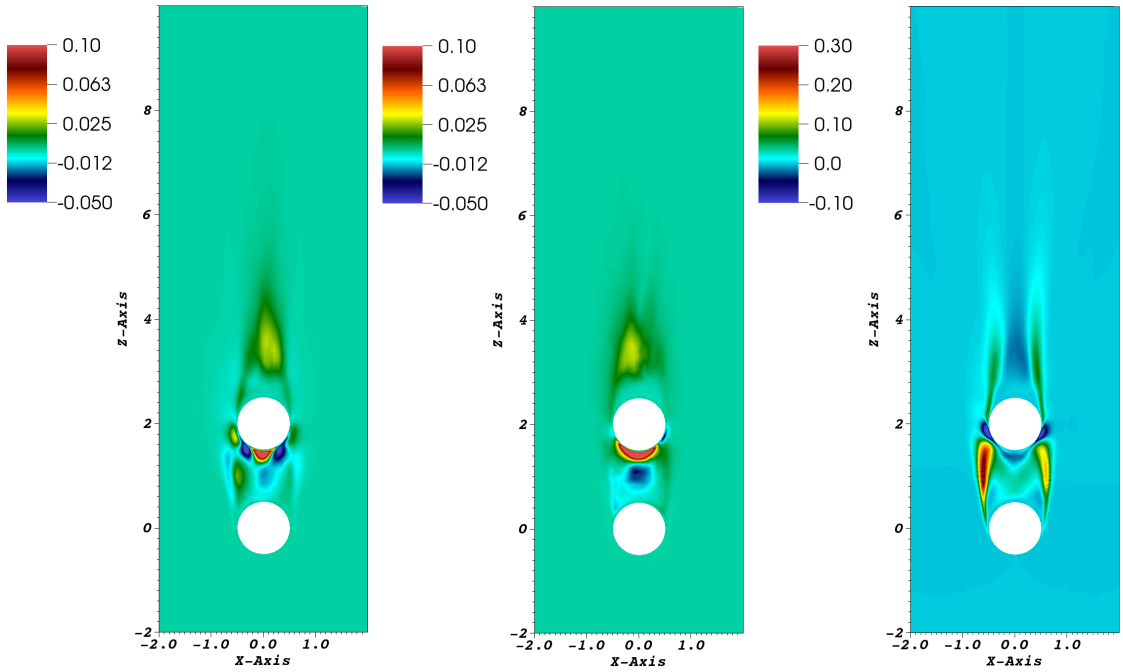

(a) $\mathcal{P}_{xx}$ (b) $\mathcal{P}_{yy}$ (c) $\mathcal{P}_{zz}$

Figure 3.13: Pseudo-color field of the diagonal components of the turbulent kinetic energy production tensor for the two sphere case in the $[x, 0, z]$ plane.

of the velocity profiles that was observed in §3.3.1.

The turbulent kinetic energy dissipation components for the two sphere case have maxima that are concentrated on the surface of the down stream sphere, making visualization difficult using pseudo-color fields. Thus, volume renderings are used to illustrate the structure of the dissipation tensor components in Figs. 3.14a-3.14c. The lateral components show a similar rotated agreement as observed for the production components in Fig. 3.13, while the stream wise component ϵ_{zz} shows a symmetric distribution on the surface of the down stream sphere.

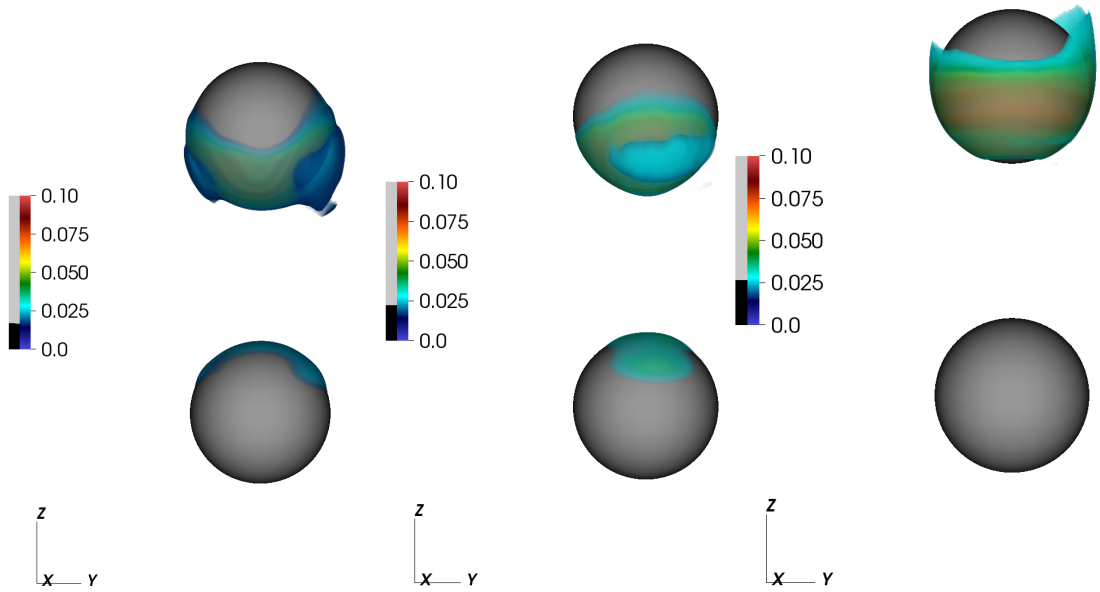

(a) ϵ_{xx} (b) ϵ_{yy} (c) ϵ_{zz}

Figure 3.14: Volume rendering of the diagonal components of the turbulent kinetic energy dissipation tensor for the two sphere case in the $[x, 0, z]$ plane.

3.3.3 Temporal auto- and cross-correlations

As an initial investigation of a potential difference in temporal shedding behavior between the two cases, the temporal auto-correlation function (ACF) and cross-correlation function of the time histories of the fluctuating stream wise velocity, u_z at two points in the shear layers of the two cases was calculated.

For both cases, the two points were selected from those defined in the time-history interpolation lines in the $[x, 0, z]$ plane discussed previously. For the single sphere case, the points for the correlations were selected at $z/L_D = 2$, and $x/L_D = \pm 0.5$. For the two sphere case, the points for the auto- and cross-correlation were selected to be between the upstream and downstream spheres inside the shear layer observed in Fig. 3.8, at $z/L_D = 1$, and $x/L_D = \pm 0.6$. The temporal auto-correlation function

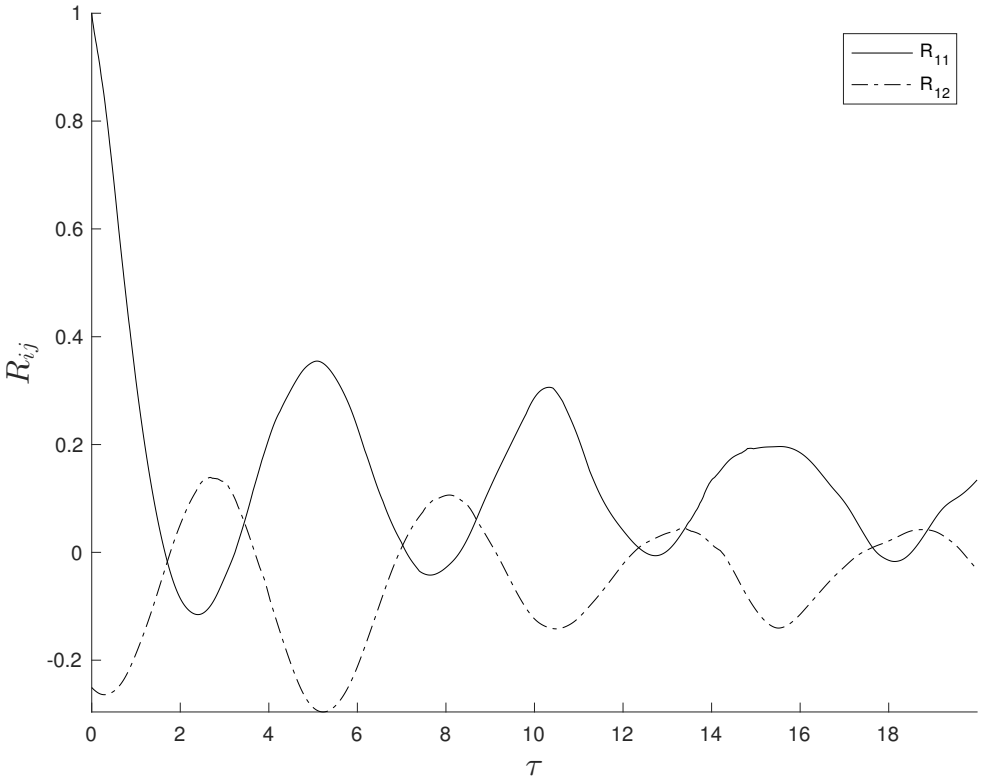

Figure 3.15: Temporal auto- and cross-correlation functions for the single sphere case.

is defined as

$$R_{ii}(\tau) = \lim_{T\to\infty} \frac{1}{T} \int_0^T u_i(t) u_i(t+\tau) dt, \tag{3.4}$$

where the index defines the point under consideration and u_i is the instantaneous fluctuating velocity at that point. Similarly, the temporal cross-correlation is defined as

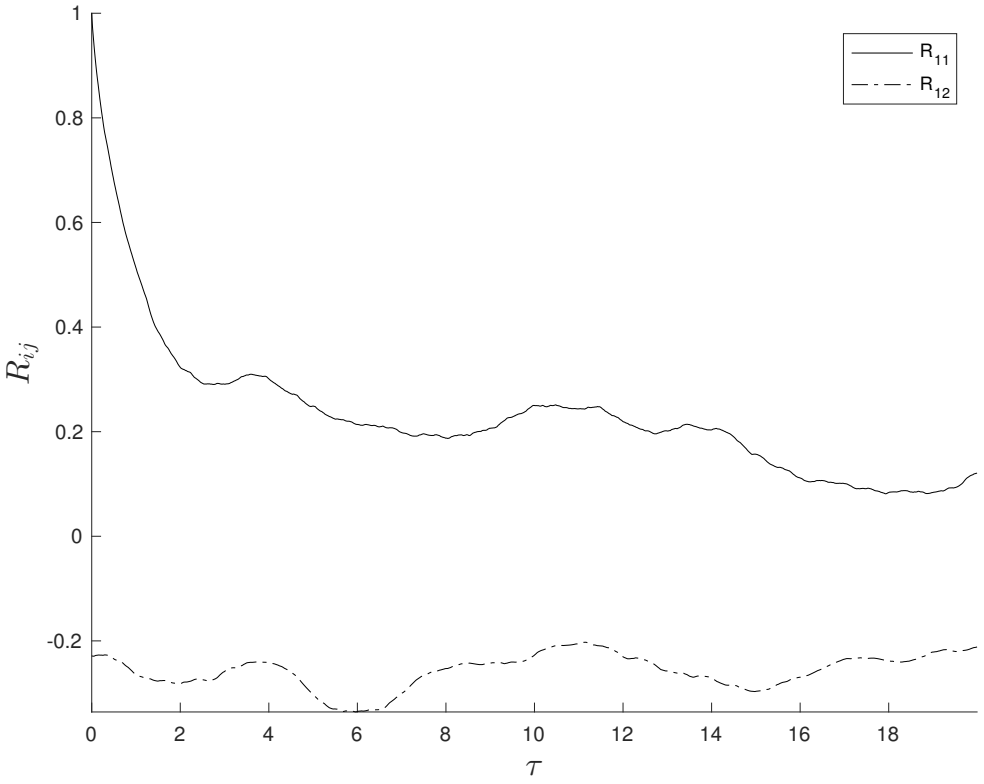

Figure 3.16: Temporal auto- and cross-correlation functions for the two sphere case.

$$R_{ij}(\tau) = \lim_{T\to\infty} \frac{1}{T} \int_0^T u_i(t) u_j(t+\tau) dt, \tag{3.5}$$

where u_i and u_j are again the instantaneous fluctuating velocities at the two points. All the lines are normalized using the product of the $\tau = 0$ shifted auto-correlation coefficients for u_i and u_j:

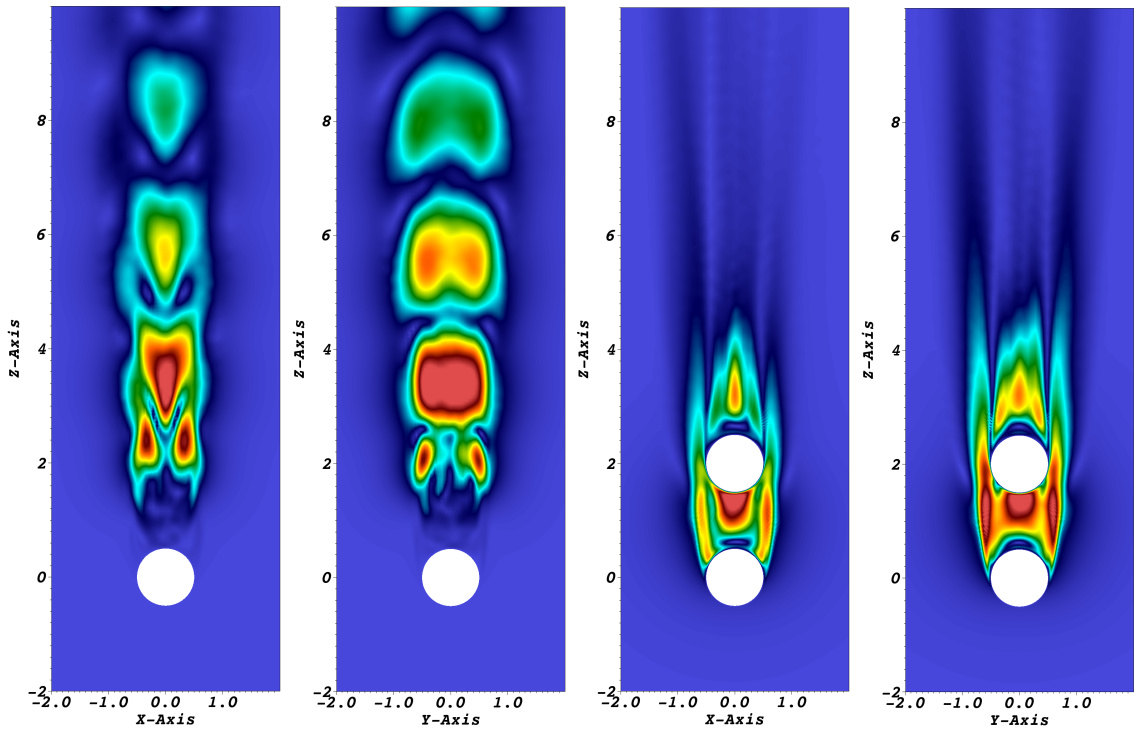

(a) One Sphere: $[x, 0, z]$ plane.

(b) One Sphere: $[0, y, z]$ plane.

(c) Two Sphere: $[x, 0, z]$ plane.

(d) Two Sphere: $[0, y, z]$ plane.

Figure 3.17: Pseudo-color field of the mode 1, i.e. highest energy, POD eigenfunctions.

$$R_{ij}(\tau) = \frac{R_{ij}(\tau)}{\left(R_{ii}(0) R_{jj}(0)\right)^{1/2}}. \tag{3.6}$$

It can be observed for the single single sphere case, shown in Figs. 3.15 and 3.16, that both the auto- and cross-correlations exhibit fluctuations as the time shift is increases, consistent with the shedding of the vortex from the back of the sphere. The same phase angle shift observed in [18], who showed that a difference

in azimuthal position is related to a difference in the phase angle between the points under consideration, was observed here. They attributed this to a potential azimuthal rotation mechanism affecting the wake separation region, which was also suggested by [22].

Figures 3.15 and 3.16 shows the auto- and cross-correlations for the two sphere case between the points defined previously. A marked difference in the qualitative behavior can be observed between these correlations and those seen in for the single sphere case. The fluctuations observed for the single sphere case is not present here. The auto-correlation shows the expected initial decorrelation, after which it remains relatively constant for the available time-shifted data. The cross-correlation fluctuates relatively stably around a fixed negative correlation value.

Based on the observations made above, it may be hypothesized that if there is indeed a cyclic wake-separation mechanism present for the two sphere flow case, that the frequency at which this mechanism is active is much lower than for the single sphere case. However, the data presented is not sufficient for any definitive conclusions. In continued studies, an increase in the available time-shifted data and the number of azimuthal points that are monitored will help investigate this behavior further.

3.3.4 Proper orthogonal decomposition

The method of proper orthogonal decomposition allows for the definition of coherent structures in a turbulent flow field as a function of spatial variables that has maximum energy content. The spatial variable in the case of turbulent flows is the turbulent kinetic energy. The POD algorithm used in Nek5000 follows the snapshot method, and the details of the implementation may be found in [17].

For both cases, 1,200 snapshots of the instantaneous flow domain was saved every

100 time steps, i.e. at intervals of 0.4 CU. Since the flow Reynolds number is low, and thus the turbulent energy at high wave numbers negligible, it was deemed the number of snapshots sufficient for identifying the highest energy structures.

Figures 3.17a and 3.17b show the magnitude of the mode 1, i.e. most energetic, POD eigenfunctions for the single sphere case in the $[x, 0, z]$ and $[0, y, z]$ lateral planes. The cyclical shedding structure can be observed in both figures, where discrete and equally spaced energy cells with decreasing magnitude as they move further from the sphere can be seen in the wake of the sphere. It is observed that the structure of the mode differs between the two lateral planes under consideration. While more lateral planar fields for comparison here have not been extracted here, it is evident that the highest energy coherent structures in the field are not azimuthally symmetric around the domain axial center line for the 480 CU over which the POD was calculated. This is consistent with the observations made in [22, 18] regarding an azimuthal rotation of the vortex shedding cell.

The mode 1 eigenfunctions for the two sphere case are shown in Figs. 3.17c and 3.17d. From these figures, it can be seen that the wake vortex structures seen in the single sphere case is suppressed by the second sphere, leading to a qualitatively different concentration of the highest energy coherent structures for this case. In this case, the maximum energy in mode 1 is concentrated at the front of the downstream sphere and in the shear layer at the interface of the recirculation cell between the upstream and downstream spheres and the higher velocity positive stream wise flow outside the cell.

In terms of azimuthal symmetry, the two sphere case shows a more symmetric structure for mode 1, although the magnitude of the energy is higher in the $[0, y, z]$ plane. This observation is again consistent with a possible lower frequency rotational mechanism associated with the boundary layer separation.

3.4 Conclusions

Selected results from the simulation of incompressible flow over a single and two spheres at $Re = 1000$ has been presented. Several verification and validation results for flow over a single sphere were presented to establish confidence in the numerical results.

This work may be considered as an initial extension of the canonical case of flow over a single sphere. Of specific interest is the change in temporal dynamics of the flow when additional spheres are added. the results show that the addition of a second sphere results in a marked increase in the asymmetry of turbulence statistics, even for long periods of time integration. This is consistent with the results from studies of higher Reynolds number flows through domains consisting of regularly ordered spheres, which will be discussed in the next section.

In terms of results, a non-exhaustive selection of first-second order statistics were shown that illustrate the increased level of asymmetry of the flow statistics resulting from the addition of a second sphere downstream from the first. The difference between the temporal vortex shedding behavior of the two cases was discussed by comparing the temporal auto- and cross-correlations at selected points in the wakes. Finally, a set of results generated by a POD of the turbulent flow field was discussed to illustrate the qualitative difference in the structure of the highest energy coherent structures between the two simulations. A marked decrease in the formation of a vortex street was observed for the two sphere case.

Continued work will focus on refining the quantification of the temporal effects of the additional sphere. Potential methods of analysis include dynamic mode decomposition and spectral-POD, which are similar to the POD done in this study, but better quantify the temporal dynamics. A linear stability analysis will also be

performed to help identify the laminar to turbulent transition mechanism for the two cases and identify any potential differences between them.

4. NUMERICAL EXPERIMENT II: FCC UNIT CELL AND EXPANDED DOMAIN*

This section presents results for the FCC unit cell case and an expanded domain based on this unit cell. This study was chronologically the first study to be conducted during the dissertation research. Upon identification of meta-stable behavior that will be discussed in more detail subsequently, the study of the single two sphere case presented in the previous section was done to determine whether this meta-stable behavior could be reproduced.

A similar structure of presentation to the previous study is followed, consisting of background regarding the problem and it's importance, a discussion of the methodology, presentation of results and discussions, and finally conclusions.

4.1 Background

The very high temperature reactor (VHTR) is a reactor concept proposed by the Generation IV International Forum as a potential successor to currently operating generation II and III nuclear reactor systems. Pebble bed high temperature reactors (PBR) form a sub-class of the VHTR concept, with the other being prismatic block type. These designs incorporate advanced design features that enable enhanced passive safety and efficiency [3, 4].

The reactor core in a PBR consists of either a cylindrical or annular core geometry randomly packed with on the order of hundreds of thousands of graphite spheres, in which tristructural isotropic fuel is particles are dispersed. An online refueling

*This section contains results previously published in the ASME Journal of Fluids Engineering [21].

system may be utilized where pebbles are removed from the bottom of the core at a rate of singular pebbles per day and reinserted at the top of the core until reaching their cycle limit. Alternatively, a more conventional offline refueling strategy is also possible.

PBR systems may use either an inert gas, such as helium, or molten salt as primary loop coolant. Depending on the coolant type, secondary and tertiary energy conversion loops may be used to provide thermal energy for chemical processes such as hydrogen cracking, power generation using either Rankine or Brayton cycles, or a combination of the two in co-generation.

To successfully design a nuclear reactor system, a detailed understanding of the fluid flow through the core geometry is essential. Since the PBR core geometry consists of a randomly packed bed, which means an extreme level of geometric curvature, this type of reactor design features one of the most complex flow geometries in any nuclear reactor system. This fact has historically hampered both detailed experimental [25] and computational studies [7]. This fact has led to the implementation of heuristic design philosophies that rely on macro-scale data to develop empirical correlations for the calculation of parameters of engineering interest such as pressure drop and temperature distributions. Certain correlations [26] remain highly referenced today, where they are used to benchmark the accuracy of computational tools in calculating macro-scale effects.

With increased emphasis on detailed analyses of physical effects and a more stringent regulatory framework, the level of information provided by such correlations alone may not be sufficient in the modern design of new nuclear reactor systems. Fortunately, a substantial increase in computational capabilities in recent years, coupled with the maturation of CFD as a research and design tool, enables increasingly detailed simulations and analyses of complex flow domains such as those encoun-

tered in PBR systems. Tools exist that cover the range of scales encountered in PBR systems, from the total system scale which is usually treated in a one dimensional fashion [27, 28] , to the pebble scale, where detailed three-dimensional CFD simulations may be conducted [29].

CFD analyses of pebble bed flows is complicated by a number of challenges. The large degree of geometric curvature in PBR beds leads to blunt body effects such as flow separation and reattachment, which remains a challenge for RANS based turbulence models that are generally employed in commercial CFD packages. Thus far, limited success has been achieved when using these codes to performed detailed flow analyses [30]. Further compounding this problem is a general lack of detailed, i.e. two- or three-dimensional, experimental data which may be used for validating RANS-based tools. This is again due to the complexity of pebble bed flow domains, which complicate experimental procedures and the capture of detailed data inside pebble beds [31].

High-fidelity simulation schemes such as LES and DNS are better suited to accurately simulate the flow effects in pebble bed flow domains. LES explicitly solves for the majority of the turbulent length scales in a given flow, while modeling the dissipation scales, while DNS explicitly solves for all the turbulent length scales up to and beyond the dissipation scales. These frameworks are thus less, or completely independent of the modeling assumptions required in RANS-based approaches [32]. Commensurate with the additional level of resolution provided by LES and DNS over RANS, their computational cost are much increased. An attractive objective is therefore to use these better-resolved schemes to develop a detailed understanding of physics in pebble bed fluid flow using suitable prototypical cases. This increased understanding of the physics may then be used to inform the optimization of RANS-based tools so that they may more accurately simulate flows in pebble bed

geometries.

Although LES resolves the majority of the length scales in turbulent flows, they are still dependent on the modeling of the so-called sub-grid, or dissipation scales. Thus, LES is not completely free of modeling assumptions, which leaves DNS as the only viable framework for the detailed analysis of pebble bed flows and the development of high-fidelity reference data which may be used as pseudo-experimental data for validating data obtained by using RANS methods.

This section outlines the development of a DNS database for incompressible, isothermal flow through an expanded FCC unit cell pebble bed structure. The database comprises data sets generated by using differing degrees of spatial discretization. The purpose of using multiple orders of spatial discretization was to to ensure explicit conformance to DNS requirements and to prove the validity of using Kolmogorov theory as a measure for this conformance. Temporal analyses were done to verify the consistent behavior across the developed data sets. Selected comparisons between data generated using the differing orders of discretization are presented, as well as tests for statistical stationarity of the data sets. The results from the data sets are also cross-verified using available quasi-DNS data.

Finally, an observed low-frequency fluctuating behavior of the temporally averaged data is investigated. This is done by performing additional simulations in an enlarged FCC flow domain and implementing ensemble averaging instead of time-averaging, after which the results obtained using the differing methodologies are compared.

4.2 Methodology

This subsection presents the research methodology. The problem scope, computational aspects, discretization, and simulation parameters are described.

4.2.1 Outline

The flow domain under consideration is an extended, single FCC unit cell. All the pebble surfaces are treated as no-slip walls. Since the domain is idealized and features a set minimum spacing between pebbles, it is classified as an extended FCC unit cell.

The spacing between the pebbles considered in this computational study does not exist in practical VTHR systems. Thus, the flow geometry considered here must be seen as idealized. Fortunately, complex flow effects such as separation and attachments still manifest in this idealized geometry. These effects have not been quantified using high-fidelity numerical simulation tools such as LES or DNS in any significant manner based on a review of literature. The investigation of blunt body flows using these tools have generally been limited to idealized flows such as those treated in §3. Examples of such studies are included in the references [33, 19, 20]. Thus, the idealized FCC geometry treated in this section may be seen as a valid starting point for high-fidelity investigations of pebble bed geometries, after which additional complexity may be added in subsequent studies. This geometry also allows for cross-verification of results with the data generated by Shams et al. [29].

The FCC geometry features eight $1/8$ pebble sections at the domain corner vertices. Each face features a $1/2$ pebble section. The FCC unit cell thus consists of a total of four complete spheres. Figure 4.1 shows an example the instantaneous velocity magnitude of the turbulent flow field during simulation.

Figure 4.2 shows the position of the $[x, 0, z]$ and $[0, y, z]$ lateral planes where the majority of the results that will be subsequently shown is obtained from. This choice is completely arbitrary, since data from the entire field are available for analysis. The domain is centered around the $[0, 0, 0]$ coordinate. All spatial coordinates are

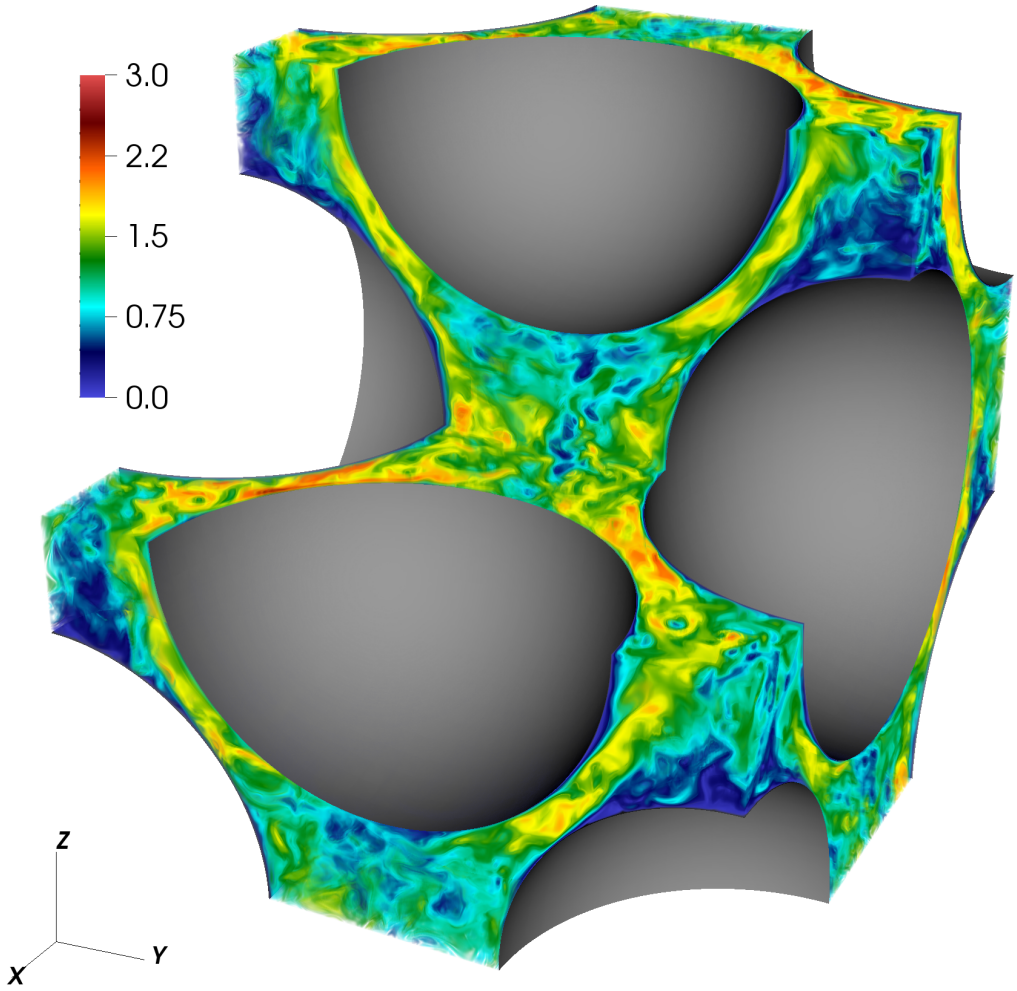

Figure 4.1: Volume rendering of U_{mag}. The cut away section is defined for the region $-1 \leq y \leq 0$ and $0 \leq z \leq 1$.

normalized using half the domain length, L_D. Table 4.1 provides physical dimensional data, obtained from [29], as well as the equivalent normalized geometric data used in this study.

The domain boundary conditions are all periodic, and thus approximate a physical domain located at the center of a practical pebble bed core where the effects of inflow, outflow, and wall boundaries may be considered negligible.

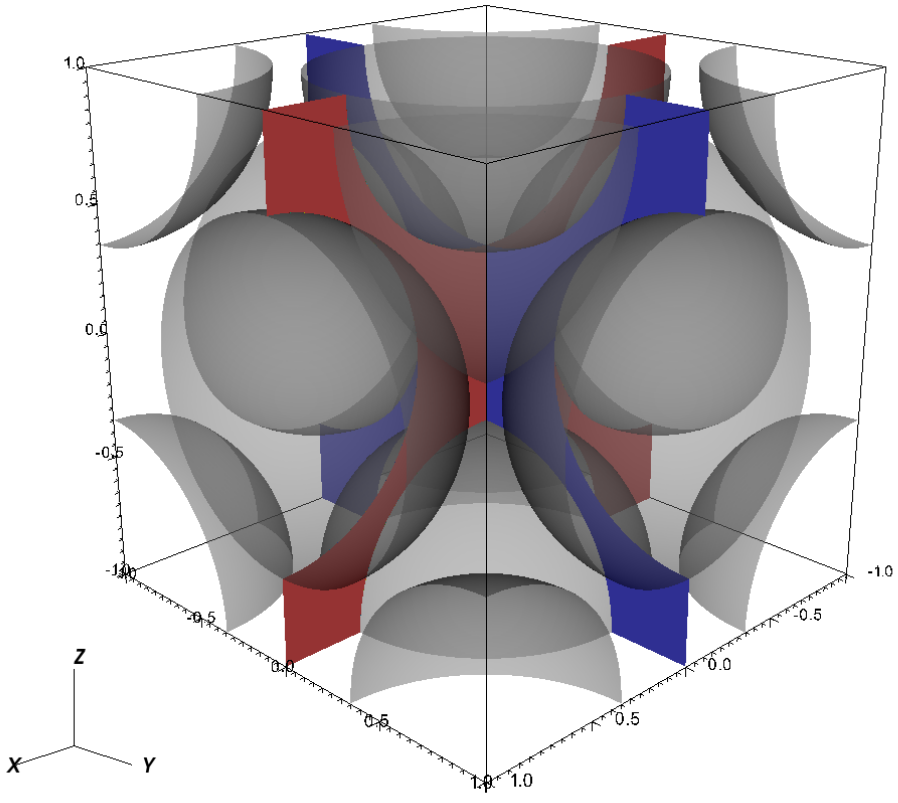

Figure 4.2: Position of the $[x, 0, z]$ and $[0, y, z]$ lateral planes in the domain.

4.2.2 Interpolation

Figure 4.3 illustrates the naming convention and locations of the arbitrarily chosen interpolation lines and time history probes in the domain for the $[0, y, z]$ plane. The same layout is used in the $[x, 0, z]$ plane. The data presented in the following subsections are collected from these locations

The interpolation line locations in each plane was chosen so that there would

Table 4.1: Geometric data: FCC unit cell

Parameter	Physical	Normalized
Domain length	91.924 $[mm]$	2 [-]
Inlet area	2795 $[mm^2]$	1.323 [-]
Pebble diameter	60 $[mm]$	1.305 [-]
Pebble gap spacing	5 $[mm]$	0.108 [-]

be at least one set of interpolation data in each plane that was normal to a specific pebble surface. The length of each line presented in the results is presented as L, with the specific point on each line represented by δ. All the line lengths are normalized to one for simpler representation.

The naming convention uses a three letter identifier:

1. Top [T] or bottom [B], corresponding to the streamwise-positive ($z > 0$) or streamwise-negative coordinates ($z < 0$).

2. Right [R] or left [L] of the domain, corresponding to the positive ($x, y > 0$) or negative lateral coordinates ($x, y < 0$).

3. Lateral flow plane under consideration [X], corresponding to the $[x, 0, z]$ plane, or [Y], corresponding to the $[0, y, z]$ plane.

4.2.3 Computational considerations

The computational mesh was generated by using Prenek, a meshing tool native to Nek5000, and consists of 28,672 fully hexahedral elements. Figure 4.4 shows a section of the $N = 13$ mesh, that is, thirteenth-degree mesh in the $[x, 0, z]$ plane.

The SEM is advantageous for DNS, because it exhibits little numerical dispersion and dissipation [34], and has been extensively validated [32]. Temporal advancement

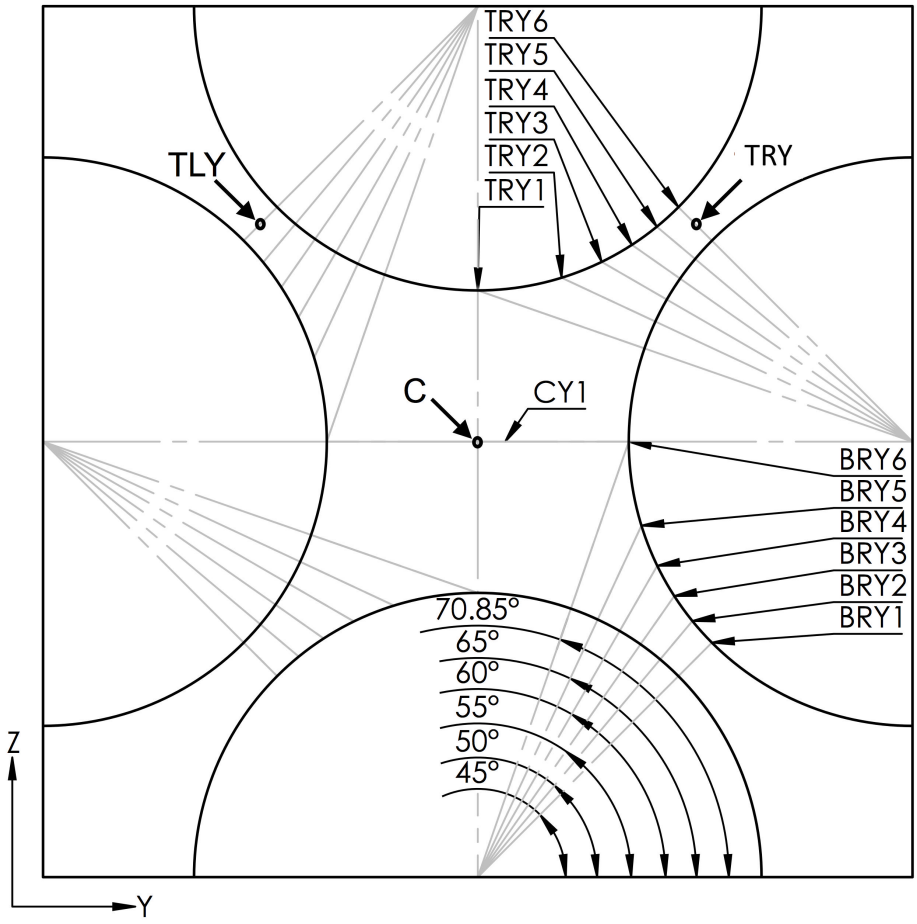

Figure 4.3: Naming convention and locations of the arbitrarily defined interpolation lines and point probes.

of the Navier-Stokes equations is carried out by using an implicit, third-order, backward differentiation (BDF3) scheme for the viscous terms and a third-order, explicit extrapolation (EXT3) scheme for the nonlinear terms. Readers are referred to §2.2 for additional details regarding the time-stepping scheme.

To speed up the development of stationary turbulent flow conditions, fifth-degree polynomials were used to allow for rapid time-stepping. The flow was allowed to develop for 150 convective time units (L_D/U), where each flow unit corresponds to half

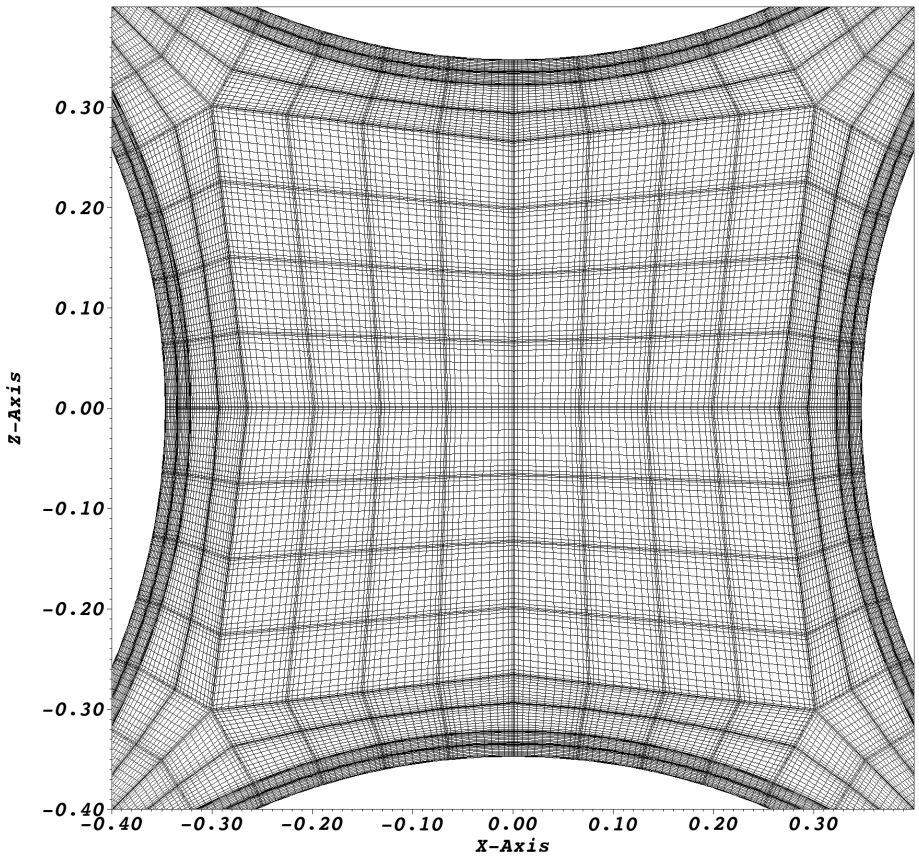

Figure 4.4: Section of the spectral-element mesh after sub-discretization, illustrating the central pebble gap area.

a flow-through time (FTT). Using the flow profile obtained from the fifth-degree development runs, production runs were run concurrently using seventh-degree, ninth-degree and thirteenth-degree discretization. A fixed Δt, shown in Tab 4.2, were used to ensure that the CFL number remained below 0.6.

The simulations were performed on an IBM Blue Gene/Q cluster operated under lease by the Texas A&M University High Performance Research Computing department. The balance of the required computations and post-processing was done on the systems operated by the Argonne Leadership Computing Facility, located at

Table 4.2: Computational parameters: FCC case

	Polynomial degree		
Parameter	7^{th}	9^{th}	13^{th}
Time step length	2.5×10^{-4}	1.5×10^{-4}	1.0×10^{-4}
Collocation points	14.68×10^{6}	28.67×10^{6}	78.68×10^{6}
Nodes (Cores)	128 (2048)	128 (2048)	256 (4096)
Total FTT	1260	300	77
Core hours	3×10^{6}	3.5×10^{6}	10.5×10^{6}
Hours/FTT	2,381	11,667	136,364

Argonne National Laboratory.

4.2.4 Discretization

From turbulence theory, a recognized test for confirming that the numerical discretization of the Navier-Stokes equations meets the required criteria to be termed a DNS, is the discretization of the problem beyond the Kolmogorov length scales of the flow in question. The Kolmogorov scales are discussed in §2.4. During the initial scoping runs before the initiation of the data set production runs, a number of runs using different polynomial degrees were conducted. During these runs, the TKE dissipation and Kolmogorov scales were calculated at each point in the computational domain, with the global minimum and maximum values being exported for comparison with the temporal and spatial discretization parameters for the runs.

For the case of $N = 7$, a total of 10.08E6 time steps were simulated. Taking the average of the minimum calculated Kolmogorov length scale in the domain for the available time history, a value of 7.89E-4 was obtained. The maximum grid spacing in the domain was constant and equal to 4.6E-4. Thus, the maximum grid spacing remains smaller than the smallest length scale in the domain by more than a factor of

1.5. For the time scale, the constant time step length of 2.5E-4 seconds was smaller than the average maximum Kolmogorov time scale by at least an order of magnitude.

Because the seventh-degree data already exceeded the requirements for DNS based on Kolmogorov theory, the higher order runs would by extension also conform to the requirements for DNS. Because the simulation parameters for the cases under consideration did not fully match those used in the formulation of Kolmogorov theory, an additional check on DNS conformance could be performed by explicitly comparing the data from the sets of differing discretization. This is analogous to a grid-independence study.

4.2.5 Turbulent time scales

The temporal ACF allows for characterizing the time scales over which turbulent motion at a point in the domain is correlated with itself. The ACF was used to calculate and confirm that the three data sets delivered a consistent evolution of the fluctuating velocity, that is, was sufficiently resolved in time. The ACF is plotted for u_{mag} at the XTR probe point in Fig. 4.5. The fluctuating velocity for the final half-million data points was extracted from the total time history for analysis for each data set. For each data set, 30,000 lag increments were used to calculate the ACF. Acceptable agreement was observed between the data sets, indicating sufficient temporal resolution for all the data sets. The ACF decays to an asymptotic state of minimal correlation, $r(\tau) \leq 0.1$, after $\tau \approx 0.2$ FTT, where the numerical value of τ is normalized to represent a single FTT. Since a strong mean flow gradient is present in the contracted space at the point surrounding the minimum distance between pebbles, it is expected that a low level of correlation persists for increasing values of τ.

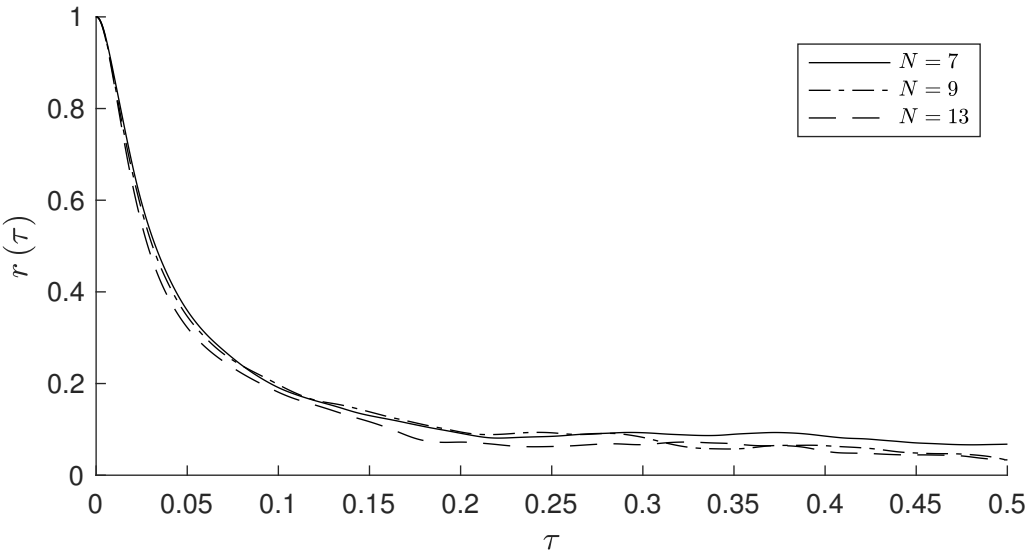

Figure 4.5: Temporal ACF for time history of u_{mag} at the XTR probe point.

4.2.6 Statistical stationarity

Differing FTTs were achieved for the simulations depending on their polynomial deree. During production, a standard checkpoint save and restart methodology was used. Checkpoints for the seventh-, ninth-, and thirteenth degree runs were saved at 30, 6, and 1.8 FTT, respectively, corresponding to the number of time steps achievable in the set wall-clock time limits on the compute resource. To confirm the stationarity of the statistics, the averaged data was compared between each of the available checkpoints, with the time shift, τ, used to indicate the number of FTT separating each checkpoint.

Figures 4.6, 4.7, and 4.8 illustrate the convergence of the diagonal components of the velocity and Reynolds stresses for the ninth degree data set. The interpolation lines are drawn at the coordinates for which they are defined in the $[x, 0, z]$ plane. The naming convention detailed in Fig. 4.3 is used. The data set shows an acceptable

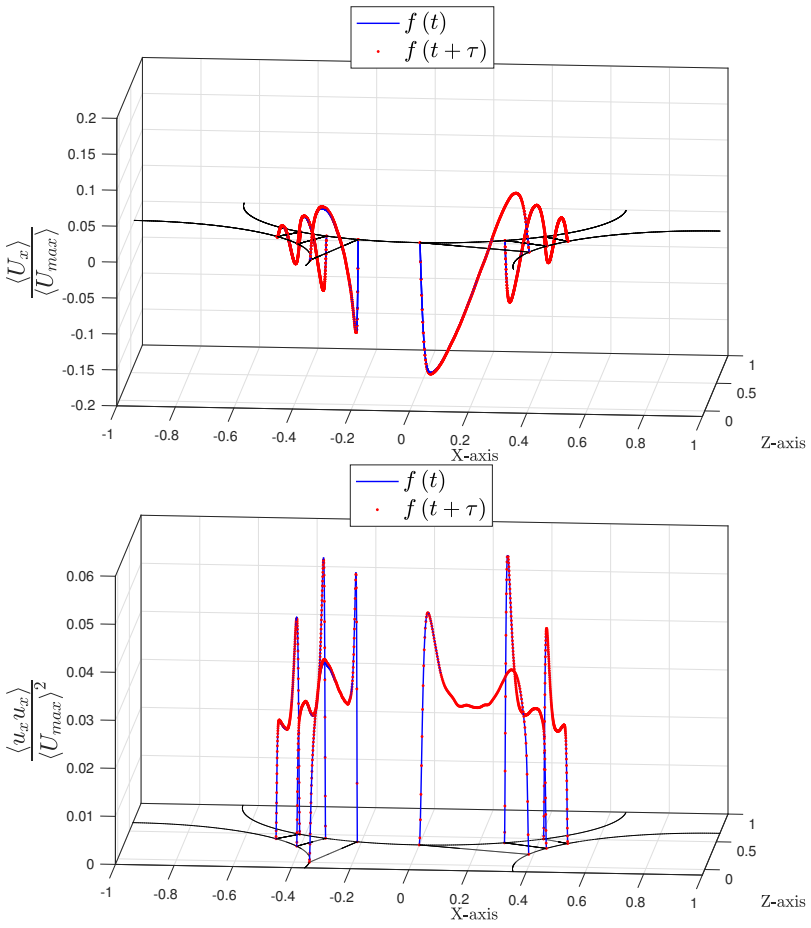

Figure 4.6: Interpolated profiles for $\langle U_x \rangle$ (top) and $\langle u_x u_x \rangle$ (bottom) profiles extracted at times $f(t) = 294$ FTT and $f(t+\tau) = 300$ FTT for the ninth-degree data set.

measure of stationarity for the choice of τ.

Due to the high computational cost associated with the $N = 13$ data set, only marginal stationarity was obtained for this data set. Thus, analysis of the data is limited to the two lower order data sets.

4.3 Results and discussion

This subsection presents selected quantitative and qualitative data. Initially, the generated data sets are compared in a fashion analogous to a grid independence

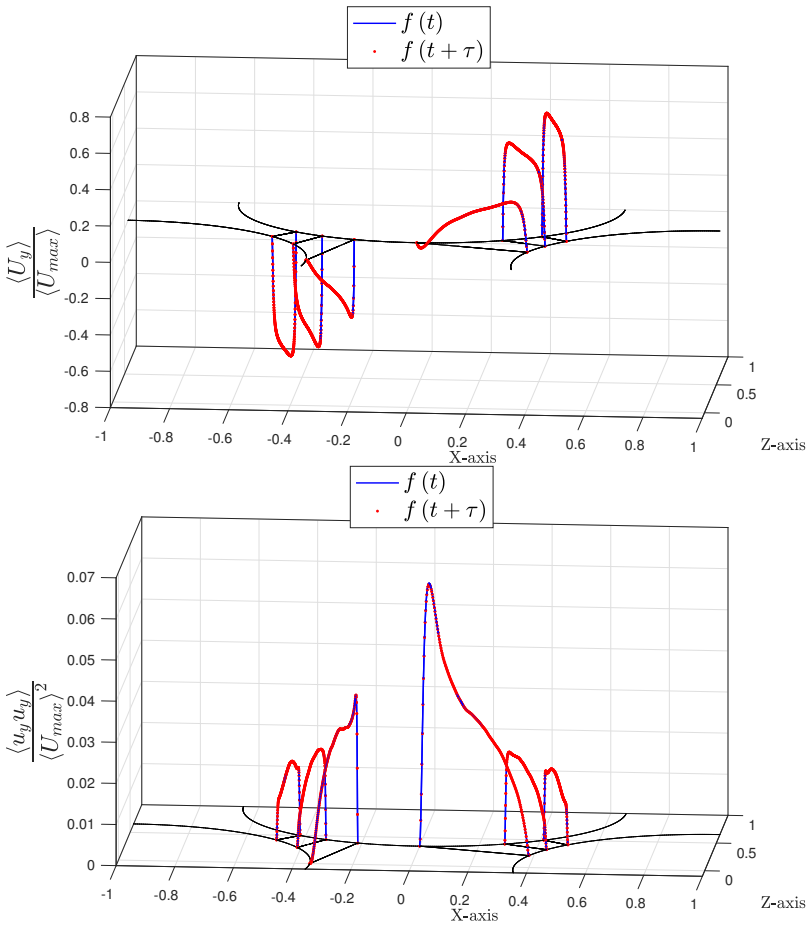

Figure 4.7: Interpolated profiles for $\langle U_y \rangle$ (top) and $\langle u_y u_y \rangle$ (bottom) profiles extracted at times t and $t + \tau$.

study. Cross-verification is then done using the quasi-DNS database of Shams et al. [29] as reference. An observed long-term, semi-oscillatory temporal instability is then investigated using the method of proper orthogonal decomposition. Finally, an expanded flow domain and ensemble averaging scheme is used to try and eliminate the asymmetry in the generated statistics.

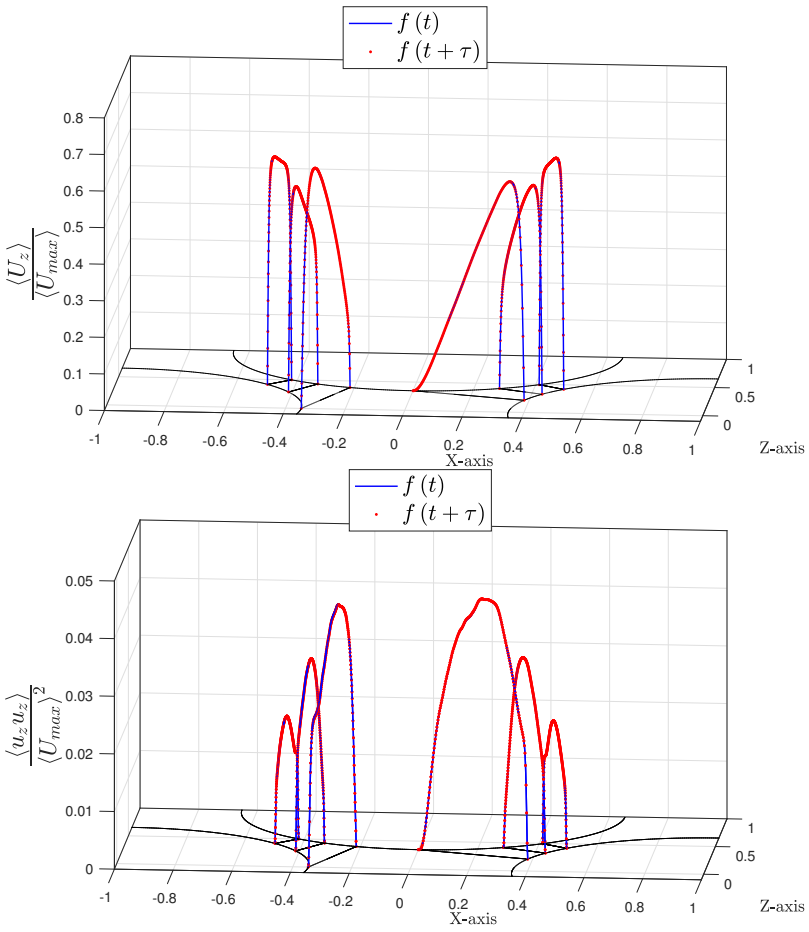

Figure 4.8: Interpolated profiles for $\langle U_z \rangle$ (top) and $\langle u_z u_z \rangle$ (bottom) profiles extracted at times t and $t + \tau$.

4.3.1 Inter-data-set comparisons

Figures 4.9, 4.10,4.11,4.12, and 4.13 present line interpolations of selected first- and second-order statistics for the TLX, TRX, BLX and BRX quadrants of the $[x, 0, z]$ plane. The interpolations are presented at the coordinates in the plane where they are defined, as per Fig. 4.2.

The profiles were normalized using the maximum value of the velocity magnitude in the plane under consideration. It is observable that both the velocity and the

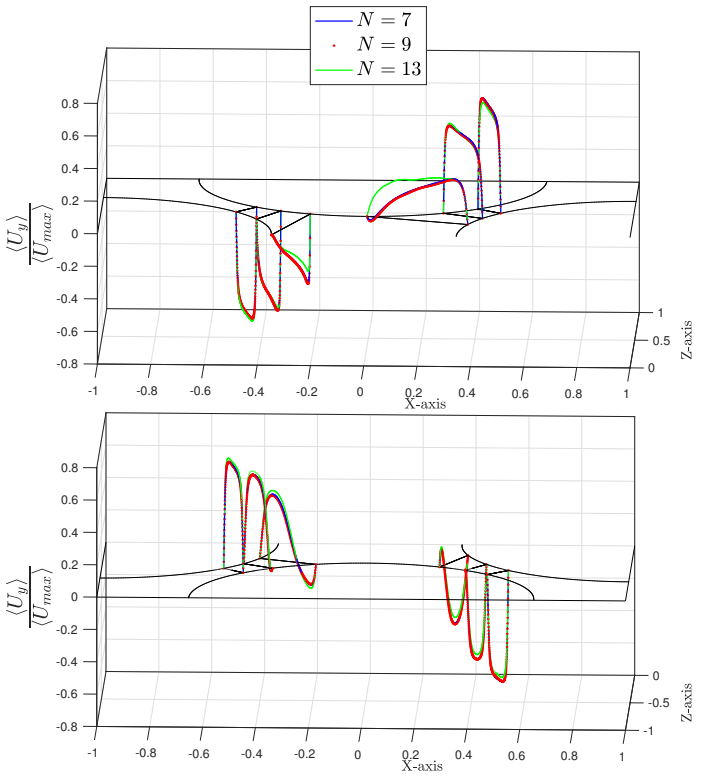

Figure 4.9: Profiles of the $\langle U_y \rangle$ for the three data sets.

covariance components show good agreement for the two lower order data sets. This is also consistent for the other components not shown here. Since the area behind the sphere, corresponding to the central pebble gap, exhibits lower magnitudes of flow due to the flow separation and recirculation effects that exist in this area, the interpolated line profiles that penetrate this area are slightly less well averaged. This is expected.

In the contracted spaces where the clearance between the pebbles are minimized, the flow is much more strongly directed or accelerated. Thus, the statistics generated in these areas shows very smooth profiles associated with sufficient averaging in time. Here, both the first- and second-orde statistics show very good agreement.

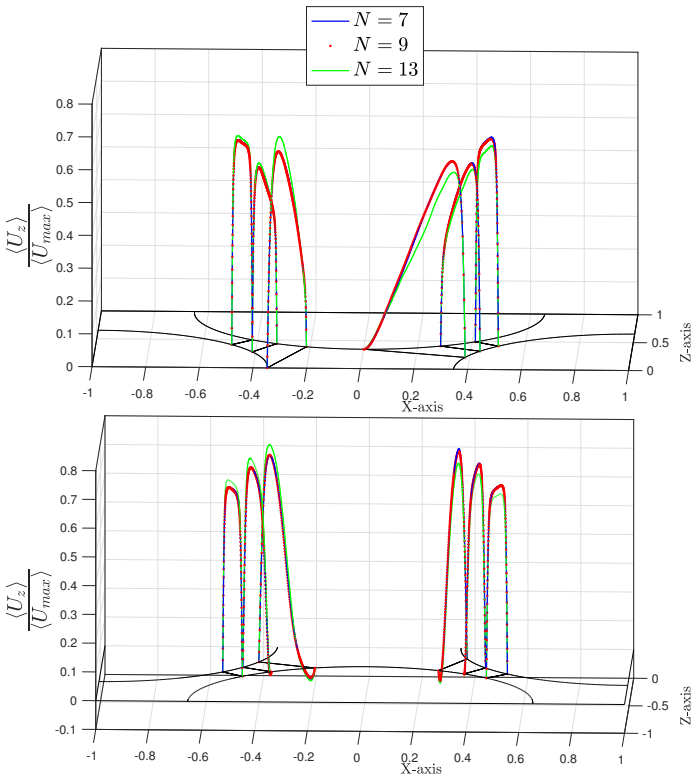

Figure 4.10: Profiles of the $\langle U_z \rangle$ for the three data sets.

The data generated using $N = 13$ exhibits acceptable qualitative agreement when compared with the other two data sets, considering the marginal stationarity achieved for that data set. While the shapes of the profiles are generally similar, the observed magnitude defects shows an observable trend, where the defect switches from negative to positive as a function of lateral position $x = 0$. This is attributable to a velocity asymmetry around the domain streamwise center line.

4.3.2 Turbulent kinetic energy

The turbulent kinetic energy transport in the FCC domain provides important information regarding the turbulent processes that take place in this class flow, where there is a large amount of geometric curvature. As seen in the results presented in

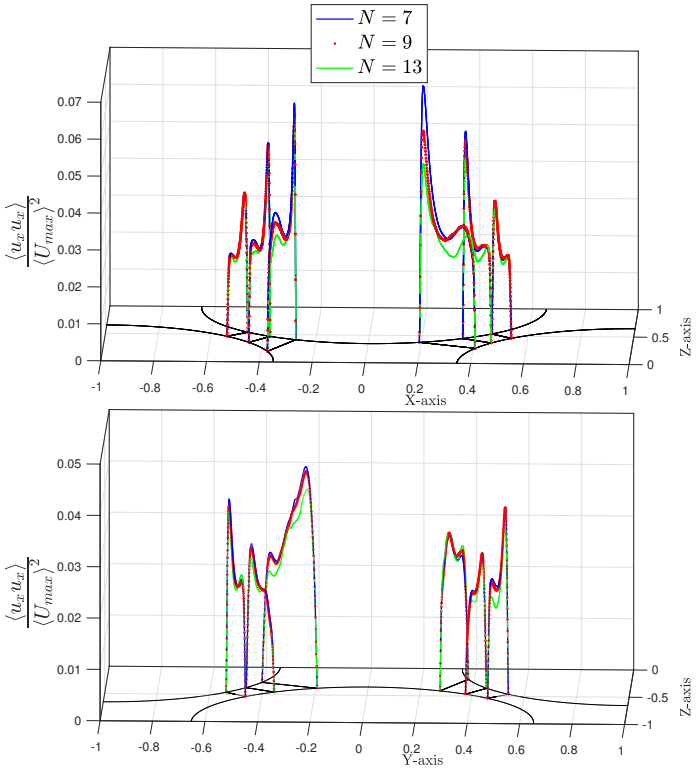

Figure 4.11: Profiles of $\langle u_x u_x \rangle$ for the three data sets.

§3, even for a single sphere in free stream conditions at low Reynolds number, the bluff body interaction between the sphere and the fluid causes complex flow behavior. This complexity is further enhanced by the addition of additional spheres. Thus, we expect the turbulent effects in the FCC domain to be even more complex.

The TKE fields presented in this subsection were all calculated using the data from the $N = 13$ case. This is due to the fact that the gradients required for the TKE term calculation require a higher resolution to be accurately resolved than what is required for the velocity and covariance data.

Since there are several terms in the TKE transport equation, plotting all the components of each term leads to an overwhelming amount of data. Since some of the

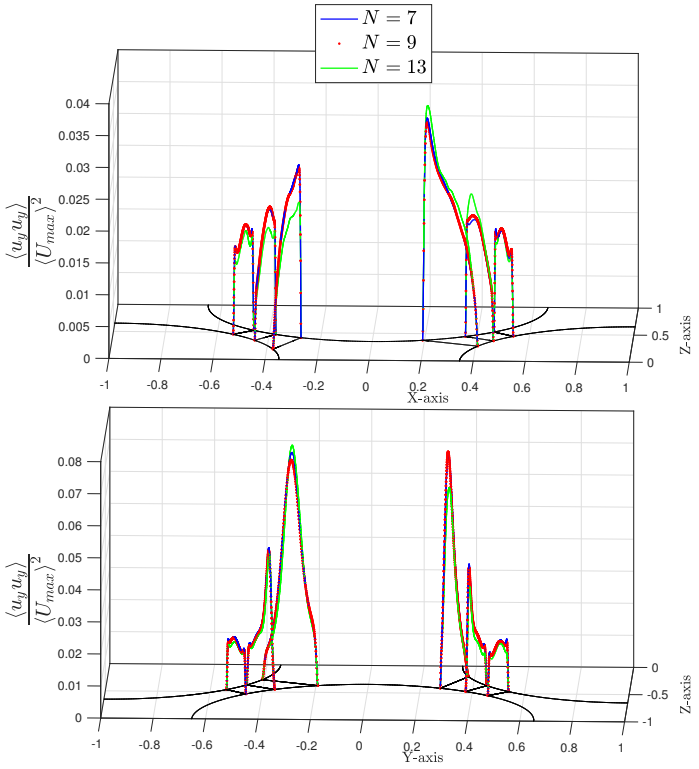

Figure 4.12: Profiles of $\langle u_y u_y \rangle$ for the three data sets.

terms are more pertinent than others, only selected components of the TKE transport equation terms are plotted here. The two terms that are generally considered to be most important are the production and dissipation terms of the TKE transport equation, since their data most directly provides information regarding the physical processes taking place in the flow.

All the second order tensors in the TKE equation have nine components, but since the tensors are symmetric, only have six independent components. It is important to realize that the structure of the individual terms show in the following figures are dependent on the coordinate frame in which they were calculated, i.e. that the data fields would look different when using a different coordinate frame. However,

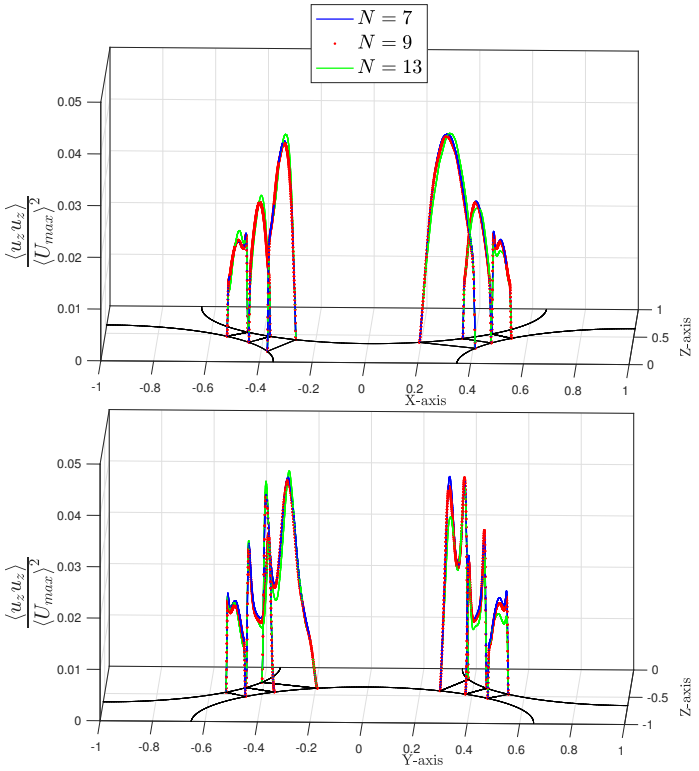

Figure 4.13: Profiles of $\langle u_z u_z \rangle$ for the three data sets.

by taking half the trace of the specific tensor under consideration, e.g. $\frac{1}{2}\mathcal{P}_{ii}$, one obtains the magnitude of that term, which is also frame invariant.

Figure 4.14 shows the independent components of the TKE production tensor, $\mathcal{P}_{ij}$. For the two diagonal terms, $\mathcal{P}_{xx}$ and $\mathcal{P}_{yy}$, it is observed that they show large magnitudes of turbulent kinetic energy production in the area behind the streamwise bottom sphere. This distribution is consistent with the area where the flow recirculation cell exists, and the enhanced TKE production in this area may be attributed to the strong shear layer and flow deceleration that exists between the fluid flowing in the positive streamwise direction and the negative velocity in the recirculation cell. For the $\mathcal{P}_{zz}$ component, the maximum magnitude of production is seen to be in front

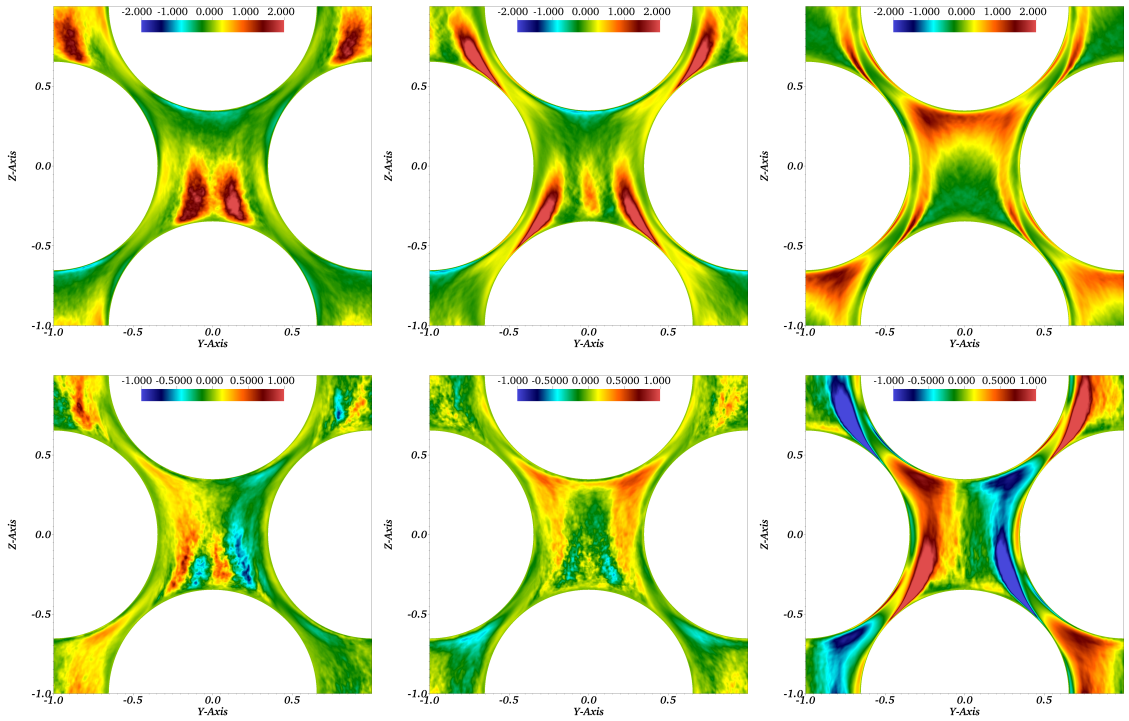

Figure 4.14: Pseudo-color fields of $\mathcal{P}_{ij}$ for the $[0, y, z]$ plane. Top row, left: $\mathcal{P}_{xx}$, middle: $\mathcal{P}_{yy}$, right: $\mathcal{P}_{zz}$. Bottom row, left: $\mathcal{P}_{xy}$, middle: $\mathcal{P}_{xz}$, right: $\mathcal{P}_{yz}$.

of the top pebble, in the area where the streamwise velocity rapidly decreases as it nears the stagnation zone on the bottom of the top sphere. As the flow is deflected laterally through the inter-pebble gaps, it is accelerated, which causes the production to decrease.

The $\mathcal{P}_{xy}$ and $\mathcal{P}_{xz}$ terms, corresponding to the transverse and out-of-plane velocity components have a lower magnitude in this plane, and are maximum behind and in front of the bottom and top spheres, respectively. The in-plane diagonal component, $\mathcal{P}_{yz}$ shows a larger magnitude, and is again maximized in the flow separation and shear layer regions that exist behind the bottom sphere.

For the components of the TKE dissipation tensor, ϵ_{ij}, a relatively similar trend

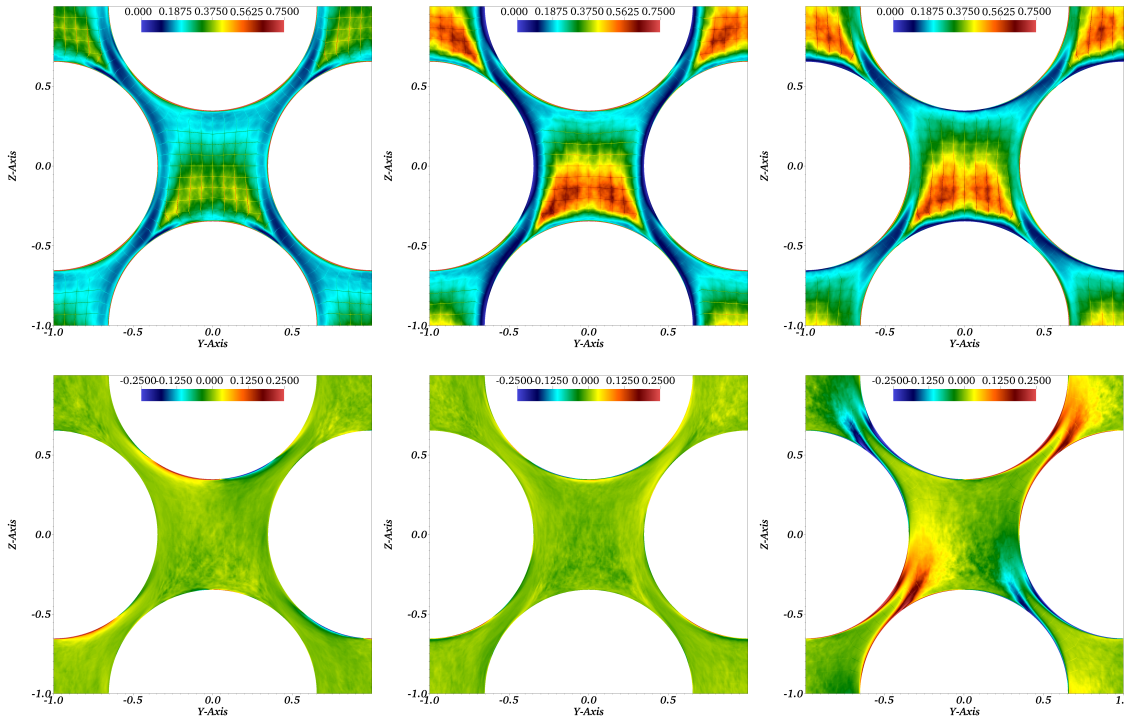

Figure 4.15: Pseudo-color fields of ϵ_{ij} for the $[0, y, z]$ plane. Top row, left: ϵ_{xx}, middle: ϵ_{yy}, right: ϵ_{zz}. Bottom row, left: ϵ_{xy}, middle: ϵ_{xz}, right: ϵ_{yz}.

is observed as for the production. For the three normal components, the distribution of the areas of maximum dissipation are similar, while in terms of magnitude the in-plane and streamwise components are larger than the out of plane component, ϵ_{xx}. In the central pebble gap area, the dissipation structure follows the separation of the flow from the surface of the bottom pebble and becomes maximized in the recirculation area in the central pebble gap.

The visible lines in the plots of the ϵ_{xx}, ϵ_{yy}, and ϵ_{zz} components are not physical flow features. These lines form at the element boundaries of the spectral element mesh. This is due to the numerical formulation of the SEM, where the velocity component values are continuous over the element boundaries, while derivatives are not.

Since the dissipation is defined as the averaged product of gradients of the fluctuating velocity, this term is very susceptible to this manifestation of the discontinuous values of the term over element boundaries. While these lines are locally unphysical, the overall structure of the field remains physical. A gradient smoothing operation does exist to remedy the discontinuity of the gradients across element boundaries, but the formulation of the dissipation term calculation used during run-time does not allow for the operation to be carried out after the averaging has already been performed. This formulation has already been updated for future studies.

The magnitude of the off-diagonal terms of the dissipation tensor is less than for the diagonal components. The values for the ϵ_{xy} and ϵ_{xz} components can also be seen to be homogeneous and roughly zero in the bulk flow areas, while being maximized on the surfaces of the pebbles. The final term ϵ_{yz}, is also maximized close to the sphere surfaces, where the streamwise velocity is reduced as the lateral velocity increases as the flow is deflected around the pebbles.

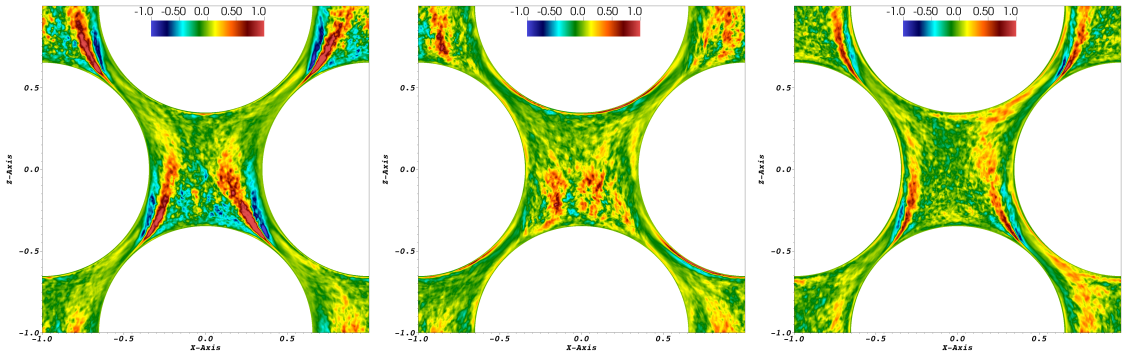

Figure 4.16: Pseudo-color fields of the diagonal components of the turbulent diffusion tensor for the $[x, 0, z]$ plane. Left: x-component, middle: y-component, right: z-component.

The turbulent diffusion tensor requires an averaged triple product of the fluctuating velocity components in it's calculation. Thus, this term takes the longest to reach statistical stationarity. It is observable in the fields of the diagonal components of this term, shown in Fig. 4.16, that the fields do not seem to be completely stationary for the available time average. However, the structure where the in plane x- and streamwise z-components are maximized is discernable, and are consistent with the flow separation shear layer. The side-by-side positive and negative valued regions are characteristic of this term of the TKE equation.

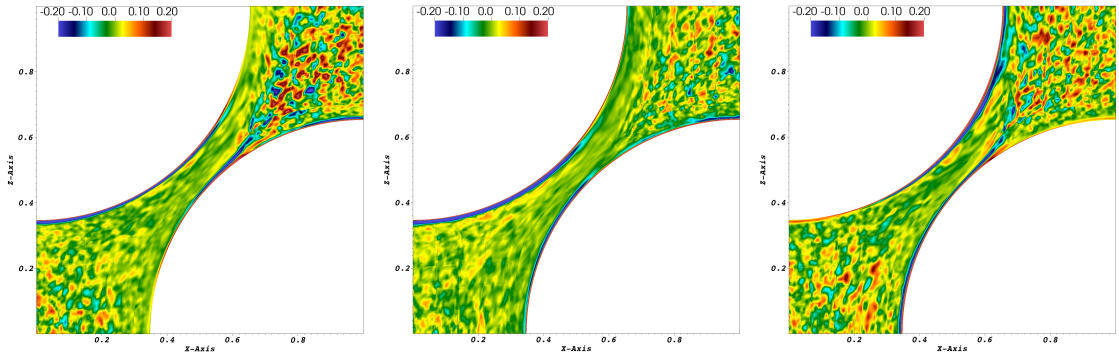

Figure 4.17: Pseudo-color fields of the diagonal components of the viscous diffusion tensor for the $[0, y, z]$ plane. Left: x-component, middle: y-component, right: z-component.

Finally, the diagonal terms of the viscous diffusion tensor are shown in Fig. 4.17. The figures focus on the contracted, inter-pebble gaps, since the viscous terms are maximized here close to the pebble surfaces. This is attributable to the viscous action dominating in the boundary layer.

4.3.3 q-DNS data cross-verification

Verification data in the form of the q-DNS data of Shams et al. [29] was available for a single lateral plane for selected flow statistics. Figures 4.18 and 4.19 show a comparison of the q-DNS data with the seventh-degree data. In order to facilitate the comparison of data generated in differing Cartesian reference frames, a 180-degree rigid frame rotation of the q-DNS data was done. Since both simulations were conducted in the limit of $Fr \to \infty$, and the rotation was of a rigid type, rotational invariance of the governing equations applies, justifying the frame rotations. Focus is given to the area of maximum statistical variability, which corresponds with the central pebble gap region.

The comparison of $\langle U_z \rangle$ for the the seventh-degree data at the CX1 interpolation with the q-DNS data is shown in Fig. 4.18a. In the figure, the profiles of the data averaged over increasing time-integration periods are presented. The values given in the legend represent a multiple of 30 FTT (i.e. $N \times 30$ FTT). As shown in the figure, the average does not converge to a constant, symmetric profile for increasing time averaging, as is expected for the class of symmetric domain under consideration here. Instead, the averaging over increasing time-integration periods produces a meta-stable switching behavior, where maximum value of $\langle U_z \rangle$ switches position laterally around $x = 0$ as as the averaging period is lengthened. The temporal instability has a very long period in the $[x, 0, z]$ lateral plane, since a significant switch in the side where the maximum magnitude is present only takes place over roughly $42 - 3 = 39 \times 30 = 1170$ FTT.

A similar trend of $\langle U_z \rangle$ is observed for the CY1 line in Fig. 4.18b. Here, the switching is more apparent than for the interpolated line in the $[x, 0, z]$ plane. We observe that for the data averaged over 15 checkpoints, an almost symmetric velocity

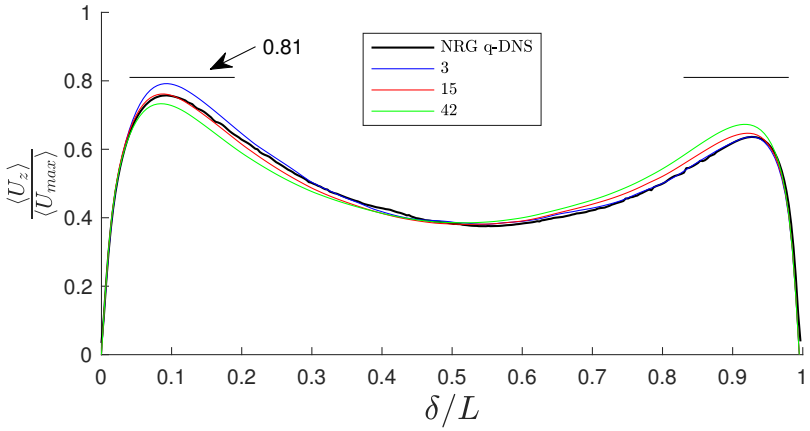

(a) Velocity component $\langle U_z \rangle$, for line CX1.

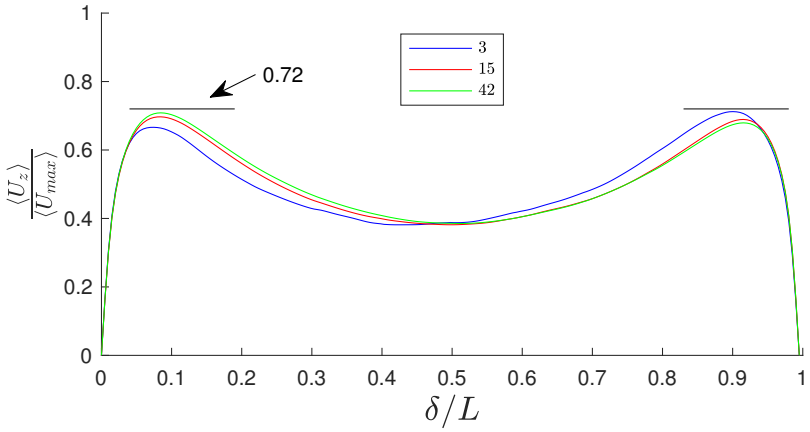

(b) Velocity component $\langle U_z \rangle$, for line CY1.

Figure 4.18: Line profiles of $\langle U_y \rangle$ plotted for different lengths of time-integration.

profile is obtained around the streamwise centerline at $\delta/L = 0.5$. For 90 FTT ($N = 3$), the maximum magnitude of this component of the velocity is located on the side of the domain where $\delta > 0$, while after 1260 FTT ($N = 42$), the maximum magnitude of the component is located at $\delta < 0$

Comparative results for the two in-plane components of the covariance tensor, $\langle u_x u_z \rangle$ and $\langle u_y u_z \rangle$, are presented in Fig. 4.19. The results show good agreement for the $[x, 0, z]$ plane illustrated in Fig. 4.19a. The magnitude of the Nek5000 data shows

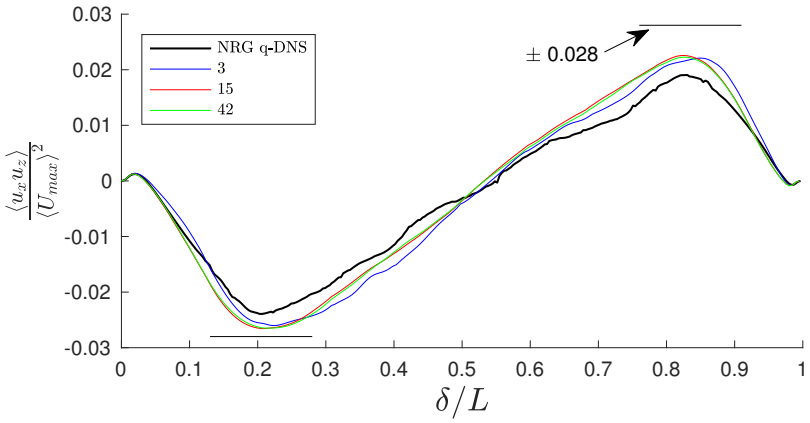

(a) Covariance component $\langle u_x u_z \rangle$, for line CX1.

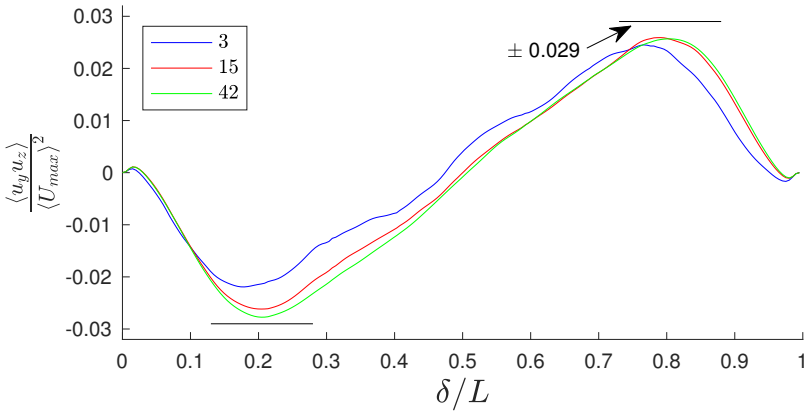

(b) Covariance component $\langle u_y u_z \rangle$, for line CY1.

Figure 4.19: Line profiles of the in-plane covariance components plotted for different lengths of time-integration.

good agreement of the profiles. Similar trends relating to the temporal velocity profile evolution are observed for the covariances in the two lateral planes. The profile for CX1 in the $[x, 0, z]$ plane is seen to converge to a relatively stationary state, whereas the covariance in the $[0, y, z]$ plane shows a clear evolution in time.

4.3.4 Temporal analysis

As an additional quantification of the averaged velocity instability observed in the data, the piecewise averaged velocity magnitudes for the streamwise top row of

time-history point probes were plotted. The averages were generated by averaging the velocity component data taken at the probe locations for consecutive 32, 64, and 128 convective time unit intervals respectively and plotting these averages as point data. Data from the seventh-degree set is illustrated here, since it had the longest time history available.

The evolutions of the piecewise averaged velocities at these points are illustrated in Fig. 4.20. It is observable that the magnitudes at the TLX and TLY probe points remain steady for most of the available time history, before switching magnitude at the end of the time series. For the TLY and TRY probes, the evolution exhibits a shorter frequency, switching twice during the available time history. Thus, spatial dynamic instabilities are observed in both lateral planes that seem to be evolving as a function of differing time scales.

4.3.5 Proper orthogonal decomposition

Temporal instabilities of flow over bluff bodies such as spheres have been identified in a number of experimental studies. Although these studies usually focus on single spheres in free stream conditions, it is expected that the physics observed in the studies is relevant to the FCC domain treated here. The studies found that for a range of Reynolds numbers, which includes the number used in this study, vortex shedding occurs in a time-varying manner such that the vortex detachment point moves around on the surface of the sphere [22]. Other experimental studies have found the existence of two unique Strouhal numbers, associated with low-frequency, large-scale instabilities in the wake and higher-frequency instabilities in the wake separation shear region, respectively [35]. Although the case presented here introduces some additional geometric complexity and associated effects, these experimental results seem to indicate that the instability we observe in our temporal data is based on

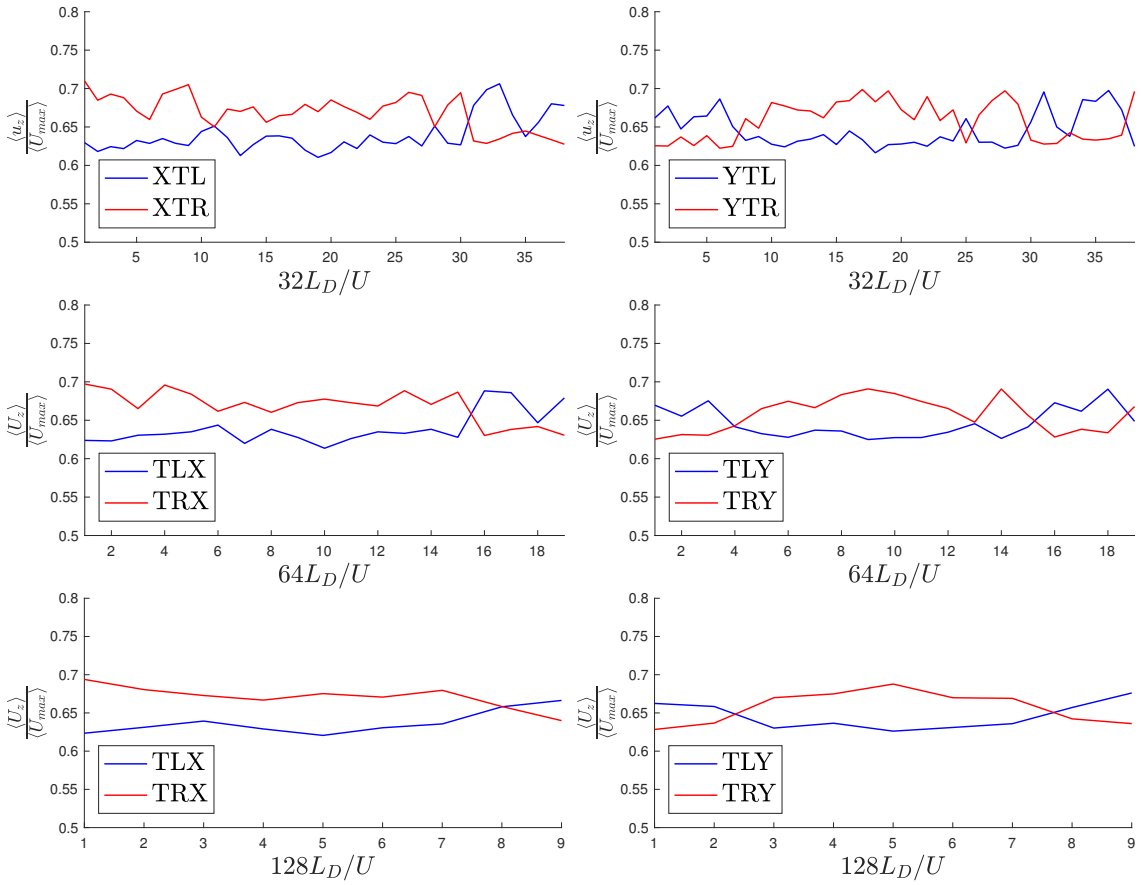

Figure 4.20: Evolution of the z-velocity (streamwise) components, averaged per 32 (top), 64 (middle), and 128 (bottom) FTT at four time probe locations.

physical effects in the wake of the pebble. Based on the conclusions made in §3, it is also evident that any instability observed for the canonical case of flow over a single sphere is greatly magnified when an additional sphere is added in close proximity to the first.

As an initial step in quantifying the observed instability, an effort is made to investigate the underlying dynamics of the flow, in a similar manner as to what was attempted in the previous section by using the method of proper orthogonal decomposition for this purpose. Details of the implementation of the method in

Nek5000 may be found §2.5.

The POD was conducted by using the seventh-degree data for two time sequences of 100,000 time steps, representing 12.5 FTT each. The time sequence initiation points were spaced so that the two time series were separated by a long time history in an attempt to observe the changes in the dynamics that lead to the observed temporal instability of the flow statistics. The first sequence was initiated by using the first available time history checkpoint as the restart condition. The second sequence was initiated using the restart field corresponding to the checkpoint generated at 900 FTT of time integration. Thus, the two time series were separated by 900 FTT of flow integration. The second checkpoint was chosen to correspond to the time at which the point probes in the $[x, 0, z]$ plane started showing a switch in the lateral side where the dominant velocity magnitude was located. Due to this switch occurring during the snapshot generation sequence for the second time series, it was expected that the POD modes would be less prominent.

Figure 4.21a shows the most energetic POD eigenfunctions for the transverse ($[x, y, 0]$) plane in POD sequence 1. A counterclockwise rotating eddy, represented by the magnitude-scaled vector field, is observed in the planar area bounded by $-0.4 < x < 0.4$, and $-0.4 < y < 0.4$. This eddy structure is three-dimensional, as can be seen by the $[x, 0, z]$ lateral plane view shown in Fig. 4.21b. In this figure, the orientation of the highest-energy eigenfunction is observed, with the modes directed in the positive lateral direction before changing to favor a downward-facing orientation. A clockwise rotating eddy structure is observed in the lower right of Fig. 4.21b, which might correspond to the area of flow recirculation known to be present behind the bottom pebble. This eigenfunction structure corresponds with the observation regarding the lateral side at which the dominant velocity is present for this sequence, as observed in Fig. 4.18a. The side of dominant velocity corresponds to

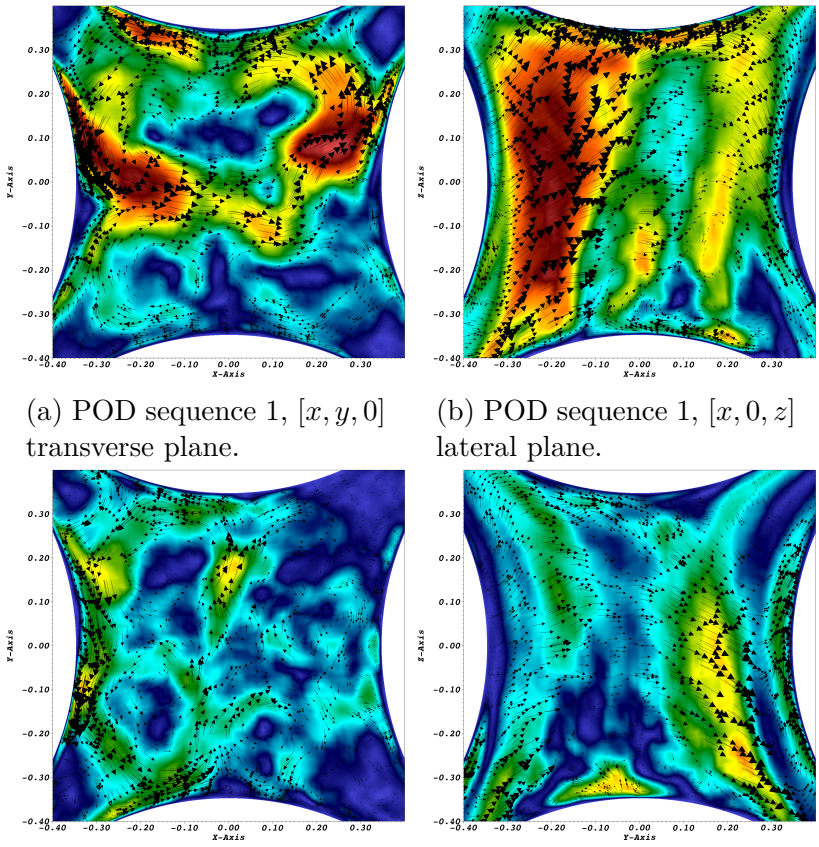

(a) POD sequence 1, $[x, y, 0]$ transverse plane.

(b) POD sequence 1, $[x, 0, z]$ lateral plane.

(c) POD sequence 2, $[x, y, 0]$ transverse plane.

(d) POD sequence 2, $[0, y, z]$ lateral plane.

Figure 4.21: Vector of the most energetic eigenfunctions in the domain for the two time sequences.

the lateral side $-0.4 < x < 0$, where the eigenfunctions are nominally directed in the flow direction, whereas the lower magnitude side corresponds to $0 < x < 0.4$, where the eigenfunctions are directed downwards because of the recirculation eddy. Thus, this large-scale, three-dimensional rotational structure of the fluctuating velocity eigenfunctions is potentially the reason for the observed asymmetry in the mean velocity field.

Sequence 2 of the POD delivers similar structure fields, as observed for the trans-

verse and lateral planes in Figs. 4.21c and 4.21d. The most relevant difference is that the eddy structure observed in the lateral plane has undergone a 90-degree, counterclockwise rotation in the transverse plane. Thus, a structure similar to what was observed in the $[x, 0, z]$ lateral plane in sequence 1, is now seen in the $[0, y, z]$ plane in sequence 2.

The magnitude of the modes observed in sequence 2 is lower than those seen in sequence 1, as expected. Since the temporal start point for the second time sequence used for the POD was chosen to correspond to the time the switching commenced, the averaged behavior for the sequence might be changing rapidly relative to the locally stationary behavior captured in sequence 1, thus leading to less well established structures. The correlation between the orientation of the highest energy eigenfunctions and the position of maximum velocity magnitude is consistent with the observation for sequence 1.

4.3.6 Expanded case and ensemble averaging

Based on the observation of the metastable behavior of the time-averaged turbulence statistics in the case, it was important to test whether the geometry played any significant role. Thus, to confirm sufficient decorrelation between the periodic boundaries in the streamwise direction, an expanded FCC domain consisting of three unit cells was generated by translating and copying the original unit cell twice in the streamwise direction to create a three FCC geometry. Periodic boundary conditions were used along all domain edges. When time averaging was performed for this new geometry, similar metastable behavior was observed as in the single FCC case. It was therefore confirmed that the observed switching behavior was not simply a consequence of the domain potentially being too small. The effect of multiple spheres in close proximity in cases with non-periodic boundaries was also confirmed in §3.

A second test that was proposed was to test the effect of the averaging approach used to generate the turbulence statistics. Instead of using time-averaging, a newly implemented ensemble averaging scheme [36] was used to generate ensemble averaged data for the three FCC domain. By generating data using the ensemble averaging routines, it could be determined whether the method of averaging impacted the attainment of a symmetric, time-invariant solution that is expected for this class of flow simulation. For the ensemble averaging runs, 32 concurrent sessions of the case were run in parallel. Each session was initialized using a uniquely perturbed initial flow field based of the session number. After allowing sufficient time integration for the sessions to decorrelate, time averages of each session were taken, after which the ensemble average was performed over all the sessions.

Figure 4.22 shows $\langle U_{mag} \rangle$ in the $[x, 0, z]$ lateral plane of the expanded domain after 192 FTT of ensemble averaging. A qualitatively symmetric velocity field around the streamwise centerline of the domain can be observed. The covariance field for $\langle u_x u_z \rangle$ is shown for the same plane in Fig. 4.23

Three line interpolation locations, CX1-3, are highlighted in Figs. 4.22 and 4.23. Interpolations of $\langle U_z \rangle$ and $\langle u_x u_z \rangle$ at these locations plotted in Figs. 4.24a and 4.24b respectively.

A comparison between the ensemble averaged data, the temporally averaged Nek5000 data, and the q-DNS data, reveals a clear difference regarding the symmetry of the first- and second-order turbulence statistics. This indicates a violation of the ergodicity assumption that is used to establish an equivalence between time averaged and ensemble averaged data. This observation has also been made for other cases where high-fidelity methods were employed [37]. Thus, in order ensure completely stationary statistics for this type of flow geometry, ensemble averaging instead of temporal averaging may be a requirement.

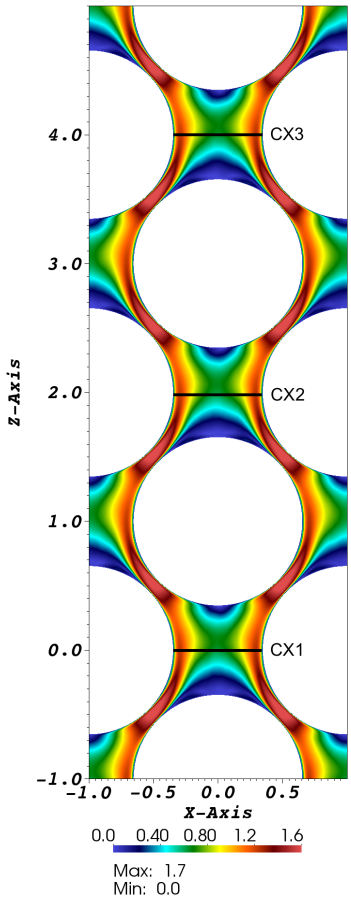

Figure 4.22: Field rendering of $\langle U_{mag} \rangle$ in the $[x, 0, z]$ plane for the 3 FCC domain.

4.4 Conclusions

This section presented a DNS analysis of flow through an extended FCC domain. Three databases were generated by using differing levels of spatial discretization. The conformance of each database to DNS requirements based on the Kolmogorov length and time scales was tested, with even the data generated using the lowest order of spatial discretization exceeding the requirements. To ensure that Kolmogorov theory could be used as a test for DNS conformance at this moderate Reynolds number, the data from the databases was compared with each other to test for consistent results.

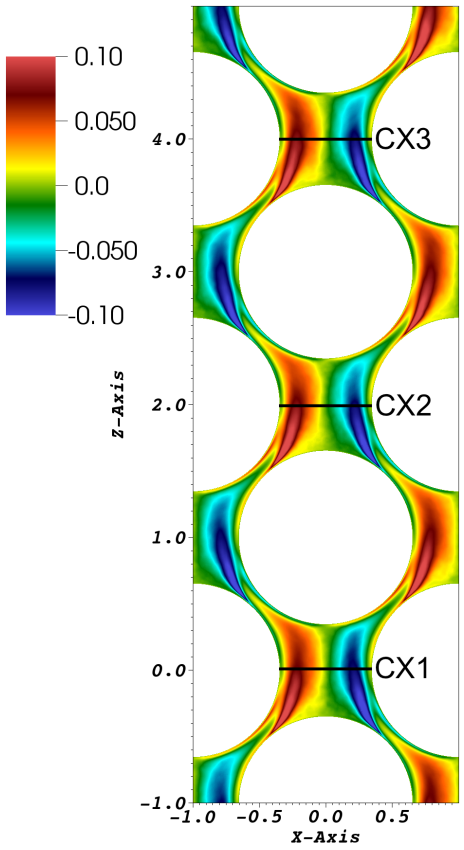

Figure 4.23: Field rendering of $\langle u_x u_z \rangle$ in the $[x, 0, z]$ plane for the 3 FCC domain.

This form of testing is analogous to a grid convergence study, but since all the data sets were already resolved beyond the Kolmogorov scale, it was expected that they would deliver consistent results. This expectation was proven to be correct, with the exception that the data generated using the highest order of spatial discretization was not completely stationary yet. It was thus proved that the Kolmogorov scales may be used as an explicit test of DNS conformance for this type of flow simulation.

Quasi-DNS data was used to perform cross-verification of the generated DNS data. Good agreement was observed between the Nek5000 data and the available first- and second-order statistics data from the q-DNS database. During the cross-

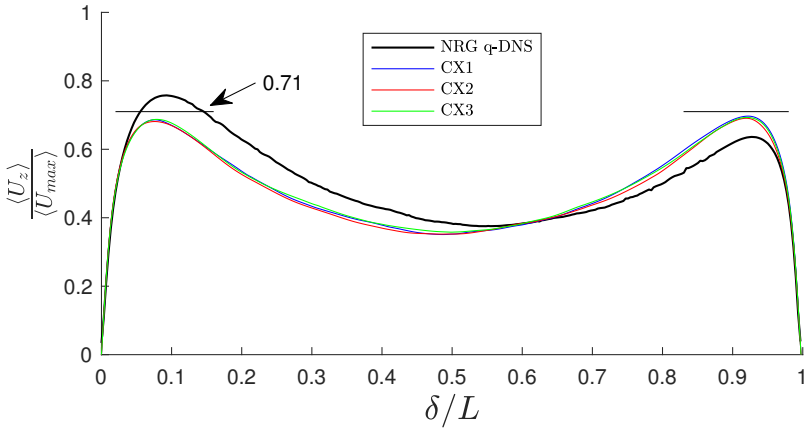

(a) Velocity component $\langle U_z \rangle$.

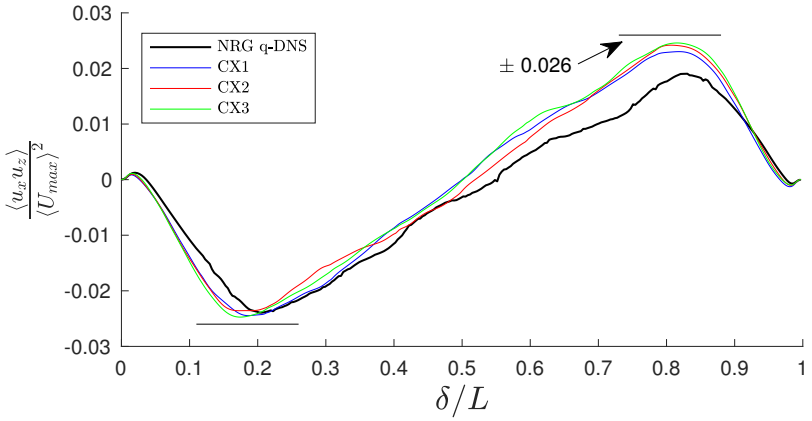

(b) Covariance component $\langle u_x u_z \rangle$.

Figure 4.24: Interpolated line profiles of ensemble averaged data in the 3 FCC domain.

verification process, a temporal instability in the averaged data was observed. This metastable behavior manifested in the form of a bounded, semi-periodic switching of the position of the maximum magnitude of averaged statistical quantities in the domain. This behavior was initially believed to be due to an insufficient amount of time averaging of the data, but the switching continued even for very long periods of time integration. Thus, the frequency of this mechanism is very low, being on the order of hundreds of flow through times.

POD was implemented as an analysis tool that could possibly shed light on the metastable behavior observed in the flow. The data generated in the POD allowed for the identification of a correlation between the most energetic POD modes at different points in time and the observed temporal instability. It was concluded that the flow recirculation cell behind the streamwise bottom pebble generated a large, three-dimensional instability that changed shape over large amounts of time integration, and that this structure resulted in the time-dependent lateral shift of the position of the maximum values of the statistical quantities under consideration.

Finally, a three FCC flow domain was generated by translating and copying the original flow domain. A newly implemented ensemble averaging method was employed to generate stationary and symmetric flow statistics in this geometry. The ability of the ensemble averaging method to generate the expected symmetric results point to a violation of the ergodicity assumption in this class of flows. This violation is the result of low-frequency instability modes in the flow, potentially caused by the slowly changing structure of the recirculation cell behind the pebbles.

5. NUMERICAL EXPERIMENT III: WALL BOUNDED DOMAIN

The final section pertaining to the numerical experiments corresponds to the last study done during the dissertation research. It was identified that no literature existed, to the best knowledge of the author, that treated wall bounded pebble bed domains. It was hypothesized that a bounding wall would significantly influence the behavior of the flow in the near wall region, and therefore warranted investigation. The insights gained from the two prior studies, coupled with practical considerations regarding the size of the problem and it's associated computational burden, informed the development of this study.

The study is again detailed using the background, methodology, results and discussions and conclusions format of the previous sections.

5.1 Background

The bulk of the literature pertaining to the investigation of turbulent flows through pebble beds focus on flow through regions removed from wall boundaries, i.e. the reactor vessel walls. Example works like the series of papers by Shams et al. [1, 6, 38, 30, 29], the LES paper of Hassan [7], and a number of theses [12, 39, 40].

This focus extends to more fundamental cases, where only single examples of the treatment of spherical bluff bodies near bounding walls are encountered in literature. Examples of experimental works include [41], while computational works include treatment of single spheres [42] hemispheres [33]. From these works, it is apparent that bounding walls drastically alter the flow characteristics when compared with flows far removed from walls.

The experimental work in [41] is particularly pertinent in showing the effect of a sphere in contact with a flat plate boundary, which leads to the formation of a

low velocity recirculation region behind the sphere. In a practical reactor system, where convective heat transfer is critical, such stagnation of the flow may lead to significant temperature gradients on both the pebble surfaces and bounding walls. Such temperature gradients may cause thermal fatigue in the spheres and core walls, leading to decreased safety margins during long term operation.

The development of DNS flow data for a pebble bed flow domain with the addition of a bounding wall again presents an opportunity to develop a better understanding of the fluid mechanical interplay between spherical bluff bodies and walls walls, while also providing reference data which be used to verify lower fidelity RANS based simulations.

This study presents results for a DNS of a wall bounded pebble bed domain based on an extension of the FCC unit cell geometry discussed in §4.

5.2 Methodology

This section discusses the methodology employed during the study. A case outline is given, including meshing, flow and boundary condition information. The interpolation of data during the simulation is discussed. Finally, the computational aspects of the simulation is briefly discussed.

5.2.1 Case outline

The geometry for the case is based on the FCC unit cell geometry treated in the previous section. To generate the mesh, the FCC mesh was copied in each principle coordinate direction so that an eight FCC unit cell geometry was obtained. After this, a half FCC unit cell layer was added to a selected domain edge to complete the layer of spheres next to the wall. Finally, another layer of elements were added to create a clearance gap between the sphere layer and the wall boundary equal to the fixed inter-pebble gap spacing of the FCC unit cell. Thus, a consistent spacing

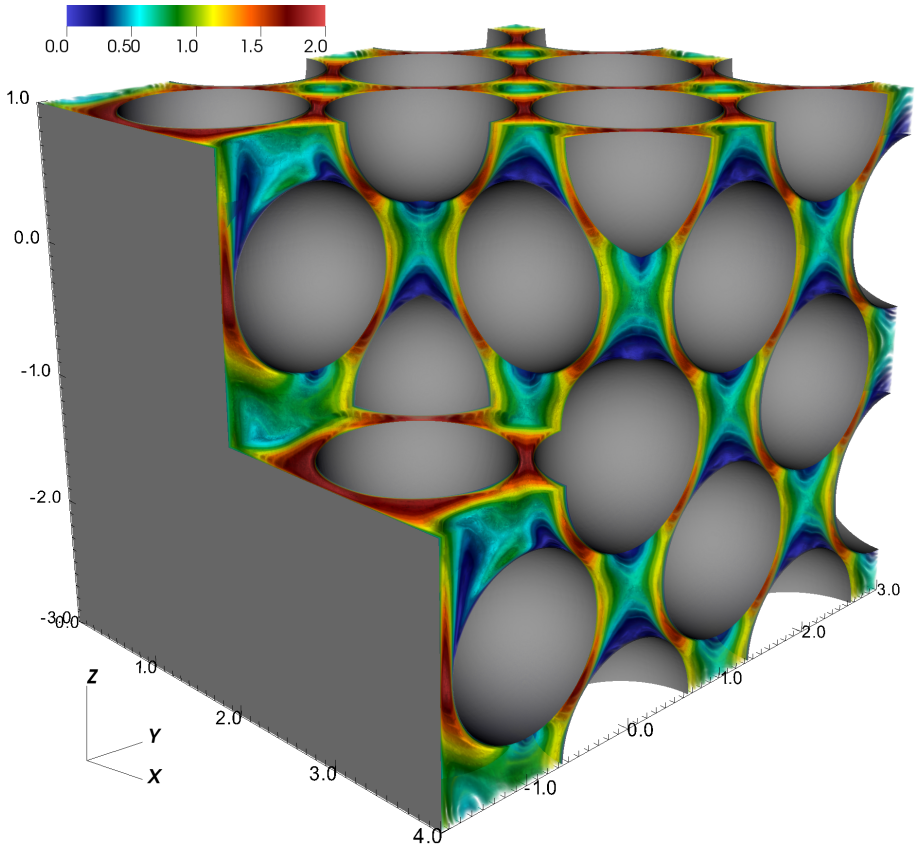

Figure 5.1: Sectioned volume rendering of the wall bounded domain showing the averaged velocity magnitude.

between all wall surfaces in the domain was maintained. Figure 5.1 shows the geometry of the complete domain, with a volume rendering of the averaged velocity magnitude obtained after 256 convective time units of integration. A cutaway section corresponding to $x \geq 2$, $y \leq 0$, $z \geq -1$ is included to show the velocity profiles inside the domain in the near wall region.

The spacing between the wall and the spheres was chosen to minimize the number of additional elements required for the mesh, while still allowing for adequate resolution of the turbulent boundary layer at the wall boundary. Meshing contact areas remains a challenge when using hexahedral meshes, as discussed in the previous

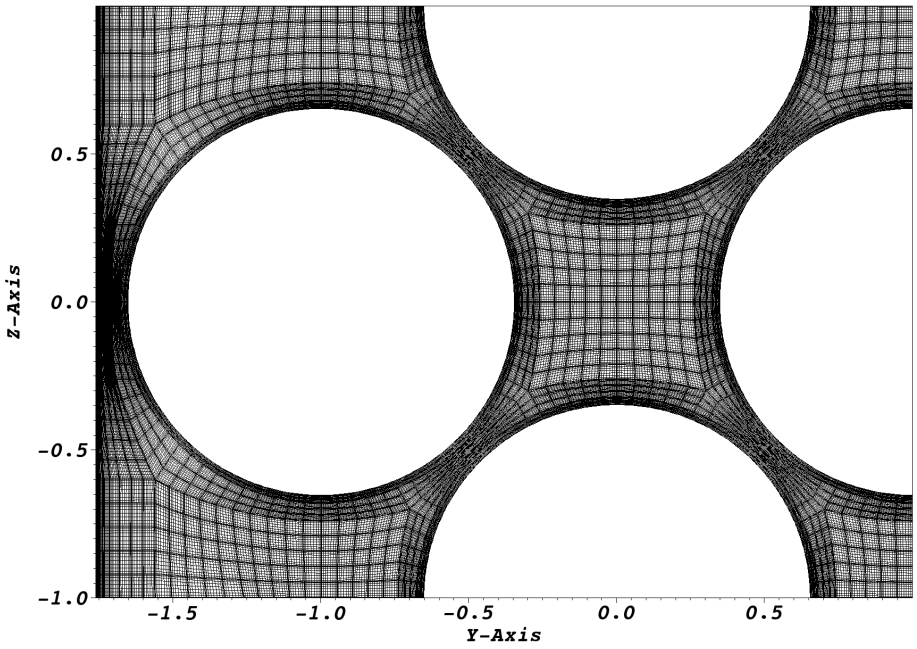

Figure 5.2: Section of the hexahedral mesh for the wall bounded domain in the near wall region.

section. Thus, at the present time, a non-zero spacing is required to generate a mesh of acceptable quality. A section of the mesh in the $[2, y, z]$ plane in the near wall region is shown in Fig. 5.2.

The boundary conditions for the case include non-slip wall conditions for the sphere surfaces and the bounding wall at the negative y-coordinate domain edge, a symmetry (slip) condition at the positive y-coordinate domain boundary, and periodic boundary conditions for both x-coordinate domain edges and the stream wise (z-coordinate) edges.

The flow Reynolds number was based on the same parameters as those used in the results in §4, namely the averaged domain inlet velocity and the diameter of the spheres, and an appropriate kinematic viscosity. To ensure that comparisons could be drawn between the results presented in §4 and the results presented in this

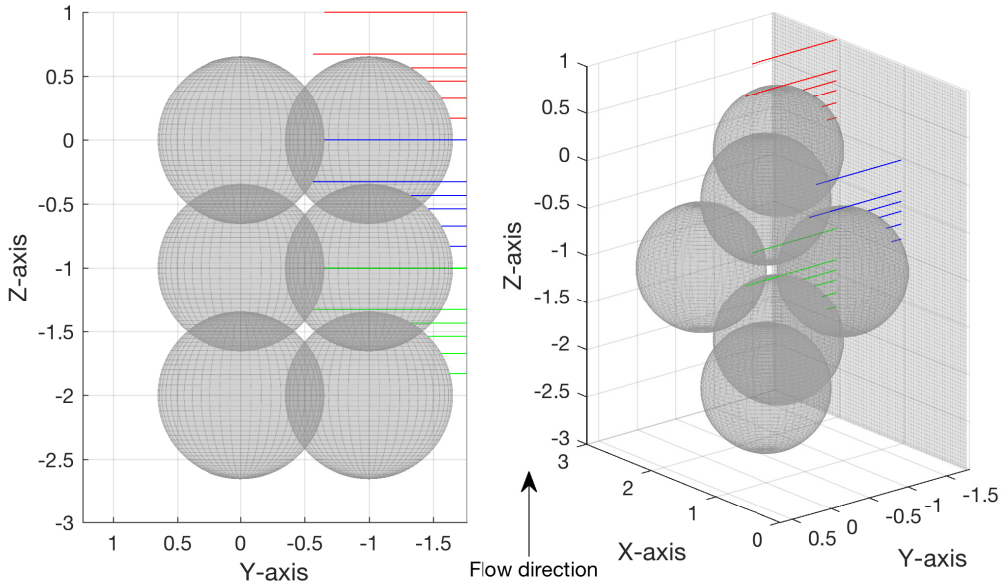

Figure 5.3: Three-dimensional view of three of the interpolation line sets distributed in the near wall region.

section, a value of $Re = 9308$ was used.

5.2.2 Data interpolation

To collect time series data during the simulation, 44 line profiles consisting of 100 point probes each were defined in the computational domain. During run time, the velocity and pressure information was interpolated at these locations for each time step to generate time series that could be used do time-series analyses such as temporal and spatial spectra, temporal auto-correlations, and two-point correlations.

The interpolation lines were chosen to be normal to the wall, with each terminat-

ing at the wall and the relevant sphere surface depending on the location of the line in the domain. Figure 5.3 shows a subset of three sets of six interpolation lines from the total set of 44 lines. Each set is consistently spaced, with a simple translation of the coordinates generating the interpolation lines sets at different locations in the domain.

The spacing of the lines that terminate on the surfaces of the the first row of spheres next to the wall were chosen to have elevations of $\psi = 15, 30, 45, 60$ degrees. The elevation is defined as $\psi = 90° - \phi$, where ϕ is the inclination angle from the zenith, which is defined to be the positive z-coordinate. The layout of each interpolation line set is presented in Fig. 5.4. The line colors and symbols will be used in subsequent line plots to demarcate the location at which the relevant profiles were extracted.

The spacing of the lines that terminate on the surfaces of the the second row of spheres from the wall were defined to be translated to be at $z = z_{ref} + 0.75$ and $z = z_{ref} + 1$ respectively, where z_{ref} is the center point z-coordinate of the sphere directly below the line in the z-direction. The interpolation line x- and y-coordinates are also defined to be the x_{ref} and y_{ref} respectively, where the reference coordinates are again defined as the relevant sphere center point coordinates.

5.2.3 Computational parameters

The wall bounded domain consisted of 386,400 spectral elements. Based on scoping runs and experience from the simulation of the FCC unit cell case, a polynomial order $N = 10$ was chosen for the spatial sub-discretization. This resulted in a domain consisting of roughly 280 million collocation points.

Time stepping was done using the characteristics scheme, allowing for stable time integration with a CFL number of 2. This choice of time step length was larger than

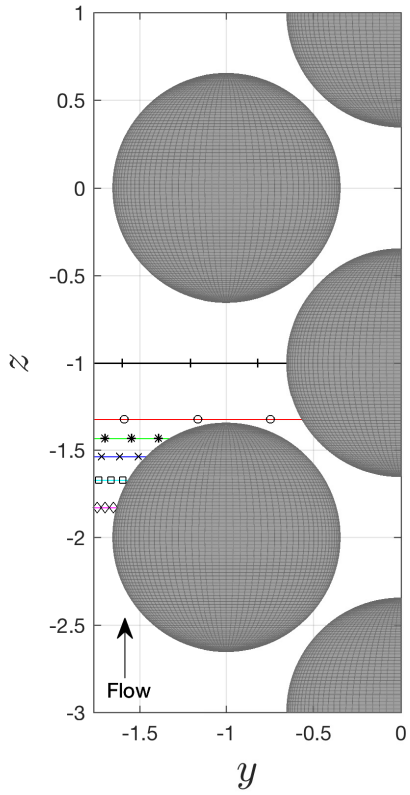

Figure 5.4: Layout of one of the interpolation line sets normal to the wall.

the minimum Kolmogorov time scale for the flow in this case. Fig. 5.5 shows a power spectrum of the stream wise component of the fluctuating velocity, u_z, at a point located in the gap area between two spheres in the sphere layer next to the wall. It is observed that the energy content for the high frequency fluctuations becomes negligible at the $St = 500$, thus illustrating that all energy containing scales are still captured, thus conforming to DNS requirements.

To reduce the real time to a stationary state for the turbulence statistics, the ensemble averaging routines discussed in §4.3.6 was employed to conduct production runs and averaging. After initial development of the flow for 60 convective time units

Table 5.1: Computational parameters: Wall bounded domain case

Parameter	Value
Time step length (L_D/U)	0.0005
Collocation points	279.08E6
Ranks/Session	16,384
Sessions	16
Total FTT	256
Core hours	8.4E6
Hours/FTT	32,813

using polynomial order $N = 6$, an ensemble run was initiated using 16 concurrent sessions, with each session running for a total of 5 convective time units. The first time unit in each session was used for decorrelating the uniquely perturbed fields, after which statistics were gathered for the remaining four convective units. This procedure was repeated four times, with lower polynomial runs used to generate 24 convective units of flow between each ensemble run. This ensured that the initial condition for each ensemble run was unique. Using this methodology, 256 convective units of total averaging was achieved.

5.3 Results and discussions

The following subsections discuss selected first- and second-order turbulence statistics. The presented pseudo-color fields are slices of the the domain in $[1, y, z]$. The interpolated line profiles correspond to the blue set of profiles shown in Fig. 5.3. These selections were arbitrarily made, since the periodicity of the domain dictates that similar results will be observed for a given translation of in the lateral directions.

The interpolated data is normalized in the same manner as discussed in eq. (3.3) of §3.3.1, while the normalized line zero coordinate corresponds to the location of

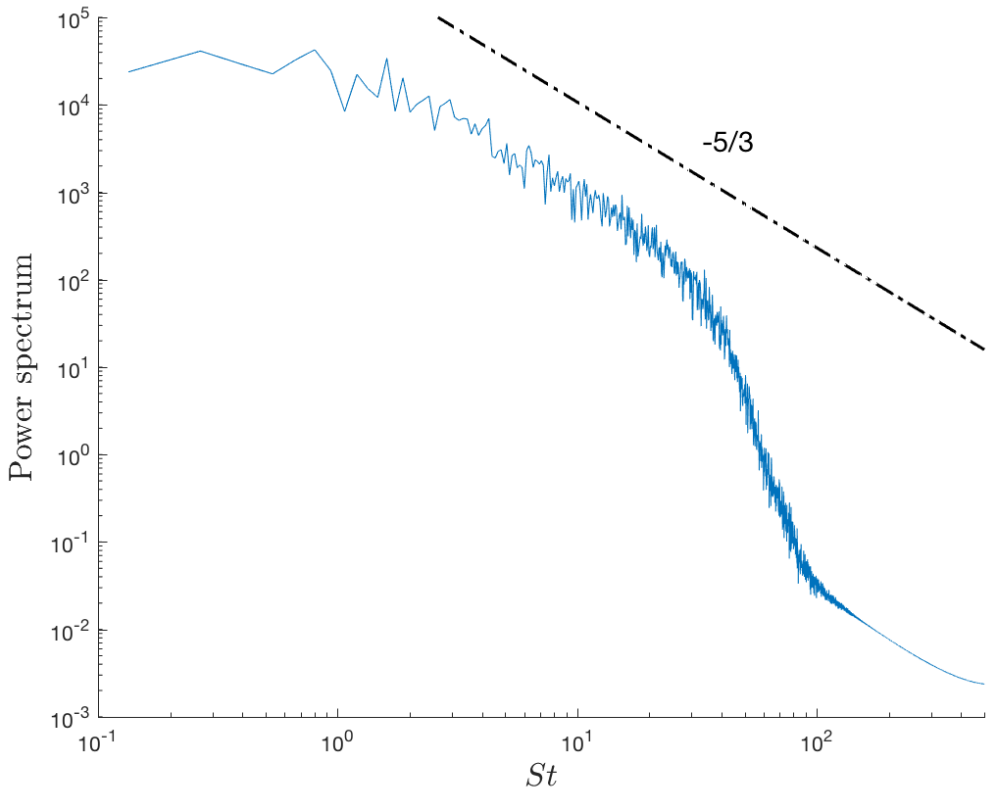

Figure 5.5: Power spectrum for u_z at the point $[1, -1, 0]$.

the wall boundary.

5.3.1 First-order statistics

Data is only presented for $\langle U_y \rangle$ and $\langle U_z \rangle$, since the magnitude of $\langle U_x \rangle$ is significantly smaller than the other components. This is expected for the plane under consideration. For the field of $\langle U_y \rangle$ shown in Fig. 5.6, a similar field is observed as for the single FCC case discussed in §4 in the area beyond the first row of pebbles, with the flow accelerating laterally around the spheres in the contracted inter-pebble spaces. Near the wall, the flow is directed towards the wall more consistently, indicating an entrainment effect caused by the accelerating fluid near the wall.

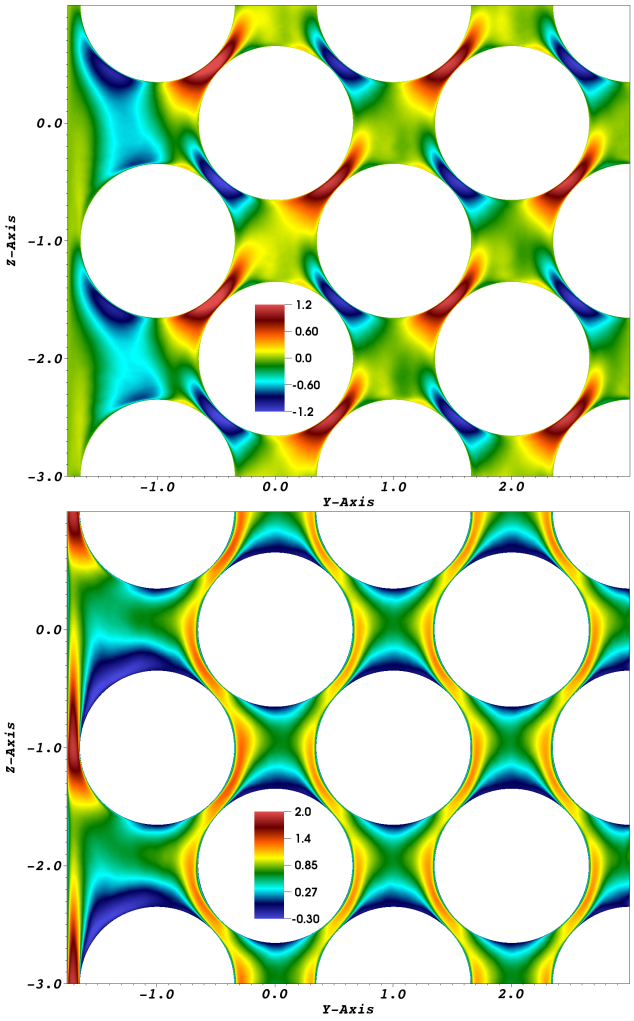

Figure 5.6: Pseudo-color field of $\langle U_y \rangle$ (top), and $\langle U_z \rangle$ (bottom).

For $\langle U_z \rangle$, shown in Fig. 5.6, the field again resembles the flow distribution seen in the 1FCC case in the domain beyond the first row of spheres next to the wall. There is a slight increase in the magnitude of $\langle U_z \rangle$ on the side of the first row of spheres furthest on the wall. The highest stream wise velocity is observed in the area surrounding the minimum spacing between the sphere and the wall boundary. Because of this accelerated flow, the recirculation cell behind the spheres in the first row of pebbles next to the wall is drawn towards the wall and also enlarged when

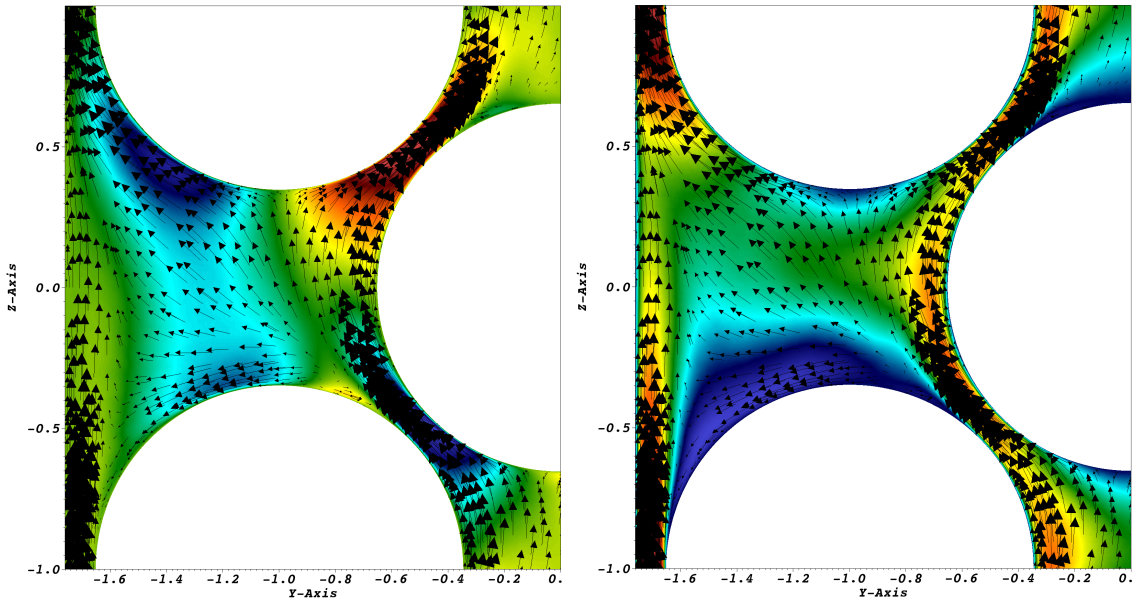

Figure 5.7: Pseudo-color field and velocity magnitude vectors for $\langle U_y \rangle$ (left), and $\langle U_z \rangle$ (right) highlighting the recirculation behind the pebbles in the near wall region.

compared with the recirculation cells behind the pebbles further removed from the walls. This is due to the flow entrainment caused by the accelerating flow through the pebble-wall gap. This is highlighted in Fig. 5.7.

The interpolated line profiles for $\langle U_y \rangle$ in Fig. 5.8 shows the negative lateral velocity, indicating flow towards the wall, in the recirculation cell region. The magnitude of lateral flow is reduced in the large gaps between the spheres next to the wall. For the $\langle U_z \rangle$ component of the velocity, both flow acceleration next to the wall, as well as the negative streamwise velocity in the recirculation cell are observable.

5.3.2 Second-order statistics

The second-order statistics highlight the increased Reynolds stress intensity in the near wall region. For the lateral component $\langle u_x u_x \rangle$, shown in Fig. 5.9, a marked increase is observed in the gap areas of the first row of spheres next to the wall.

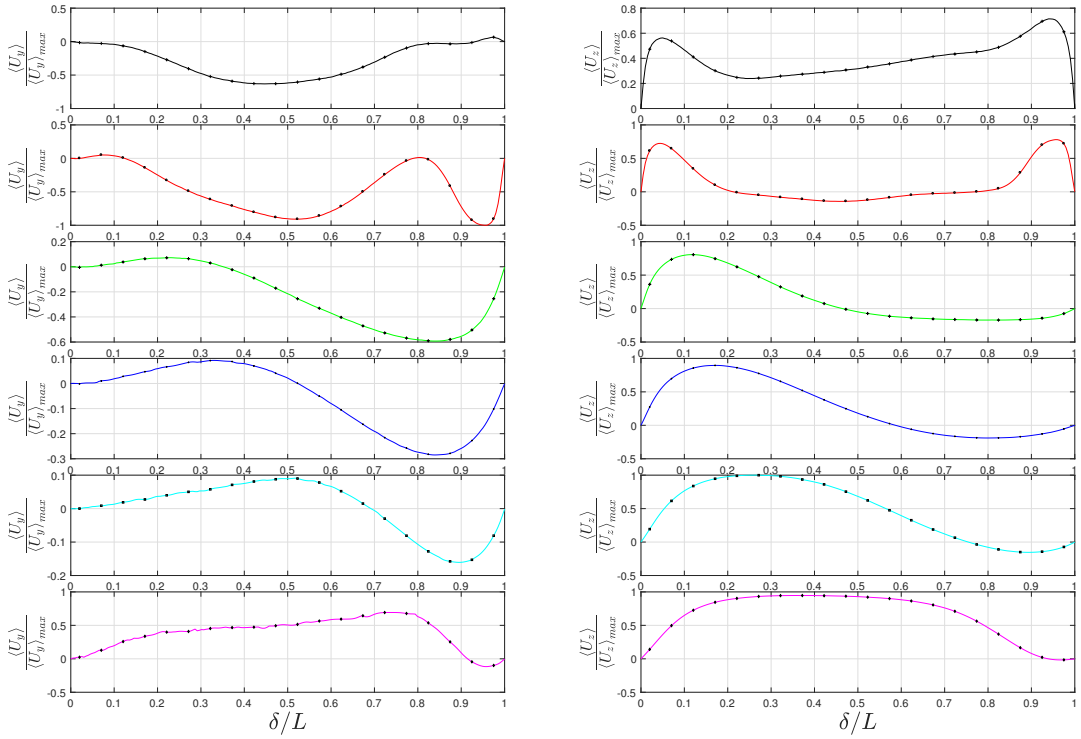

Figure 5.8: Normalized interpolated line profiles for $\langle U_y \rangle$ (left), and $\langle U_z \rangle$ (right).

An increase in the magnitude of the stress is also observed close to the surface in front of the spheres relative to the flow direction. This is related to the acceleration of the fluid through the gap between the spheres and the wall, and the subsequent deceleration as the flow is curved away from the wall after passing through the gap and encounters the next sphere.

A similar trend is observed for $\langle u_y u_y \rangle$ in Fig. 5.9, where there is an increase in magnitude in nearly the entire gap area between the spheres adjacent to the wall. The shear stress magnitude of this component is also asymmetric behind the second row of pebbles with relation to the wall, with an increased shearing effect taking

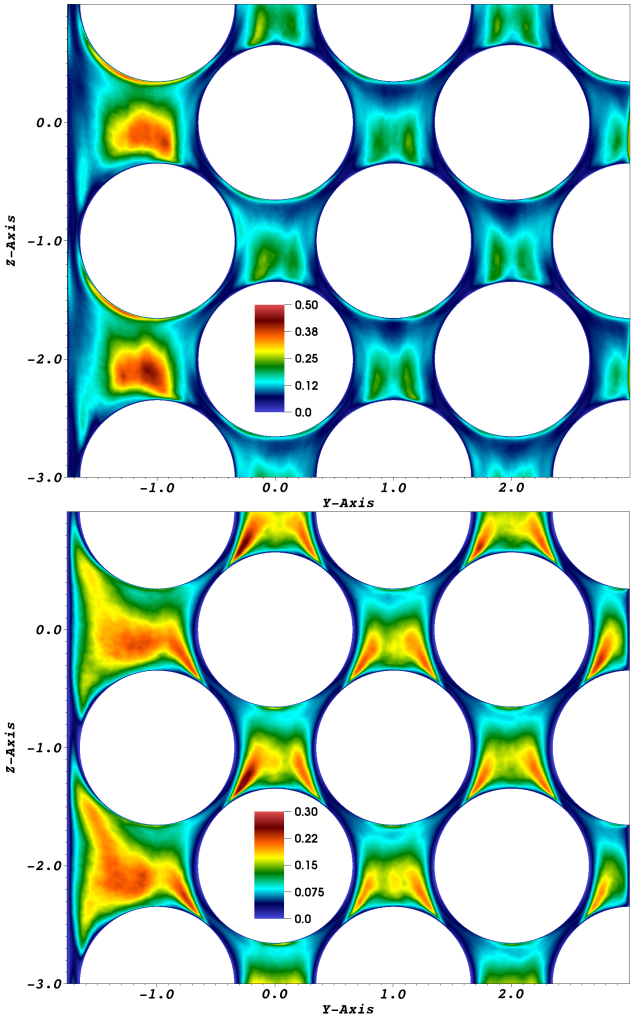

Figure 5.9: Pseudo-color field for $\langle u_x u_x \rangle$ (top), and $\langle u_y u_y \rangle$ (bottom).

place on the side closest to the wall.

The highest magnitude of $\langle u_x u_x \rangle$ occurs in the large gap between the pebbles next to the wall, as is observable in the top (black line) line plot of this Reynolds stress component in Fig. 5.10. The magnitude of the component decreases as the interpolation lines trend towards the area of maximum streamwise velocity in the minimum pebble-wall spacing. The same trend is observable for $\langle u_y u_y \rangle$ in the same figure.

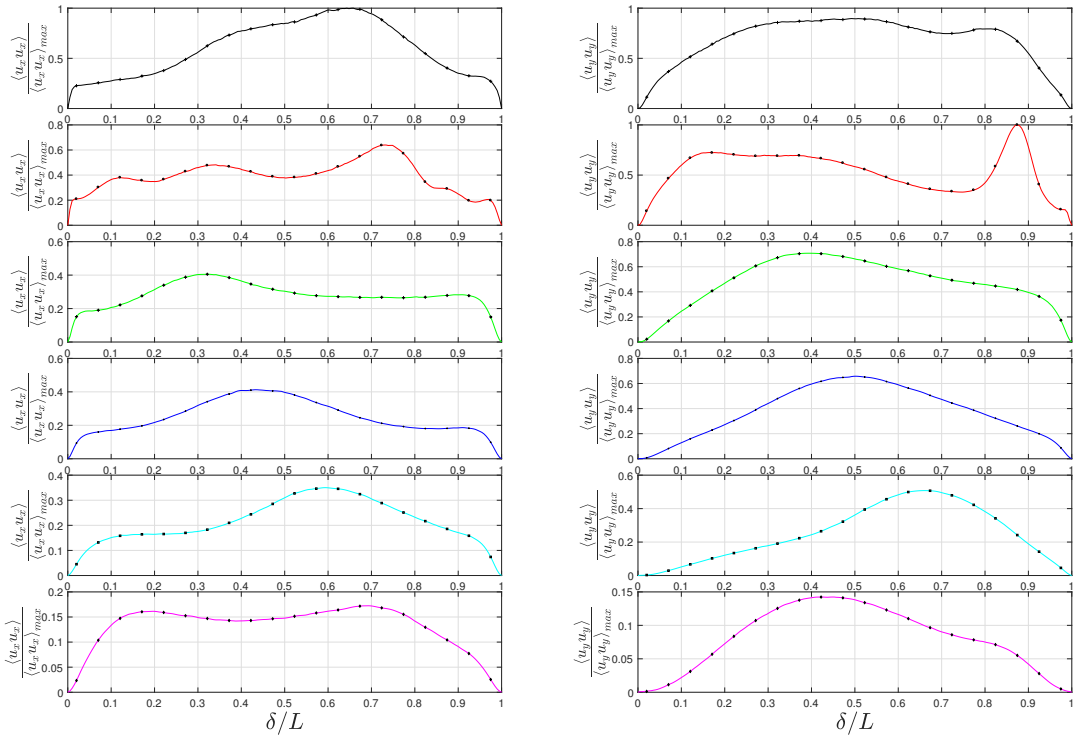

Figure 5.10: Normalized interpolated line profiles for $\langle u_x u_x \rangle$ (left), and $\langle u_y u_y \rangle$ (right).

The stream wise shear stress, $\langle u_z u_z \rangle$, shows the largest increase in magnitude near the wall in Fig. 5.11. This increase is also intuitively the easiest to understand when considering the stream wise velocity component shown in Fig. 5.6. Due to the strong velocity gradient that exists between the high-velocity jet and the recirculation cell behind the sphere, a steep velocity gradient exists, leading to increased shear stress in this area.

The off-diagonal Reynolds stresses are smaller in magnitude than the diagonal components of the Reynolds stress. Since they are of smaller magnitude, the time integration period required for these quantities to reach stationarity is longer. The

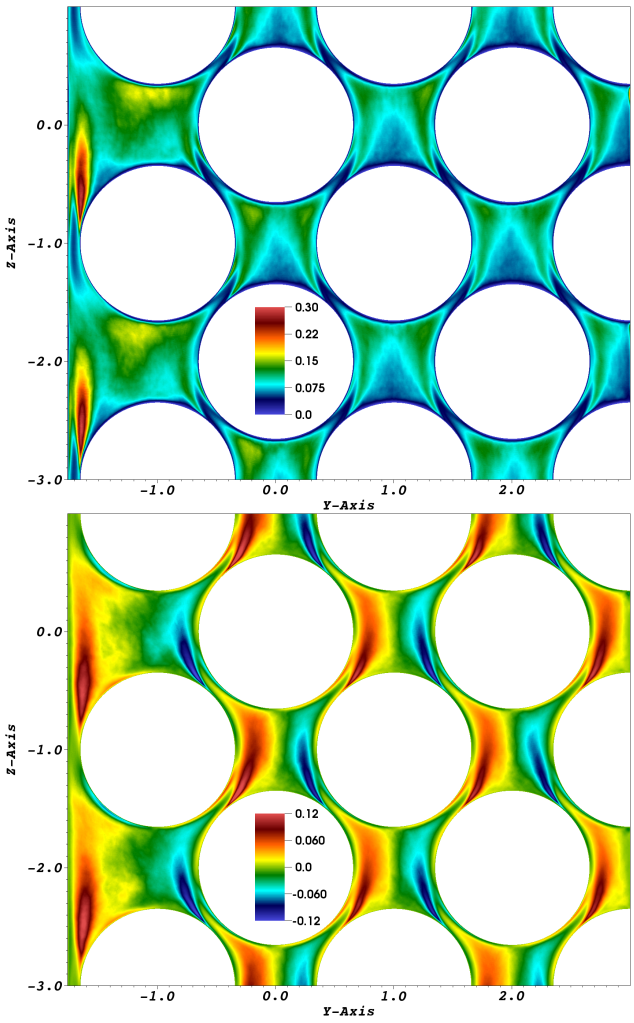

Figure 5.11: Pseudo-color field for $\langle u_z u_z \rangle$ (top), and $\langle u_y u_z \rangle$ (bottom).

$\langle u_x u_y \rangle$, and $\langle u_x u_z \rangle$ Reynolds stresses are expected to be smaller in the plane under consideration here, since the magnitude $\langle U_x \rangle$ is small.

For $\langle u_y u_z \rangle$, shown in Fig. 5.11, acceptable convergence has been achieved. The shear layers in the gaps between the spheres is again consistent with the results generated in the 1 FCC case. Additionally, as with $\langle u_z u_z \rangle$, the stress is increased in the area where the high velocity flow through the contracted gap between the wall and first row of spheres interacts with the stagnation region behind the spheres.

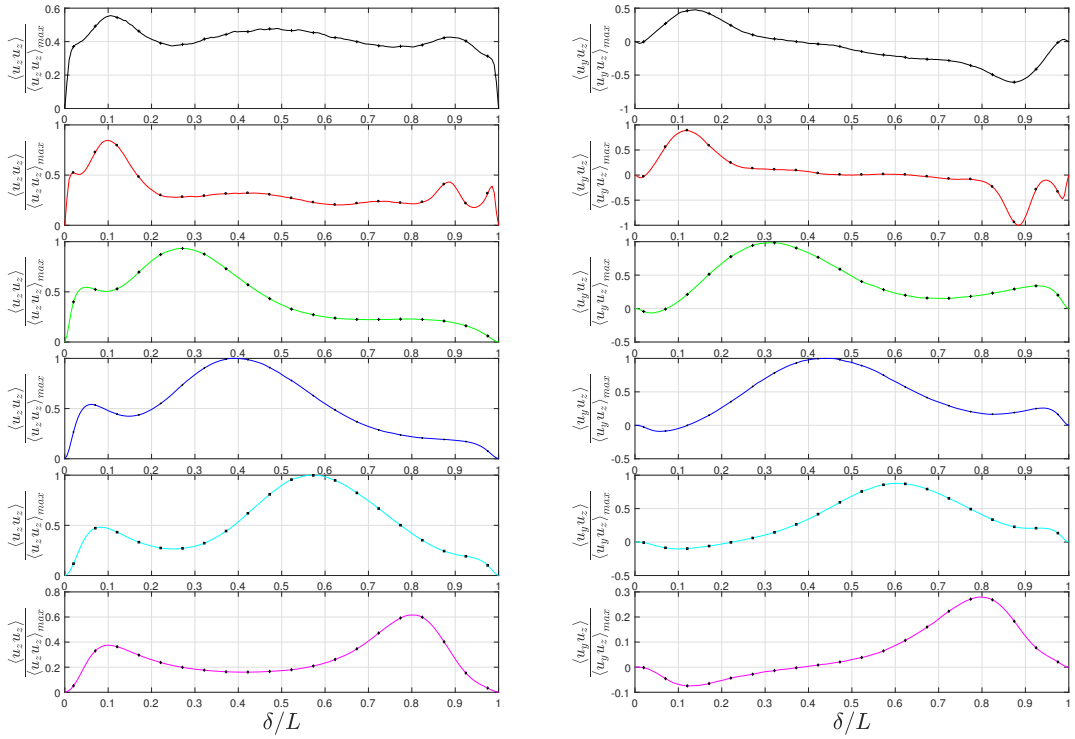

Figure 5.12: Normalized interpolated line profiles for $\langle u_z u_z \rangle$ (left), and $\langle u_y u_z \rangle$ (right).

This is due to the entrainment effect of the high velocity flow through the narrow gap causing lateral acceleration of the flow towards the wall before being decelerated again as it approaches the wall.

The interpolated profiles for $\langle u_z u_z \rangle$, shown in Fig. 5.12, indicate local maxima close to the wall for the lines located in the large gap between the spheres. These local maxima correspond to the area of high shear stress shown in Fig. 5.11. The smaller double bumps observed in the second (red) profiles show the effect of two spheres in close proximity. This type of behavior should prove difficult for RANS based simulations to capture accurately, and is thus a good example of why these

high-fidelity results are important for this class of flow.

Figure 5.12 also shows the in-plane covariance component, $\langle u_y u_z \rangle$. The first line interpolation (black), which is located in the center of the large gap between the pebbles, shows a qualitatively similar profile to those observed in the central gaps of the 1FCC case. The subsequent line profiles also show the maxima of this Reynolds stress component in the area where the interaction between the recirculation cell and the high velocity jet occurs.

5.4 Conclusions

This section detailed the development and results of a direct numerical simulation of incompressible flow in a domain consisting of regularly packed spheres, with a bounding wall. Based on a review of the available literature, very few works have, either experimentally of computationally, treated the near wall effects of flow in a geometry such as this in detail. The flow Reynolds number was chosen to be consistent with that used in the generation of the FCC unit cell data in §4.

Presented results include selected first- and second-order turbulence statistics. While the ensemble averaging routines that are available in Nek5000 provide a powerful tool for reducing the real time to convergence of the turbulence statistics, the high computational cost of DNS means that certain statistics could not be considered converged even as the computational hours committed to their development neared 10 million hours.

The statistics that could be considered converged were qualitatively similar to those observed in the FCC case when considering domain units that were at least two rows of spheres removed from the wall. Closer to the wall, the altered packing structure resulted in areas of increased stream wise velocity flow in the areas of minimum clearance between the wall and the first row of spheres. Additionally,

enlarged areas of flow recirculation were observed behind the spheres in the first row next to the wall.

Additional data generation is possible for this case, such as the calculation of cross-flow fluxes to ascertain whether the wall leads to any significant cross-flow effects. With more time integration, the budgets of the turbulent kinetic energy equation may also be calculated to investigate how the geometry in the near wall region influences the transport of turbulence energy, especially since the presented second order statistics show increased shear stress magnitudes in the wake separation areas.

6. CONCLUSIONS

In this section, the conclusions drawn from the three numerical experiments are consolidated and synthesized in to an overarching set of conclusions. The objectives for each experiment are restated in the subsections that follow here. Conclusions are then discussed for each objective.

6.1 Conclusions

The conclusions are detailed in the order in which they were presented in the results sections.

6.1.1 Numerical Experiment I

- Verify the simulation methodology by using the available numerical simulation and experimental literature.

Data from literature that treat the canonical case of flow over a sphere in free stream conditions were used to verify the correct implementation of the case. Pertinent results used for comparison were skin-friction coefficients, sphere surface pressure coefficient, shedding Strouhal number, and domain axial center-line velocity profiles. Good comparisons were obtained for all the data.

It was imperative that the simulation methodology be confirmed before extension to the two sphere case. Since the objective of the free-stream flow cases was to confirm that the addition of spheres to the canonical case would increase the temporal instability of the flow, confidence in the methodology was paramount.

- Confirm increased meta-stable behavior of long time-averaged data with the addition of a additional spheres to the canonical case.

Based on comparison of several first- and second-order turbulence statistics and components of the TKE transport equation, it was observed the the addition of a second sphere in the free-stream flow cases introduced significant asymmetry of the temporally averaged flow data. This is consistent with observations made in the FCC case.

6.1.2 Numerical Experiment II

- Generate a high-fidelity database of time-invariant flow data, including:
  - First- and second-order turbulence statistics.
  - Budgets of the turbulent kinetic energy.

The results presented in §4 show selected first- and second-order turbulence statistics, and selected terms of the TKE transport equation. The conformance of the data to DNS requirements was verified using both the calculated values of the Kolmogorov scales, as well as the comparison of data sets of differing polynomial order. The data conformed to DNS requirements based on both criteria.

The data generated using seventh- and ninth-degree discretization delivered similar results, indicating that even the lowest chosen discretization level delivered DNS results. This is important in practical terms, since the computational effort per FTT is significantly less than for the higher discretization levels. Thus, when considering first- and second-order statistics, higher levels of discretization are not required.

- Identify and isolate temporal instabilities present in the flow.

The long time-integration achieved during the FCC runs showed a low-frequency switching behavior of the flow that led to an asymmetry of the turbulence statistics in the symmetric flow domain. A POD of the flow revealed time-dependent coherent structures in the recirculation region behind the pebbles, which is consistent

with observations made in literature regarding slowly revolving flow wake separation structures. The behavior of these structures correlated with the asymmetry that was manifesting in the turbulence statistics.

Based on the observed asymmetry of the flow statistics, further tests were done using an expanded FCC domain and an ensemble averaging scheme that allowed for spatial averaging of the flow instead of temporal averaging. The results from this case delivered symmetric, invariant first- and second-order statistics.

These findings challenge the ergodicity assumption that allows time-averaged data to be equated to ensemble (spatial) averaged data. While the mechanism that drives the low-frequency oscillatory behavior has not been fully quantified, it can be concluded that to generate invariant statistics for the purposes of high-fidelity database generation, ensemble averaging routines may be required to remove any asymmetry from the statistics. Researchers must however be cognizant of the fact that the ensemble averaging procedure may in effect be suppressing low-frequency physical processes in the flow.

6.1.3 Numerical Experiment III

- Generate first-of-a-kind DNS results that quantify the effect of a bounding wall on the flow.

The purpose of the simulation of the wall bounded geometry was to implement and expand the lessons learnt from the previous studies and develop an initial turbulence statistics data set that quantified the flow in the near wall region of a wall bounded, expanded FCC domain.

Initial first- and second-order statistics generated for the wall bounded case was discussed. It was observed that the flow acceleration in the contracted spaces between the pebbles and the bounding wall cause the flow to relaminarize. Also observed was

enhanced flow stagnation and recirculation effects in the first row of spheres next to the wall.

The above mentioned effects may have a significant impact on heat transfer behavior in a practical system, as the convective heat transfer will be diminished due the the laminarization of the flow in the areas where the pebbles contact the wall. The flow stagnation regions will also large temperature gradients that may compromise the structural integrity of the near wall spheres during long residence time in the reactor core.

6.2 Future work

Based on the findings, a number of subsequent studies may be initiated to expand upon the analyses presented in this dissertation. These include:

1. The addition of heat transfer to characterize the effects of the flow on the temperature distribution in pebble bed geometries. Conjugate heat transfer treatment is recommended for such investigations.

2. DNS studies of the effect of inter-pebble contact treatment in both flow and thermal fields. A systematic investigation of different contact treatments using high-fidelity methods has not been done based upon a review of the currently available literature. Since contact treatment has the ability to markedly influence results obtained using numerical simulations, it's effect must be quantified.

3. Investigation of the physical effects that drive the metastable behavior of the flow in pebble bed geometries.

BIBLIOGRAPHY

[1] A. Shams, F. Roelofs, E. Komen, and E. Baglietto, "Improved Delayed Detached Eddy Simulation of a Randomly Stacked Nuclear Pebble Bed," *Computers & Fluids*, vol. 122, pp. 12–25, 2015.

[2] J.-S. Wu and G. M. Faeth, "Sphere Wakes in Still Surroundings at Intermediate Reynolds Numbers," *AIAA Journal*, vol. 31, no. 8, pp. 1448–1455, 1993.

[3] M. A. Fütterer, L. Fu, C. Sink, S. de Groot, M. Pouchon, F. Kim, Y. W.and Carré, and Y. Tachibana, "Status of the Very High Temperature Reactor System," *Progress in Nuclear Energy*, vol. 77, pp. 266–281, 2014.

[4] P. Sabharwall, S. M. Bragg-Sitton, and C. Stoots, "Challenges in the Development of High Temperature Reactors," *Energy Conversion and Management*, vol. 74, pp. 574–581, 2013.

[5] C. Argyropoulos and N. Markatos, "Recent Advances on the Numerical Modelling of Turbulent Flows," *Applied Mathematical Modelling*, vol. 39, no. 2, pp. 693–732, 2015.

[6] A. Shams, F. Roelofs, E. M. J. Komen, and E. Baglietto, "Large Eddy Simulation of a Nuclear Pebble Bed Configuration," *Nuclear Engineering and Design*, vol. 261, pp. 10–19, 2013.

[7] Y. A. Hassan, "Large Eddy Simulation in Pebble Bed Gas Cooled Core Reactors," *Nuclear Engineering and Design*, vol. 238, no. 3, pp. 530–537, 2008.

[8] A. T. Patera, "A Spectral Element Method for Fluid Dynamics: Laminar Flow in a Channel Expansion," *Journal of Computational Physics*, vol. 54, no. 3, pp. 468–488, 1984.

[9] S. B. Pope, *Turbulent Flows*. Cambridge University Press, 2000.

[10] M. O. Deville, P. F. Fischer, and E. H. Mund, *High-Order Methods for Incompressible Fluid Flow*. Cambridge University Press, 2002.

[11] Y. Maday and A. T. Patera, "Spectral element methods for the incompressible Navier-Stokes equations," in *State-of-the-art Surveys on Computational Mechanics. New York, American Society of Mechanical Engineers*, pp. 71–143, 1989.

[12] P. Ward, "Direct Numerical Simulation of the Flow in a Pebble Bed," MS thesis, Texas A&M University, 2014.

[13] L. F. Richardson, *Weather Prediction by Numerical Process*. Cambridge: Cambridge University Press, 2 ed., 2007.

[14] A. Kolmogorov, "The Local Structure of Turbulence in Incompressible Viscous Fluid for Very Large Reynolds Numbers," *Akademiia Nauk SSSR Doklady*, vol. 30, pp. 301–305, 1941.

[15] P. Holmes, J. L. Lumley, and G. Berkooz, *Cambridge Monographs on Mechanics: Turbulence, Coherent Structures, Dynamical Systems and Symmetry*. Cambridge, GB: Cambridge University Press, 2012.

[16] L. Sirovich, "Turbulence and the Dynamics of Coherent Structures. I. Coherent Structures," *Quarterly of applied mathematics*, vol. 45, no. 3, pp. 561–571, 1987.

[17] E. Merzari, W. D. Pointer, and P. Fischer, "Numerical Simulation and Proper Orthogonal Decomposition of the Flow in a Counter-Flow T-Junction," *Journal of Fluids Engineering*, vol. 135, no. 9, p. 91304, 2013.

[18] A. G. Tomboulides and S. A. Orszag, "Numerical Investigation of Transitional and Weak Turbulent Flow Past a Sphere," *Journal of Fluid Mechanics*, vol. 416, pp. 45–73, 2000.

[19] I. Rodriguez, R. Borell, O. Lehmkuhl, C. D. Perez Segarra, and A. Oliva, "Direct Numerical Simulation of the Flow Over a Sphere at Re = 3700," *Journal of Fluid Mechanics*, vol. 679, pp. 263–287, 2011.

[20] G. S. Constantinescu and K. D. Squires, "LES and DES Investigations of Turbulent Flow over a Sphere at Re = 10,000," *Flow, Turbulence and Combustion*, vol. 70, no. 1, pp. 267–298, 2003.

[21] L. H. Fick, E. Merzari, , and Y. A. Hassan, "Direct Numerical Simulation of Pebble Bed Flows: Database Development and Investigation of Low-frequency Temporal Instabilities," *Journal of Fluids Engineering*, vol. 139, no. 5, p. 51301, 2017.

[22] E. Achenbach, "Vortex Shedding from Spheres," *Journal of Fluid Mechanics*, vol. 62, no. 02, pp. 209–221, 1974.

[23] H. J. Kim and P. A. Durbin, "Observations of the Frequencies in a Sphere Wake and of Drag Increase by Acoustic Excitation.," *Physics of Fluids*, vol. 31, no. 11, p. 3260, 1988.

[24] E. Achenbach, "Experiments on the Flow Past Spheres at Very High Reynolds Numbers," *Journal of Fluid Mechanics*, vol. 54, no. 03, pp. 565–575, 1972.

[25] J. Y. Lee and S. Y. Lee, "Flow Visualization of Pebble Bed HTGR," *Proceedings of the 4th International Topical Meeting on High Temperature Reactor Technology*, vol. 2, pp. 319–322, 2008.

[26] B. Eisfeld and K. Schnitzlein, "The Influence of Confining Walls on the Pressure Drop in Packed Beds," *Chemical Engineering Science*, vol. 56, pp. 4321–4329, 2001.

[27] C. G. du Toit and P. G. Rousseau, "Modeling the Flow and Heat Transfer in a Packed Bed High Temperature Gas-Cooled Reactor in the Context of a Systems CFD Approach," *Journal of Heat Transfer*, vol. 134, no. 3, p. 31015, 2012.

[28] P. Rousseau, C. du Toit, and W. Landman, "Validation of a Transient Thermal-Fluid Systems CFD Model for a Packed Bed High Temperature Gas-cooled Nuclear Reactor," *Nuclear Engineering and Design*, vol. 236, no. 5-6, pp. 555–564, 2006.

[29] A. Shams, F. Roelofs, E. Komen, and E. Baglietto, "Quasi-Direct Numerical Simulation of a Pebble Bed Configuration. Part I: Flow (Velocity) Field Analysis," *Nuclear Engineering and Design*, vol. 263, pp. 473–489, 2012.

[30] A. Shams, F. Roelofs, E. M. J. Komen, and E. Baglietto, "Optimization of a Pebble Bed Configuration for Quasi-direct Numerical Simulation," *Nuclear Engineering and Design*, vol. 242, pp. 331–340, 2012.

[31] Y. A. Hassan and E. E. Dominguez-Ontiveros, "Flow Visualization in a Pebble Bed Reactor Experiment using PIV and Refractive Index Matching Techniques," *Nuclear Engineering and Design*, vol. 238, no. 11, pp. 3080–3085, 2008.

[32] E. Merzari, W. D. Pointer, J. G. Smith, A. Tentner, and P. Fischer, "Numerical Simulation of the Flow in Wire-Wrapped Pin Bundles: Effect of Pin-Wire Contact Modeling," *Nuclear Engineering and Design*, vol. 253, pp. 374–386, 2012.

[33] M. Tavakol, O. Abouali, and M. Yaghoubi, "Large Eddy Simulation of Turbulent Flow around a Wall Mounted Hemisphere," *Applied Mathematical Modelling*,

vol. 39, no. 13, pp. 3596–3618, 2015.

[34] J. H. Ferziger and M. Peric, *Computational Methods for Fluid Dynamics*. Springer Berlin Heidelberg, 2001.

[35] S. Taneda, "Visual Observations of the Flow Past a Sphere at Reynolds Numbers Between 10^4 and 10^6," *Journal of Fluid Mechanics*, vol. 85, no. 1, pp. 187–192, 1978.

[36] V. Makarashvili, E. Merzari, A. Obabko, P. Fischer, and A. Siegel, "Accelerating the High-Fidelity Simulation of Turbulence: Ensemble Averaging," in *Proceedings of the ASME Fluids Engineering Division Summer Meeting (FEDSM)*, 2016.

[37] P. Sagaut, *Large Eddy Simulation for Incompressible Flows*. Springer-Verlag Berlin Heidelberg, 2002.

[38] A. Shams, F. Roelofs, E. Komen, and E. Baglietto, "Numerical Simulations of a Pebble Bed Configuration using Hybrid (RANS-LES) Methods," *Nuclear Engineering and Design*, vol. 261, pp. 201–211, 2013.

[39] A. Gandhir, "Computational Analysis of Fluid Flow in Pebble Bed Modular Reactor," Master's thesis, Texas A & M University, College Station, TX, 2011.

[40] G. Yesilyurt, "Numerical Simulation of Flow Distribution for Pebble Bed High Temperature Gas Cooled Reactors," MS thesis, Texas A&M University, 2003.

[41] M. Ozgoren, A. Okbaz, S. Dogan, B. Sahin, and H. Akilli, "Investigation of Flow Characteristics around a Sphere Placed in a Boundary Layer over a Flat Plate," *Experimental Thermal and Fluid Science*, vol. 44, pp. 62–74, 2013.

[42] H. Zhao, X. Liu, D. Li, A. Wei, K. Luo, and J. Fan, "Vortex Dynamics of a Sphere Wake in Proximity to a Wall," *International Journal of Multiphase Flow*, vol. 79, pp. 88–106, 2016.